

**Small-molecule inhibitors of non-structural protein 15
(NSP15) for the treatment of SARS-CoV-2**

by

Jerry Chen

A thesis submitted in partial fulfillment of the requirements for the degree of

Master of Science

Department of Pharmacology

University of Alberta

© Jerry Chen, 2022

Abstract

Background: Severe acute respiratory syndrome coronavirus 2 (SARS-CoV-2) is responsible for the coronavirus disease 2019 (COVID-19) pandemic. As of 2022, the viral spread is still ongoing and has claimed the lives of at least 6.24 million globally. Despite being more than two years into the pandemic, the need to find effective treatments for SARS-CoV-2 remains. This project aims to screen for small molecule inhibitors of SARS-CoV-2 non-structural protein 15 (NSP15). NSP15 is a relatively conserved RNA uracil endonuclease implicated in the evasion of host interferon and immune defenses. NSP15 was found to be essential for coronavirus replication *in-vivo* and represents a promising therapeutic target for treating SARS-CoV-2 infections. Currently, only a limited number of NSP15 inhibitors have been identified and these have only limited therapeutic potential. As a result, this project aims to further expand the repertoire of potential coronavirus treatments by finding novel SARS-CoV-2 NSP15 inhibitors through high-throughput screening.

Methods: To screen for NSP15 small-molecule compounds, a fluorescent resonance energy transfer (FRET)-based NSP15 activity assay was designed and optimized. Using this assay, a high-throughput screen of over 108,000+ compounds for NSP15 inhibition, and a secondary screen of the top 1280 hits, was performed. Top compounds were further validated by orthogonal assays such as for dose-dependency using the FRET-based assay, the Amplex Red assay for redox cycling, and an RNA gel cleavage assay. Furthermore, compound inhibition mechanisms were determined through Michaelis-Menten titration experiments. Finally, compound cytotoxicity tests were

performed and the efficacy of the compounds against SARS-CoV-2 viral infection was measured in the Vero cell line using plaque assay.

Results: I successfully validated and optimized a FRET-based NSP15 activity assay, including the validation of NSP15 characteristics and enzyme kinetics. From the high-throughput screen, I validated six novel compounds for NSP15 inhibition using the various orthogonal assays. These compounds inhibited NSP15 in *in-vitro* biochemical assays at ranges from 5-95 μM with competitive, mixed, and non-competitive mechanisms. Surprisingly, three compounds, CID5675221, Hexachlorophene, and IPA3, showed strong efficacy in Vero cells against SARS-CoV-2 viral replication and was determined to have positive selectivity index 50 (SI_{50}) ratios.

Conclusions: From the high-throughput screen of SARS-CoV-2 NSP15 inhibitors, I validated six novel NSP15 inhibitors using *in-vitro* enzymatic assays. Of the six compounds, three compounds showed favorable selectivity index 50 (SI_{50}) ratios in Vero cell culture. As a result, these compounds could bode well for a downstream hit-to-lead pipeline. Future experiments will further elucidate the binding affinity and structural mechanism by which these compounds bind to the NSP15 protein, and to further evaluate their potential as therapeutics for the treatment of COVID-19.

Preface/Attributions

This thesis includes collaborations with research labs in the University of Alberta and the University of British Columbia. Joaquin Lopez-Orozco at the High Content Analysis Core Facility (University of Alberta), and Tom Pfeifer at the Biofactorial Facility (University of British Columbia, Canada), helped perform the primary and secondary high-throughput screenings respectively, including operation of the high-throughput screening machineries. Tom Pfeifer provided the graphic summary and statistics of the main screen in **Figure 3.4b**. Dr. Basil Hubbard and I conceived and designed the experiments. I carried out the experimentations. Filip Reformat and Dr. Benjamin Brigant provided partial assistance in designing and purifying the NSP15 protein cloning and purification. Additionally, Filip Reformat helped design the NSP15 mutants. **Table 3.4** was generated by me with help and knowledge from Helen Wu. SARS-CoV-2 Vero plaque assay data was generated in collaboration with Dr. Daniel Limonta Velázquez, who carried out all Biosafety Level 3 work and assay, while under the lab of Dr. Tom Hobman at the University of Alberta. The design, creation, validation, and performance of experiments were done by me unless otherwise stated above.

Acknowledgements

I would like to first and foremost thank Dr. Basil Hubbard, my supervisor, for having me as a graduate student. His guidance has been immeasurable, and I am grateful for the opportunity to study under his mentorship. I am also thankful for the support and insight provided by my committee members, Dr. James Hammond and Dr. Kristi Baker. Their suggestions have been invaluable in guiding my projects. I would also like to thank Filip Reformat and Dr. Benjamin Brigant for their incredible assistance in helping start a brand-new project during the pandemic! I would also like to thank Evan Kerek, Chris Cromwell, and all other members of the Hubbard lab for making such an excellent lab. I am also thankful to Luka Wang, Sidath Wijayasiri and Helen Wu for their contributions and assistance. I would also like to thank our many collaborators, including Dr. Xiaoyun Tang, Dr. Joaquin Lopez-Orozco, Dr. Tom Pfeifer, Dr. Daniel Limonta Velázquez, Ola Mabrouk, and Rabih Abou Farraj, for the project would not be what it is without them. Finally, I would like to thank my family and friends for their continued support. These years have been an incredible journey thanks to all of you.

Table of Contents

Abstract	ii
Preface/Attributions	iv
Acknowledgements	v
Abbreviations Used	x
List of Tables	x
List of Figures	xi
Scope of Masters	xiii
Outline of Chapters	xiii
Introduction to the Problem	xiii
Research Questions	xiv
Significance of Research	xiv
CHAPTER 1: Introduction to SARS-CoV-2 and NSP15	1
1.0 Overview	1
1.1 Introduction to SARS-CoV-2	1
1.1.1 SARS-CoV-2 Taxonomy	1
1.1.2 SARS-CoV-2 Genome Organization and Viral Translation of NSPs	2
1.1.3 SARS-CoV-2 Structural-Proteins and Accessory Factors	4
1.1.4 Coronavirus Transcription and Replication	5
1.2 Introduction to non-structural protein 15 (NSP15)	6
1.2.1 NSP15 Genetic and Phylogeny Insights	6
1.2.2 NSP15 Structure	7
1.2.3 NSP15 has Endoribonuclease Activity	8
1.3 Coronavirus and the Immune System	9

1.3.1 Interferon Response Types	9
1.3.2 The RIG-I-Like Receptor (RLR) Family: RIG-I and MDA5.....	10
1.3.3 Endosomal Toll-Like Receptors	11
1.3.4 Protein Kinase R (PKR) pathway.....	11
1.3.5 Oligoadenylate Synthetase (OAS) / RNase L Pathway	12
<i>1.4 NSP15 Function in Coronavirus Infection</i>	<i>12</i>
1.4.1 NSP15's Role in Evading Interferon Defence.....	12
1.4.2 Alternative NSP15 Mechanisms	15
<i>1.5 Effect of NSP15 on Viral Titers in Cell Culture</i>	<i>16</i>
<i>1.6 SARS-CoV-2 NSP15 and SARS-CoV-2 Interferon Defenses.....</i>	<i>17</i>
1.6.1 Interferon Screens	17
1.6.2 Autophagy	18
1.6.3 SARS-CoV-2 Interferon Defense	18
<i>1.7 NSP15 Inhibitors</i>	<i>19</i>
<i>1.8 High-throughput Screening of Small-Molecules</i>	<i>20</i>
CHAPTER 2: Materials and Methods for Screening for NSP15 Inhibitors	22
2.0 General Reagents.....	22
2.1 NSP15 Cloning.....	22
2.2 NSP15 Protein Purification.....	24
2.3 NSP15 Fluorescent Activity Assay	25
2.4 High-Throughput Screening	26
2.5 NSP15 RNA Gel Cleavage Assay and Densitometry	27
2.6 Amplex Red Assay.....	27
2.7 Vero Cell Culture and Toxicity Assay.....	28
2.8 Vero SARS-CoV-2 Plaque Assay.....	28
2.9 In-silico Pharmacological Predictors	29
2.9 Data Analysis	29
CHAPTER 3: High-throughput (HTP) Screening to Identify SARS-CoV-2 NSP15 Inhibitors	30

3.1 NSP15 Reaction Setup and Substrate Optimization.....	30
3.1.1 NSP15 Reaction Setup.....	30
3.1.2 NSP15 EDTA Inhibition and Ion Preference.....	32
3.1.3 NSP15 Mutant Analysis.....	33
3.1.4 Enzyme Kinetics.....	35
3.2 NSP15 High-throughput Screen of Small-Molecule Inhibitors.....	36
3.3 NSP15 Fluorescent and Quenching Assay Hit Validation.....	39
3.4 NSP15 Inhibitors with Amplex Red Assay.....	41
3.5 NSP15 RNA Gel Cleavage Assay.....	43
3.6 NSP15 Compound Inhibitors and IC ₅₀ curves.....	44
3.7 NSP15 Michaelis-Menten of Compound Inhibitors.....	47
3.8 NSP15 Compound Cytotoxicity Concentration 50 (CC ₅₀) in Vero cells.....	50
3.9 Compound Inhibitory Concentration 50 (IC ₅₀) and Calculation of Therapeutic Index 50 (TI ₅₀) in Vero cells.....	53
3.10 Effect of DTT on NSP15 Activity and IPA3 Inhibition.....	55
3.11 Predicted Therapeutic Profile and Properties of NSP15 compounds.....	56
Chapter 4: Discussion.....	60
4.1 Summary of findings.....	60
4.1.1 FRET-Assay and RNA Sequence Differences.....	60
4.1.2 NSP15 Manganese Dependency.....	61
4.1.4 NSP15 Mutants.....	61
4.1.3 NSP15, DTT, and Amplex Red.....	62
4.1.5 NSP15 Enzyme Kinetics.....	63
4.1.6 IC ₅₀ Hill-Slope.....	63
4.1.6 Compound Discussion.....	64
4.1.6.1 CID4017446.....	64
4.1.6.2 CID5220994.....	66
4.1.6.3 CID5266986.....	67
4.1.6.4 CID5675221.....	69

4.1.6.5 Hexachlorophene.....	70
4.1.6.6 IPA3	71
4.1.6.7 On the Possibility of Covalent Interactions of Inhibitors	73
4.1.6.8 In the Context of Viral Treatments	74
4.1.6.9 Summary and Application of Research	76
4.2 <i>Limitations</i>	77
4.2.1 Screening and FRET-based Assay Limitations	77
4.2.2 Gel-Based IC ₅₀	79
4.2.3 Vero Cell Culture and Plaque Assay Limitations	80
4.2.4 Michaelis-Menten.....	82
4.3 <i>Future Directions</i>	82
References	85

List of Tables

Name	Description
Table 1.1	List of coronavirus non-structural proteins (NSPs) and their function(s).
Table 2.1	NSP15 codon optimized sequence.
Table 2.2	Primers for NSP15 cloning and sequencing.
Table 2.3	RNA substrate sequences for NSP15 activity assay.
Table 3.1	Summary of IC ₅₀ values from both gel-based and FRET-based assays and their Hill slope values.
Table 3.2	Summary of Michaelis-Menten values for compound inhibitors.
Table 3.3	Summary of Cytotoxicity Concentration 50 (CC ₅₀), Inhibitory Dose 50 (IC ₅₀), and Selectivity Index 50 (SI ₅₀) of NSP15 compound inhibitors in Vero cells against SARS-CoV-2.
Table 3.4	Predicted Lipinski's rule of the five analyses and properties for NSP15 compound inhibitors.
Table 4.1	Chemical structure of compound CID4017446 and its moieties.
Table 4.2	Chemical structure of compound CID5220994 and anthraquinones.
Table 4.3	Chemical structure of CID5266986, CID5326429 and Exebryl-1.
Table 4.4	Chemical structure of CID5675221 and Rhodanine.

List of Figures

Name	Description
Figure 1.1	SARS-CoV-2 genome and proteins.
Figure 1.2	SARS-CoV-2 NSP15 protein alignment compared to SARS-CoV-1 and MERS-CoV.
Figure 1.3	Monomeric structure of SARS-CoV-2 NSP15 compared to SARS-CoV-1 and MERS-CoV.
Figure 3.1	Establishment of FRET-based NSP15 activity assay.
Figure 3.2	Activity of various NSP15 mutants.
Figure 3.3	NSP15 enzyme kinetics.
Figure 3.4	SARS-CoV-2 NSP15 high-throughput screening of small-molecular inhibitors.
Figure 3.5	Fluorescent FRET-based assay validation of top nine NSP15 inhibitors.
Figure 3.6	Non-FRET-based validations of NSP15 compound inhibitors.
Figure 3.7	IC ₅₀ of compound inhibitors using FRET-based assay.
Figure 3.8	NSP15 gel cleavage IC ₅₀ of compound inhibitors.
Figure 3.9	Michaelis-Menten of the six compound inhibitors.
Figure 3.10	CC ₅₀ toxicity of NSP15 inhibitors in Vero cells.
Figure 3.11	Effect of NSP15 inhibitors on SARS-CoV-2 Replication in Vero Cells.
Figure 3.12	Effect of DTT on NSP15 and IPA3 Activity.

Abbreviations Used

ACE2 = Angiotensin-converting enzyme 2
ADME = absorption, distribution, metabolism, and excretion
AML = acute myeloid leukemia
BHQ1/2 = Black Hole Quencher 1/2
BMDM = Bone-marrow derived macrophages
CC₅₀, IC₅₀, SI₅₀ = Cytotoxic Concentration 50, Inhibitory Concentration 50, Selectivity Index 50
CNS = Central Nervous System
Cy5 = tetramethylindo(di)-carbocyanine 5
DMSO = dimethyl sulfoxide
DMV = double membrane vesicles
DTT = Dithiothreitol
EDTA = Ethylenediaminetetraacetic acid
EIF2a = Eukaryotic Translation Initiation Factor 2A
FAM = 6-Carboxyfluorescein
FRET = fluorescence resonance energy transfer
h.p.i = hours post-infection
HCoV = Human Coronavirus
HEPES = (4-(2-hydroxyethyl)-1-piperazineethanesulfonic acid)
hERG = Human ether-à-go-go related gene
IFN = interferon
ISG = interferon stimulating genes
m.o.i = multiplicity of infection
MAVS = Mitochondrial antiviral-signaling protein
MERS = Middle Eastern Respiratory Syndrome
NSP = non-structural protein
OAS = Oligoadenylate synthetases
ORF = Open Reading Frame
PAIN(s) = Pan-Assay Interference Compound(s)
PAK = p21-activated kinases
PAMPS = Pathogen-associated molecular patterns
PDB = Protein Data Bank
pDCs = plasmacytoid dendritic cells
PFU = Plaque Forming Units
PKR = protein kinase R
PolyA/U = PolyAdenosine/PolyUracil
PPB = Plasma Protein Binding
RdRp = RNA-dependent RNA polymerase
RIG-I-CARD = retinoic acid-inducible gene - I - Caspase recruitment domains
RTC = replication/transcription complex
S/N ratio = Signal/Noise Ratio
SARS-CoV = severe acute respiratory syndrome coronavirus
SDM = Site Directed Mutagenesis
SPR = Surface Plasmon Resonance
TBK1/IKKε = TANK-binding kinase 1/IκB kinase ε
TLR = Toll Like Receptors

Scope of Masters

Outline of Chapters

This thesis focuses on work done with the screening of small-molecule inhibitors of SARS-CoV-2 NSP15. **Chapter 1** contains the introduction to the project. **Chapter 2** contains the methodology. In **Chapter 3**, I will discuss the results of the experiments where I optimized and established a high-throughput compatible NSP15 activity assay and screened for 108,000+ compounds across a variety of compound libraries. Following compound validation and characterizations in orthogonal assays, I found six novel inhibitors of NSP15 that are suitable for future development. **Chapter 4** contains the discussion, including limitations and future direction.

During my Masters, I also performed work on the protein BLOC1S1, which is outside this thesis's scope. In addition, outside the scope of this thesis, I performed experiments for the publication "Kerek EM, Yoon KH, Luo SY, **Chen J**, Valencia R, Julien O, Waskiewicz AJ, Hubbard BP. A conserved acetylation switch enables pharmacological control of tubby-like protein stability. *J Biol Chem.* 2020 Nov 13;296:100073. doi: 10.1074/jbc."

Introduction to the Problem

At the time of this writing, in 2022, the SARS-CoV-2 pandemic is still ongoing and has taken an estimated 6.24 million lives globally.¹ Treatment of the novel coronavirus remains challenging. Current treatments, like Remdesivir, have only shown mild therapeutic efficiency.² Additionally, new treatments such as Paxlovid and Molnupiravir have only begun to enter the market.³ Furthermore, new coronavirus variants may threaten vaccine efficacy.⁴ Therefore, new SARS-CoV-2 therapies are still needed. Non-structural protein 15 (NSP15) has been shown to play a critical role in viral immune evasion and suppression of interferon (IFN) pathways, and is essential for viral replication.⁵ Recently, Sars-CoV-2 interferon antagonist screens have identified NSP15 as a potent interferon antagonist.^{6, 7} Previous work on SARS-CoV-1 NPS15 found the small-molecule, BenzopurpurinB, with putative ability to decrease viral replication in *in-*

vitro cell culture.⁸ As a result, NSP15 represents a therapeutic target for small-molecule inhibition and treatment of SARS-CoV-2. At the start of this writing, only two potential NSP15 inhibitors with limited therapeutic potential have been found.^{9, 10} This project aims to discover novel small-molecule inhibitors of SARS-CoV-2 NSP15. I hypothesize that high-throughput screening will successfully identify small molecule inhibitors of NSP15 enzyme *in-vitro*, and that such compound inhibitors will attenuate SARS-CoV-2 viral replication in cell culture model(s).

Research Questions

- What is the optimal setup for a high-throughput scalable assay of NSP15 activity?
- Does SARS-CoV-2 NSP15 follow previous SARS-CoV-1 NSP15 characteristics and enzyme kinetics?
- Will high-throughput screening of SARS-CoV-2 NSP15 find small-molecule inhibitors?
- What are the characteristics of inhibition for any discovered inhibitors?
- What is the efficacy and toxicity of such inhibitors in cell culture?
- What is the compound to protein structural-functional basis for inhibition?

Significance of Research

Given the global SARS-CoV-2 pandemic, this work is highly relevant to finding novel SARS-CoV-2 treatments. NSP15 represents an attractive therapeutic target, and if the compounds are successful in testing, this work may result in potential treatment options for SARS-CoV-2. At the same time, a novel NSP15 inhibitor compound will provide the basis for future rational drug design and hit-to-lead pipelines that will aid in the search for other NSP15 inhibitors. Furthermore, this work will provide the basis for expanded screening of NSP15 inhibitors, and the assays will contribute to the understanding of NSP15 biochemical function. Given the highly conserved nature of NSP15, the research is likely relevant to other coronavirus species as well.

CHAPTER 1: Introduction to SARS-CoV-2 and NSP15

1.0 Overview

Severe acute respiratory syndrome coronavirus 2 (SARS-CoV-2) is a positive-sense single-stranded RNA (+ssRNA) coronavirus responsible for the respiratory disease, COVID-19¹¹. Although the origins of SARS-CoV-2 is still under research, the virus may be of zoonotic origin due to close phylogenetic relationship with bat coronaviruses¹². First discovered in Wuhan, China, in late 2019, the disease has spread globally, resulting in the declaration of official pandemic status on March 11, 2020^{11, 13}. As of 2022, the viral spread is still ongoing and has claimed the lives of at least 6.24 million globally¹. Due to the global pandemic, there is now renewed interest in coronavirus biology and treatment research.

1.1 Introduction to SARS-CoV-2

1.1.1 SARS-CoV-2 Taxonomy

According to the International Committee on Taxonomy of Viruses (ICTV) classification, SARS-CoV-2 belongs to the *Nidovirales* order of viruses¹⁴. This viral order is characterized by their positive sense ssRNA and their transcription of subgenomic RNA¹⁵. The *Nidovirales* order includes the families: *Coronaviridae*, *Roniviridae*, *Arteriviridae*, and *Mesoniviridae*¹⁵. SARS-CoV-2 is part of the *Coronaviridae* family, and subsequently, its *Coronavirinae* subfamily, which is characterized by their large (~30kb) RNA genome and their “corona” structure in the envelope¹⁵. The *Coronavirinae* subfamily contains four genera: alpha, beta, gamma, and delta coronavirus¹⁵. Of the seven known human coronaviruses, the alpha genera includes HCoV-229E, HCoV-NL63, while the rest (including SARS-CoV-2) are in the beta genera¹⁶. The betacoronavirus genera includes four lineages¹⁵. Lineage A (*Embecovirus*) includes the human viruses HCoV-OC43 and CoV-HKU1^{15, 16}. Lineage B includes human SARS-CoV-1, and SARS-CoV-2¹⁴. Lineage C (*Merbecovirus*) includes human virus MERS^{15, 16}. Murine hepatitis virus (MHV) belongs to Lineage A¹⁵. It should be noted that the influenza flu viruses are negatively RNA stranded and belong in a separate phylum of

viruses unrelated to coronavirus¹⁷. Meanwhile, the common cold is a mixture of viruses with a relatively small population of cases (15%) resulting from non-SARS and non-MERS human coronaviruses¹⁸. When comparing SARS-CoV-2 to other human coronaviruses, SARS-CoV-2 is most phylogenetically similar to SARS-CoV-1¹⁹.

1.1.2 SARS-CoV-2 Genome Organization and Viral Translation of NSPs

Like other coronaviruses, SARS-CoV-2 contains a single copy of single-stranded positive-sense RNA (+ssRNA) spanning approximately 30kb (**Figure 1.1**)²⁰. Similar to host RNA, the genome contains a 5' end guanine cap with N7 methylation, as well as a 3' end poly-Adenosine (polyA) tail. Such features allow the viral RNA to be translated by host ribosomes upon viral entry^{20, 21}.

Starting from the coronavirus genome 5' end, the genome can be categorized by its open reading frames, ORF1a and ORF1b, which can be translated into polypeptide-pp1a and polypeptide-pp1b, respectively (**Figure 1.1**)²¹. Both pp1a and pp1b encode the viral non-structural proteins (NSPs). Pp1a encodes 11 NSPs. Meanwhile, a -1 ribosomal frameshift upstream of pp1a stop codon allows for the production of a larger hybrid polyprotein (pp1ab) encoding a total of 15 NSPs²¹. The polyproteins are then cleaved into individual NSPs by viral proteases NSP3 (containing papain domain) and/or NSP5 (containing 3C-like domain)²¹. **Table 1.1** contains a list of putative NSPs and a brief mention of their functions.

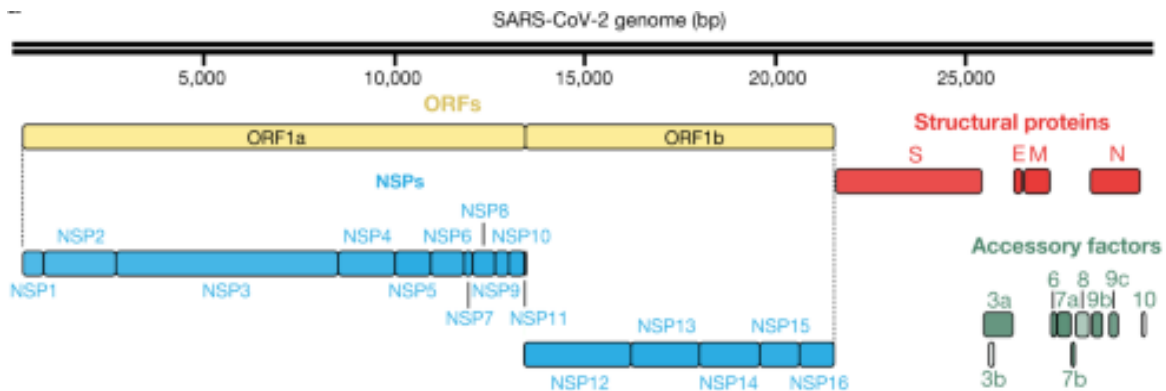


Figure 1.1. SARS-CoV-2 genome and proteins. The figure was adapted and taken from Gordon, D.E., Jang, G.M., Bouhaddou, M. *et al.*²².

Table 1.1. List of coronavirus non-structural proteins (NSPs) and their function(s).

Name	Function
NSP1	Binds to host ribosome for mRNA translation inhibition ²³
NSP2	Unknown/undefined
NSP3	Papain like protease (PLPro) responsible for NSP1-3 cleavage ²⁴
NSP4	Contains transmembrane domain with putative involvement in ER vesicle membrane rearrangement ^{25, 26}
NSP5	3C-Like (3CL ^{pro})/Main (M ^{pro}) protease responsible for NSP4-16 cleavage ^{21, 27}
NSP6	Contains transmembrane domain with putative involvement in ER vesicle membrane rearrangement ²⁸
NSP7	Complex with RNA-dependant RNA Polymerase complex (RdRp) ^{29, 30}
NSP8	Complex with RNA-dependant RNA Polymerase complex (RdRp) ^{29, 30}
NSP9	RNA binding protein, with putative involvement in replication ³¹
NSP10	Co-factor to NSP14 and NSP16 ^{32, 33} Stimulates NSP14 activity.
NSP12	Catalytic Subunit of RNA-dependant RNA Polymerase complex (RdRp) ^{29, 30}
NSP13	RNA helicase ^{34, 35}
NSP14	Exoribonuclease, with putative N7 methyltransferase function ^{36, 37}
NSP15	RNA endonuclease, host immune evasion ³⁸⁻⁴⁰
NSP16	2'O-Methyltransferase ³³

1.1.3 SARS-CoV-2 Structural-Proteins and Accessory Factors

Once the non-structural proteins have been translated, replication and translation of the structural proteins and the accessory factors can begin. The structural proteins (S, E, M, N) help make up the coronavirus virion. The spherical coronavirus virion is approximately ninety-one nanometers in diameter and has distinct “corona” heads owing to their spike protein⁴¹. These structural proteins include the following:

The envelope protein (E), the smallest of structural proteins, is an integral membrane protein, with proposed roles in viral assembly and budding, though its function requires more research⁴².

The membrane protein (M) is the most abundant structural protein. It contains three transmembrane domains alongside a smaller glycosylated N-terminus ectodomain and a larger C-terminus endo-domain⁴³. The protein may exist in many configurations to help constitute the virion shape⁴⁴.

The nucleocapsid (N) is found in the virion core, and its main function is to bind to and help package viral genomic RNA⁴⁵.

The spike protein (S) helps determine tropism and helps viral attachment and entry.

The spike protein is heavily N-glycosylated and forms a homo-trimer when engaging cells⁴¹. It consists of an S1 subunit for binding and an S2 subunit as the “stalk”⁴¹.

Cleavage of S1 and S2 subunits by furin proteases may be needed for cell entry⁴⁶.

SARS-CoV-2 contains a unique polybasic cleavage site (RRAR) at the S1 and S2 subunits junction. Additionally, there are predicted O-linked glycan residues between the two subunits of the spike, which may allow for more effective furin cleavage¹². SARS-CoV-2 spike protein binds to the human enzyme ACE2, and its entry into cells is mediated by host transmembrane protease serine 2 (TMPRSS2) protein⁴⁷. Interestingly, SARS-CoV-2 is believed to lack hemagglutinin-esterase, which is commonly found in

some subsets of *Betacoronaviruses* and is hypothesized to enhance spike protein attachment^{48, 49}.

Lastly, putative accessory factors are small proteins with emerging, but still to be determined, functions. These may not be necessary for viral replication or structure but may play key roles in immune modulation. For example, ORF3 was found to help with Type I interferon suppression⁵⁰. More research is needed to determine accessory factors' functions.

1.1.4 Coronavirus Transcription and Replication

Emerging evidence suggests that coronaviruses (perhaps all genera of coronavirus including SARS) synthesize their RNA inside perinuclear double-membrane vesicles (DMVs)⁵¹. These DMVs are most likely derived from the secretory pathway and are independent of any viral assembly location⁵¹. DMVs are thought to help concentrate viral replication machinery and help the virus evade immune system recognition.⁵¹

Viral RNA transcription and replication are carried out by the replication-transcription complex (RTC). RTC assemble after translation of key NSP members including NSP12 (RdRp), NSP13 (helicase), NSP14 (Exon N and N7- methyltransferase), and NSP16 (2'-O-methyltransferase) (**Table 1.1**)⁵². The RTC produces two types of RNA: full-length genomic RNA and nested sub-genomic RNA⁵². Full-length genomic RNAs are used for eventual replication. In contrast, sub-genomic RNAs are thought to act as mRNA for translation of structural and accessory genes downstream of the pp1ab. Because final subgenomic and full-genomic RNAs must be (+) stranded, coronaviruses transcribe a (-) sense RNA intermediary. For full-length genomic replication, a simple full-length negative strand RNA is generated, then the RTC simply produces (+) strands from the full length (-) strand⁵².

Subgenomic RNA synthesis is more complicated^{52, 53}. In the viral genome, a Transcription Regulatory Sequence (TRS) – Leader (L) sequence is located close to the 5' end of the (+) RNA strand. Meanwhile, various TRS-B(body) sequences are scattered

between various 3' end structural/accessory open reading frames. The current leading model suggests that the RTC produces (-) sense RNA from the (+) strand but pauses at various TRS-B sequences. The RTC then skips the rest of the genome to the TRS-L sequence and then finishes transcribing from TRS-L. The result is various lengths of subgenomic (-) strand RNAs that are then re-transcribed back to (+) sense by the RTC⁵². Because all coronavirus genomic RNA contains a 3' poly(A) tail, the corresponding (-) sense genomic and subgenomic RNA intermediaries will have a 5' poly(U) heads. Such poly(U) tracts may play key roles in viral immunity as explained further below⁵⁴.

1.2 Introduction to non-structural protein 15 (NSP15)

1.2.1 NSP15 Genetic and Phylogeny Insights

Following the 2003 SARS outbreak, the coronavirus genome was heavily scrutinized⁵⁵. NSP15 was predicted to have endonuclease activity given its sequence similarity to XendoU, a *Xenopus laevis* polyU magnesium dependent endonuclease used for snoRNA processing⁵⁵. Hence, NSP15 is also known as EndoU. Interestingly, EndoU is not related to other RNase families, has some conservation in metazoans (unconfirmed in humans), has distant homologues in a cyanobacterium, and is specifically found in the *Nidovirales* order of viruses, which suggests that NSP15 is a distinct family of RNase with unanswered questions of its origin⁵⁶.

NSP15/EndoU is specific to nidoviruses.⁵⁷ However, within the order, only mammal infecting families (*Coronaviridae* and *Arteriviridae*) have endoU, while the insect and crustacean infecting viral families do not, suggesting that NSP15 could be vertebrate-specific⁵⁵. Among the coronaviruses, NSP15 orthologs are relatively conserved, especially in the N and C termini, with relatively less conservation in the middle domain⁵⁸.⁵⁹ For example, SARS-CoV-2 NSP15 has 95% protein similarity to SARS-CoV-1 and 65% similarity to MERS-CoV (**Figure 1.2**).

```

MERS/1-343      -- GLENIAFNVVKQGHFI GVEGELPVAVVNDKIFTKSGVNDICMFENKTTLPVNI AFELY
SARS-CoV-2/1-347 -MS LENVAFNVV NKGHFDGQQGEVPSIINNTVYTKVDGVDVELFENKTTLPVNVAFELW
SARS-CoV-1/1-347 HQS LENVAYNVV NKGHFDGHAGEAPVSIINNAVYTKVDGI DVEI FENKTTLPVNVAFELW

MERS/1-343      AKRAVRSHPDFKLLHNLQADI CYKFLWDYERSNIYGTA TIGVCKYTDI DVN----- SA
SARS-CoV-2/1-347 AKRNIKPVP EVKILNNLGVDIAANTVIWDYKR DAPAHISTIGVCSMTDI AKKPTETICAP
SARS-CoV-1/1-347 AKRNIKPVP EIKILNNLGVDIAANTVIWDYKR EAPAHVSTIGVCTMTDI AKKPTESACSS

MERS/1-343      LNICFDIRDNCSLEKFMSTPNAIFI SDRKIKKYPCMVGP DYAYFNGA IIRSDSVKQPVK
SARS-CoV-2/1-347 LTVFVFDGRV DGGVLDLFRNARNNGVLI TEGSVKGLQPSVGP KQASLNGVTLIGEA VKTQ---
SARS-CoV-1/1-347 LTVLFDGRV EGGVLDLFRNARNNGVLI TEGSVKGLTPSKGPAQASVNGVTLIGESVKTQ---

MERS/1-343      FYLYKKV NNEFIDPT ECIYTQSR SCSDFLPLSDMEKDFL SFDSDFVFKKYGLENYAFEHV
SARS-CoV-2/1-347 FNY YKKV DGVVQQLP ETYFTQSRNLQEFKPR SQMEIDFLELAMDEFIERYKLEGYAFEH I
SARS-CoV-1/1-347 FNY FKKV DGI IQQLP ETYFTQSR DLED FKR SQMETDFLELAMDEFIQRYKLEGYAFEH I

MERS/1-343      VYGFDSHTT LGGLHLLIGLYKRQQEGHI IMEMLKGSST IHN YFITETNTAAFKAVCSVI
SARS-CoV-2/1-347 VYGFDSHSQ LGGLHLLIGLAKRFKESPFLEDFIPMDSTVK NYFITDAQTGS SKCVCSVI
SARS-CoV-1/1-347 VYGFDSHGQ LGGLHLLMIGLAKRSQD SPLKLEDFIPMDSTVK NYFITDAQTGS SKCGCSVI

MERS/1-343      DLKLDDFVM LKSQDLGVVSKVVKVP IDLTMIEFMLWCKDGVQTFYPR LQ
SARS-CoV-2/1-347 DLLLDDFVE I IKSQDLSVVSKVVKVT IDYTEISFMLWCKDGHVETFPK LQ
SARS-CoV-1/1-347 DLLLGD FVE I IKSQDLSVI I SKVVKVT IDYAEISFMLWCKDGHVETFPK L-

```

Figure 1.2. SARS-CoV-2 NSP15 protein alignment compared to SARS-CoV-1 and MERS-CoV. SARS-CoV-2 NSP15 has 95% protein similarity to SARS-CoV-1 and 65% similarity to MERS-CoV. For SARS-CoV-2, amino acids 1-60 constitute the N-terminus, 61-190 as the middle domain, and 191-347 as the C-terminus domain. Protein Data Bank sequences SARS-CoV-2 (6VWW), SARS-CoV (2H85), MERS-CoV(5YVD) were used. Blue highlights complete conservation, while light blue highlights partial conservation of amino acids. Alignment was done with CLUSTALW. Colouring was done with JalView.

1.2.2 NSP15 Structure

The X-ray crystal structure of SARS-CoV-2 NSP15 and Cryo-EM of SARS-CoV-2 NSP15 have been elucidated^{59,60}. They confirmed the usual NSP15 three-domain structure: an N-terminal domain needed for multimerization, a middle domain, and a C-terminal catalytically active domain. In addition, SARS-CoV-2 NSP15 has similar folding and structure compared to other human coronavirus homologs (**Figure 1.3**). SARS-CoV-2 NSP15 is confirmed to exist in a hexamer formation with trimer intermediates^{59,60}. Moreover, NSP15 monomeric subunits may interact with the five other subunits, suggesting possible sensitivity to mutations or inhibitors that affect hexamerization^{59,60}. In addition, the middle domain transposes out of the hexamer, suggesting that it may have interactor activity⁵⁹. Overall, SARS-CoV-2 NSP15 folding and structure are highly similar to NSP15 homologs in other coronaviruses (**Figure 1.3**).

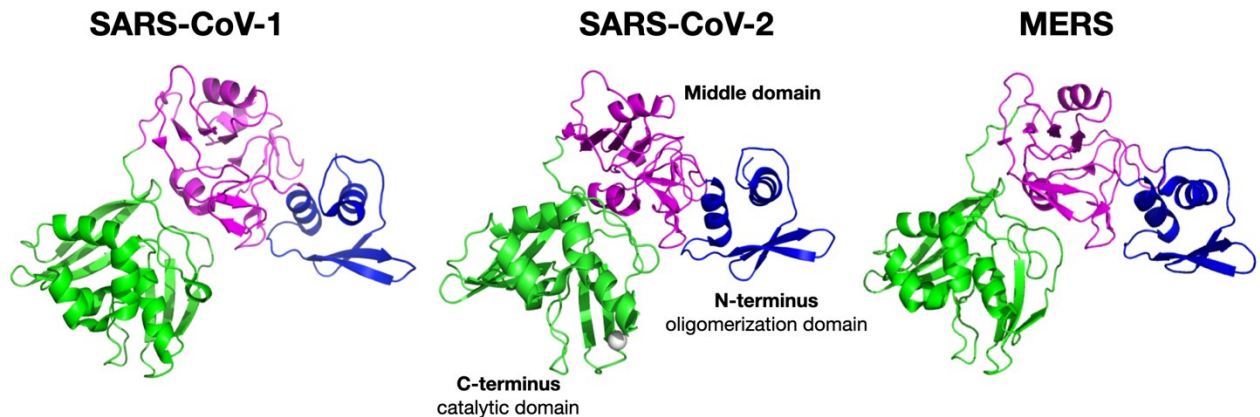


Figure 1.3: Monomeric structure of SARS-CoV-2 NSP15 compared to SARS-CoV-1 and MERS-CoV. Green indicates C-terminus catalytic domain. Magenta indicates the middle domain. Blue shows the N-terminal oligomerization domain. Protein data bank sequences SARS-CoV-2 (6VWW), SARS-CoV (2H85), MERS-CoV(5YVD) were used. The images were generated with pyMOL.

1.2.3 NSP15 has Endoribonuclease Activity

To date, all studied viral NSP15s have endonuclease activity, suggesting not only conserved sequence but also function. NSP15 endonuclease activity was first confirmed in 2004 by two independent groups using SARS-CoV-1 NSP15^{58,61}. NSP15 was found to cleave ssRNA and dsRNA, but not ssDNA or dsDNA, at single uridine or poly-uridine positions, yielding a 2'-3' cyclic phosphate end^{58,61,62}. In addition, NSP15 was shown to require divalent ions and prefers manganese, when compared to other ions like magnesium, calcium, or zinc⁵⁸. It was shown that 5' or 3' termini modifications of the RNA had no effect on NSP15 activity⁵⁸. Interestingly, 2'-O-ribose methylated RNA was shown to block NSP15 cleavage.⁶¹ Later studies revealed that the NSP15 hexameric form is likely its active form^{63,64}. In addition, NSP15 cleaves specifically at the 3' end of uridylate, with minor cleavage at 3'cytidylate, and such cleavage may be affected by RNA loop structures⁶². Overall, NSP15 is canonically characterized as an RNA uridine-specific endoribonuclease.

1.3 Coronavirus and the Immune System

NSP15 has been implicated in immune evasion. I will briefly describe the relevant immune pathways before discussing NSP15's role in them.

1.3.1 Interferon Response Types

There are three types of mammalian interferons (IFN): type I (IFN- α/β), type II (IFN- γ), and type III (IFN- λ)^{65,66}.

Type I IFN is a large family of proteins which includes 13-14 subtypes including IFN- α , IFN- β , and various others including IFN- ϵ , - κ , - τ , - δ , - ζ , - ω , - ν ⁶⁵. When RNA/DNA pathogen-associated molecular pattern (PAMP) detecting pathways are activated, canonically, the pathways converge on the TBK1/IKK ϵ kinase phosphorylation of interferon regulatory [transcription] factors (IRF)-3 and 7. Phosphorylated IRF3/7 binds to canonical interferon response element sequence (IRES) in IFN- α/β promoters, thereby activating IFN- α/β transcription⁶⁷. While IRF3 is ubiquitously expressed, IRF7 is restricted predominately to plasmacytoid dendritic cells (pDCs)⁶⁷. Following IRF3/7 activation, IFNs- α/β are produced and secreted from the cells. Secreted IFN- α/β binds to transmembrane type I IFN receptor (IFNAR), composed of IFNAR1 and IFNAR2. Dimerized IFNAR1/2 receptor activates the JAK/STAT pathway, ultimately leading to the transcription (with the help of IRF9) of type I interferon-stimulated genes (ISGs)^{65,67}. Over 300 ISGs are identified contributing to various functions including, but not limited to inflammation, signalling and its modulation, such as the activation, recruitment, and regulation of dendritic, macrophages, and natural killer cells⁶⁵. During infection, type I IFN- β is detected first as early less than 24 hours post infection⁶⁵.

Type II IFN (IFN- γ) is structurally unrelated to Type I IFN, consisting of just IFN- γ , and is produced predominantly by natural killer and innate lymphoid type 1 cells. In addition, IFN- γ signals through a different receptor, the IFN- γ receptor (IFNGR)⁶⁵. While IFN- γ is important (especially for macrophage and antigen presentation), IFN- γ has not yet been directly implicated with NSP15^{68,69}.

Type III IFN (IFN- λ) is a relatively newer interferon type (founded in 2003) and acts similarly to Type I IFN but is targeted towards viral infections of primarily mucous epithelial cells, alongside other roles in hepatocytes and gut epithelial cells⁶⁶. IFN- λ consists of four members (IFN- λ 1/2/3/4) and activates IFNLR receptors (named after IFN- λ 's alternative nomenclature IFNL). IFNLR receptors subsequently acts upon the JAK/STAT pathway for downstream ISG activation⁶⁶. Early studies suggest that IFN- λ activates the same transcription factors as IFN- α/β , chiefly IRF3 and IRF7, and can be co-expressed at the same time. However, later studies suggest different mechanisms may activate type III IFN⁶⁶. Whereas Type I IFN its generally considered to induce a rapid induction and decline of ISGs, Type III IFN induced ISG is less rapid but more long-lasting despite sharing similar ISG signatures^{66,70}.

Overall, IFNs play an important role in the innate immune pathway. Below, I discuss the various upstream IFN activating pathways.

1.3.2 The RIG-I-Like Receptor (RLR) Family: RIG-I and MDA5

The RIG-I-Like Receptor (RLR) family senses cytoplasmic viral RNA PAMPS and triggers IFN- α/β response. The RLR family includes: 1) retinoic acid-inducible gene I (RIG-I), 2) melanoma differentiation-associated gene 5 (MDA5), and 3) laboratory of genetics and physiology 2 (LGP2)^{71,72}. LGP2 acts as a regulator that attenuates RIG-I reaction while enhancing MDA5⁷². Being from the same family, both RIG-I and MDA5 share the crucial ATP-dependent DExD/H box RNA center helicase domain that helps viral RNA recognition and binding. Upon binding, both RIG-I and MDA5 homo-oligomerize (i.e., RIG-I recruits more RIG-I on the RNA). Canonically, this oligomerization activates their N-terminal caspase activation and recruitment (CARD) domain. Activated CARD domain binds to and activates the mitochondrial antiviral signalling (MAVS) protein on the mitochondria^{73,71}. Activated MAVS triggers a signaling cascade involving TBK1/IKK ϵ kinase complex, which phosphorylates transcription factors IRF3/7, leading to a multitude of type 1 IFN gene activations and also a positive feedback loop for increased MDA5 transcription^{71,73}. In addition, MDA5 induced MAVS activation also stimulates apoptosis of the infected cell⁷³.

Despite a relatively shared pathway, RIG-I and MDA5 share some differences. RIG-I seems to respond well to negative-strand RNA, while MDA5 responds well to positive-stranded RNA such as coronaviruses⁷¹. At the same time, RIG-I binds to shorter dsRNAs with 5' tri-phosphorylation, whereas MDA5 prefers longer dsRNA, including blunt end RNAs^{74,71}.

1.3.3 Endosomal Toll-Like Receptors

Human Toll-like Receptors (TLR) comprise ten members. Of interest are TLR3, TLR7, and TLR8, which are located in endosomal membranes and can detect viral, bacterial, and self-made RNA⁷⁵. TLR3 detects dsRNA while TLR7 and TLR8 detect ssRNA. TLR7 is predominantly expressed in plasmacytoid dendritic cells (pDC) and plays a major role in sensing coronavirus infections. All TLRs have a Toll/IL-1 (TIR) domain which binds to either two major adaptor proteins: MyD88 for TLR7/8, or TRIF for TLR3, to initiate downstream signaling⁷⁵. For the MyD88 pathway, the IKK complex (composed of IKK α/β , and IKK γ) is eventually activated, leading to phosphorylation of the NF- κ B inhibitor I κ B α , and the translocation of NF- κ B into the nucleus for pro-inflammatory cytokine production. NF- κ B-induced production includes: TNF- α , IL-1 β , IL-6, IL-12p40 and cyclooxygenase-2, of which TNF- α is highly important for M1 macrophage induction⁷⁶. For the TRIF dependent pathway, TRIF activates TBK1 and IKKi for IRF3 phosphorylation and induction of IFN genes. As a result, IFN I/III genes can be activated by both RIG-I/MDA5 pathways and the TLR pathways⁷⁵.

1.3.4 Protein Kinase R (PKR) pathway

The double-stranded RNA-dependent protein kinase (PKR) recognizes viral dsRNA, and its subsequent homodimerization phosphorylates the alpha subunit of eukaryotic initiation factor 2 (eIF2 α), a translation factor⁷⁷. Phosphorylated eIF2 α prevents its recycling needed for further translation initiation and causes a breakdown in viral translation. Cellular translation inhibition is prevented by discrete PKR localization. PKR has also been shown to activate the NF- κ B pathway via activation of IKK α/β . Activation

of PKR has been shown to induce apoptosis via NF- κ B and various other pathways such as P53, ATF-3, APAF/Caspase9⁷⁷.

1.3.5 Oligoadenylate Synthetase (OAS) / RNase L Pathway

Oligoadenylate synthetases (OAS) are a family of 3 proteins (OAS1/2/3) that are considered interferon-stimulated genes (ISGs) (and thus are downstream of interferon activation)⁷⁸. In infected cells, OAS synthesizes 2'-5' oligoadenylates (2-5A) from ATP. 2-5A binds and activates dimerization of RNase L, a ubiquitously expressed ssRNA (UN^N) RNase. RNaseL subsequently cleaves viral and cellular ssRNA, including 18S rRNA⁷⁹. Cleaved fragments may also act as a feedback loop for further interferon signalling.

1.4 NSP15 Function in Coronavirus Infection

1.4.1 NSP15's Role in Evading Interferon Defence

Emerging evidence suggests that NSP15 plays a key role in host immune evasion. The first clue for NSP15 function *in-vivo* came from the coronavirus, mouse hepatitis virus (MHV), whose NSP15 was found to localize to defined double membrane vesicles which house defined members of the replication transcription complex (RTC), including nsp8 and nsp12, but not any membrane (M) proteins⁸⁰. This finding suggested that NSP15 function could be regulated by localization and is tightly in sync with the viral replication complex.

In 2017, NSP15 was found to be directly implicated in interferon (IFN) response, OAS/Rnase L, and potentially the PKR pathway. Using NSP15 catalytic deficient mouse hepatitis virus (MHV) virus strain, NSP15 deficiency was shown to attenuate viral replication and spread *in-vivo* in mice⁴⁰. In both MHV and Human Coronavirus 299E (HCoV-299E), NSP15 catalytic mutations resulted in increased IFN- β expression in primary murine embryonic fibroblasts (MEFs) and blood-derived macrophages⁴⁰. In the same study, NSP15 deficient viruses were also shown to be sensitive to IFN-I treatment.

NSP15 deficiency also caused a decrease in rRNA, a marker for the OAS/Rnase L pathway, and this effect was shown to be reversed by a Rnase L mutation in macrophages⁴⁰. Additionally, the study found that NSP15 deficiency increased eIF2 α translation inhibition compared to wildtype, suggesting involvement in PKR pathway activation⁴⁰. Interestingly, the same study found that MDA5, OAS/Rnase L, or PKR deficient macrophages alone could fully restore NSP15 deficient MHV replication, suggesting that all three pathways play a role in inhibiting NSP15 deficient viral replication. Lastly, the same study found that NSP15 deficiency caused an accumulation of dsRNA in the cytoplasm, a trigger for MDA5, OAS/Rnase L and PKR pathway activation⁴⁰.

Also in 2017, NSP15 was separately shown to be essential for viral immune evasion⁵. In particular, defective NSP15 in mouse hepatitis virus (MHV) led to decreased viral titer, increased IFN- α production, and increased apoptosis in mouse bone-derived macrophages (BMDMs)⁵. In the same work, it was demonstrated that viral titer was restored when defective NSP15 virus was infected in interferon- α/β receptor negative (*ifnar*)^{-/-} bone marrow derived macrophages⁵. Moreover, mutant NSP15 infection activated the MDA5, PKR (via increased eIF2 α phosphorylation), and OAS/Rnase L system (via increased RNA degradation) compared to wildtype NSP15 virus. Furthermore, mutant NSP15 showed a decoupling of replication complex foci from dsRNA foci using immunofluorescence⁵. Most interestingly, the same study found that a single point mutation in NSP15 caused viral attenuation when injected into mice, leading to a 100% survival rate compared to wildtype virus, and even elicited protective immunity against subsequent wildtype viral injections⁵. These results strongly demonstrated the importance of NSP15 in viral-mediated immune evasion.

In regards to how NSP15 might help with *in-vivo* viral immune evasion, a study in 2020 found that NSP15 cleaved negative-sense viral RNA (termed PUN RNA) and it was established that such PUN RNAs are MDA5 activating RNA pathogen-associated molecular pattern³⁹. The study found that catalytically defective NSP15 (H262A) in MHV, was shown to cause higher dsRNA foci accumulation in mouse hepatocyte (AML12) cells using immunofluorescence techniques against a dsRNA recognizing antibody³⁹.

Subsequent pulldown and sequencing of the antibody-bound RNA revealed predominant negative-sense viral RNAs in *ifnar*^{-/-} BMDMs, and AML12 cells³⁹. In the study, quantitative-polymerase chain reaction (qPCR), using sequence-specific primers, found that NSP15 mutation increased both the abundance and length of poly(U) (PUN) RNA in MHV infected AML12 and *ifnar*^{-/-} BMDMs, as well as in α -CoV porcine epidemic diarrhea virus (PEDV) in porcine kidney epithelial (PK1) and Vero cells³⁹. Additionally, no changes in abundance of positive-stranded polyA tail were detected during mutant NSP15 MHV infection. Subsequent *in-vitro* cleavage assays confirmed that NSP15 cleaved PUN RNAs. Lastly, using AML12 cells, the study found that the poly(U) tail of PUN RNA was necessary but not solely sufficient to induce a 2000 fold increase in IFN β 1 (Type I interferon) expression³⁹. Such IFN β 1 response was not apparent in MDA5-knockdown cells. Therefore, the evidence suggested that NSP15 modulates immune evasion by cleavage of viral polyU RNA.

Recently, a study in 2021 found that NSP15 cleaved internal viral RNA sites⁸¹. Cyclic phosphate sequencing of MHV NSP15 cleavage ends in bone marrow-derived macrophages revealed a strong preference for sites containing both “U’A” and “C’A” sequences⁸¹. This finding was surprising since previous biochemical NSP15 assays revealed a strong preference for uracil cleavage only and only a minor preference for cytidine⁵⁸. Furthermore, these cleavage sites were spread out throughout the MHV RNA, especially in transcriptional regulatory sequences (TRS) and the 5’ and 3’ non-translated region (NTR) of the positive strand⁸¹. While previous studies suggested that NSP15 potentially cleaves the 5’ poly(U) heads of negative-stranded viral RNA, this study did not reveal such cleavage sites, but instead revealed cleavage sites of two ‘CA’ nucleotides adjacent to the poly(A) tail of the positive strand^{39,58}. Although the study found that the NSP15 cleavage sites shared overlap with Rnase L cleavage sites, NSP15 does not target 18S rRNA, unlike Rnase L⁵⁸. From the sequencing data, NSP15 seemed to prevent the formation of dsRNA, not through polyU tail cleavage, but through cleavage of the positive-strand RNA to prevent negative-strand synthesis. Since NSP15 was known to interact with the replication complex, including polymerase (nsp12) and its cofactors (nsp7 and 8), it was hypothesized that during negative-stranded synthesis, NSP15 would

also cleave the positive strand in order to prevent dsRNA formation and help evade dsRNA host interferon responses⁸⁰. Such events may be regulated by NSP16's 2-O-methylation of key cleavage sites, which were shown to block NSP15 cleavage⁶¹. Additionally, due to shared cleavage site overlap between Rnase L and NSP15, and the fact that Rnase L^{-/-} cells caused a decrease in NSP15 expression, a complex interplay between Rnase L and NSP15 may be occurring to regulate viral expression and host immune response⁸¹. Further research would be needed to pinpoint the mechanism of NSP15 function *in-vivo*.

Overall, it appears that NSP15, in the various coronaviruses studied prior to COVID-19, is an essential protein for coronavirus infection. During viral replication, NSP15 localizes to the replication complex and may use its endonuclease activity to help degrade either the 5' Poly(U) head of the negative-strand RNA, and/or the positive-strand viral genomic RNA. Through this nuclease activity, dsRNA formation and host immune response activation is suppressed/prevented. Thus, through these mechanisms, NSP15 is essential to viral infection.

1.4.2 Alternative NSP15 Mechanisms

While there is evidence that NSP15 helps evade the immune system via its endonuclease activity, other mechanisms could be possible. In porcine delta-coronavirus (PDCoV), NSP15 was found to act as a dimer and impair NF- κ B in an endonuclease-independent manner^{82,83}. While the exact mechanism of impairment was unclear, such impairment has not been explored in other models, and thus it is currently unclear if this is porcine virus specific.

Additionally, SARS-CoV-1 NSP15 has been shown to interact with retinoblastoma protein (pRb), a known tumor suppressor, and repressor of transcription factor E2F1⁸⁴. A retinoblastoma protein-binding motif (LXCXE/D) was detected in SARS-CoV-1, and NSP15 co-immunoprecipitated with pRb in 293T cells⁸⁴. NSP15 expression, including the use of endonuclease deficient NSP15, caused cytoplasmic translocation of cellular pRb, increased foci growth in contact independent focus formation assay, increased expression of (pRb repressed) thymidine kinase promoter gene and an overall

downregulation of pRb abundance⁸⁴. A mutation in the LXCXE/D domain of NSP15 caused a 1-5 log decrease in MHV viral titer, and increased cell death and apoptosis⁸⁴. Overall, these results suggested that NSP15 has an endonuclease-independent function via interaction with pRb⁸⁴. Interestingly, such (LXCXE/D) motifs were also found in DNA tumour viruses such as with proteins adenovirus E1a, simian virus 40 T antigen, and human papillomavirus E7, suggesting that inhibition of pRb is an important strategy to various viral infections⁸⁵.

In SARS-CoV-1, NSP15 has also been implicated in MAVS-dependent apoptosis⁸⁶. It was shown that expression of full-length MAVS triggered apoptosis and that this phenotype was independent of type I IFN pathways⁸⁶. A functional screen of MAVS-dependent apoptosis found only SARS-CoV-1 NSP15 to be a potent inhibitor of apoptosis. Repression of apoptosis is thought to be beneficial for viral replication⁸⁷. Interestingly, NSP15 in human coronavirus HKU1, and human coronavirus NL63, could not recreate the apoptosis repression phenotype, suggesting that it was SARS-CoV-1 specific⁸⁷. To what extent this phenomenon relies on NSP15 endonuclease function, and its relevance in physiological infection, requires more research.

1.5 Effect of NSP15 on Viral Titers in Cell Culture

Previously, defective NSP15 was found to have caused severe attenuation of viral replication in mice *in-vivo*^{5, 40}. However, the data for NSP15's effects in cell culture becomes more nuanced.

For the coronavirus mouse hepatitis virus (MHV), in cell culture, NSP15's effect on replication (viral titer) seems to be cell line dependent. In an earlier study, catalytic mutant MHV NSP15 (H262A) caused a ~1.5 log decrease in plaque forming units (PFU) at 0.5 multiplicity of infection (m.o.i) and ~0.8 log decrease at 1.5 m.o.i in fibroblast baby hamster kidney cells (BHK-R)⁸⁸. In another study, MHV NSP15 H262A mutant caused a ~1.8 log decrease in viral titers in BMDM cells and, and to a lesser extent, a ~1 log decrease in fibroblast 17CI-1 cells⁵. This study concluded that MHV NSP15 was not needed for viral replication in 17CI-1 fibroblast cell lines and that replication defects in

BMDMs were due to subsequent interferon defenses. On the other hand, MHV NSP15 H277A mutant was shown to produce a viral titer peak of $\sim <0.5$ log decrease compared to wildtype at 1 m.o.i but no difference in viral titer peak at 0.1 m.o.i in fibroblast L929 cells. The same NSP15 H277A mutant restricted viral titer by ~ 1 log in primary murine embryonic fibroblast (MEF) and a larger ~ 2 log decrease in viral titers in bone marrow-derived murine macrophages. In contrast, in epithelial AML12 cells, catalytic defective NSP15 MHV viruses (H262A) did not produce viral replication defects but did induce Type I (IFN β 1) and Type III (IFN λ) interferon defence³⁹. In fact, at eight hours post-infection, defective NSP15 caused a near-significant ($p=0.008$) increase (<0.3 log) in viral titers. Overall, mutant MHV NSP15 seemed to cause decreased viral titers mostly in bone marrow-derived macrophages (BMDM), and to a lesser extent in certain fibroblast-derived cells (MEF and 17CI-1)⁵. Defective NSP15 appeared to have no effect on viral titer in AML12 cells³⁹.

In HCoV-299E, it was shown that catalytically defective NSP15 (H250A) produced a ~ 2.5 log decrease in viral titer in human-derived blood macrophages. In MERS, early data suggested no viral titer change with catalytically defective NSP15 (H231A), but was accompanied by a significant increase in interferon markers (IFNL1, IFNB) in epithelial a549-dpp4 cells⁸⁹. No work has tested the effect of NSP15 mutation in SARS-CoV-1 or 2 viruses on viral replication in *in-vitro* cell lines. Thus, it appears that NSP15's effect on viral replication in *in-vitro* cell culture is cell-type specific and could also be dependent on the coronavirus used.

1.6 SARS-CoV-2 NSP15 and SARS-CoV-2 Interferon Defenses

1.6.1 Interferon Screens

Only a few papers have investigated NSP15 in SARS-CoV-2. SARS-CoV-2 interferon screens have implicated NSP15 as an IFN β antagonist using 293FT cells following RIG-I stimulation and in HEK293T cells stimulated with MAVS^{6,7}. On the contrary, numerous other interferon screens have not demonstrated a role for NSP15 in SARS-CoV-2 interferon response. These included interferon screens using Calu-3 cells stimulated with

Sendai Virus and Poly(I:C)⁵⁰, HEK293T with RIG-I-CARD stimulation⁹⁰ and HEK293T stimulated with Sendai virus^{91,92}.

1.6.2 Autophagy

SARS-CoV-2 NSP15 overexpression in HEK293T was found to have inhibited the induction of autophagy, and was found to cause a corresponding reduction in autophagosome numbers⁹². In contrast, ORF3a, E, M and ORF7a inhibited autophagosome turnover as they increased autophagosome number⁹². To account for this, the researchers performed wildtype SARS-CoV-2 infection in Calu-3 and Caco-2 cells, and found that levels of p62 (degraded after autophagosome-lysosome fusion) and processed LC3B (markers of late-stage autophagosomes) were increased, suggesting that blockage of autophagosome turnover is the predominant phenotype in infection. Indeed, ORF3a was found to block autophagosome-lysosome fusion, and ORF7a blocks autophagosome acidification⁹². As a result, to what extent NSP15 is needed by SARS-CoV-2 during physiological infection to block autophagy induction remains to be seen.

1.6.3 SARS-CoV-2 Interferon Defense

Interestingly, SARS-CoV-2 NSP15 was found to be a less potent interferon antagonist than the corresponding NSP15 protein in SARS-CoV-1, being 32-fold less potent than SARS-CoV-1 and 7.8-fold less than RaTG13-CoV NSP15 in decreasing IFNB1 levels in 293T cells⁹². These results suggest that the *in-vivo* effectiveness of NSP15 as an immune antagonist may be evolving.

Indeed, the overall biology of SARS-CoV-interferon immune induction seems to be altered compared to other coronaviruses. It was reported that SARS-CoV-2 has unique interferon responses depending on the cell type⁹³. In patient-derived epithelial cells and cardiomyocytes, IFN and OAS/Rnase L activation was not observed, but PKR activation was present⁹³. In contrast, in cell culture with Calu-3 and A549-ACE2 lung-derived cells, weak IFN-I activation was observed, but OAS/Rnase L and PKR pathways were also activated⁹³. This contrasts with MERS, which strongly inhibits OAS/Rnase L and PKR pathway activation in the same cell culture lines⁹³. Whether this is the result of altered

NSP15 functions is debatable given the numerous other proteins involved in interferon antagonism. More research is needed to find the extent of NSP15 function in SARS-CoV-2 and how that relates to other immune antagonists.

1.7 NSP15 Inhibitors

Because NSP15 plays a key role in coronavirus infection, pharmacological agents targeting NSP15 could be promising for the treatment of SARS-CoV-2. This hypothesis was particularly bolstered by the fact that mutations in NSP15 completely abolished viral replication in murine models⁵. In 2010, RNase A inhibitors were found to also inhibit NSP15⁸. Congo Red and BenzopurpurinB inhibited NSP15 *in-vitro* and modestly decreased Sars-CoV-1 infection in Vero cells at 100 μ M⁸. Unfortunately, these compounds are unlikely to be drug candidates given their structural properties and weak potency.

In 2020, given the heightened interest of NSP15 in COVID-19, various *in-silico* computational screens also identified potential NSP15 inhibitors but without follow-up in *in-vitro* assays⁹⁴⁻⁹⁶. Recently, betulonic acid derivatives was discovered to be a potent HCoV-299 NSP15 inhibitor⁹⁷. However, the same inhibitor was inactive against SARS-CoV-2. The compound was not computationally predicted to bind to SARS-CoV-2 NSP15⁹⁷. Nevertheless, the result provided evidence on the effectiveness of targeting NSP15, albeit in HCoV-299E⁹⁷.

To date, few studies have identified SARS-CoV-2 NSP15 inhibitors. Tipiracil, a uracil derivative used in anti-cancer treatment as a blocker to thymidine phosphorylase, has been predicted to bind to the active site of NSP15⁹. Tipiracil inhibited NSP15 cleavage *in-vitro* but only showed modest and barely significant (~20%) inhibition of SARS-CoV-2 virus at the highest dose (50 μ M) tested. As a result, the compound is unlikely to be used therapeutically, but Tipiracil and uracil derivatives may be a viable starting point for future drug developments. In another recent study, Exebryl-1, a small-molecule initially tested for inhibition of beta-amyloid in Alzheimer disease, was shown to bind to NSP15 and inhibited RNA cleavage¹⁰. Exebryl-1 demonstrated SARS-CoV-2 viral replication

inhibition at an IC₅₀ of 65.6 μM and with a CC₅₀ above 100 μM in Vero cells. However, it has limited therapeutic potential as it is toxic in other cell lines, and previous studies have shown that an 100mg/kg oral dose in rats resulted in only 4 μM plasma levels after four hours¹⁰. However, Exebryl-1 could be a lead in future drug designs. Recently, a 5000-compound chemical screen found compound NSC95397, a cell division control 25 (Cdc25) protein phosphatase and multiple kinase inhibitor⁹⁸. This compound inhibited NSP15 in biochemical assays with an IC₅₀ of 43 μM. However, the compound produced no effect on SARS-CoV-2 viral titer in Vero cells⁹⁸. To date, there are no safe and effective SARS-CoV-2 NSP15 inhibitors identified.

1.8 High-throughput Screening of Small-Molecules

Because of the lack of potent and safe SARS-CoV-2 NSP15 inhibitors available, more research is needed to find potential NSP15 binding agents. High-throughput (HTP) screening is a common method to identify new pharmacological reagents and has been successful in finding enzyme inhibitors in numerous contexts with examples below. Screening of enzymes similar to NSP15 such as Rnases of viral *Sweet potato chlorotic stunt virus* (CSR3) Rnase III⁹⁹, HIV Rnase H¹⁰⁰, Rnase H2¹⁰¹, have successfully identified hits, often using FRET-based RNA cleavage assays. High-throughput screening guidelines and protocols have also been extensively established¹⁰². One advantage of a well-designed HTP screen is that they can identify novel classes of ligands that are not restricted to known or main binding/enzyme sites, unlike rational drug or structural-based drug discovery. While high-throughput screening may not yield tight-binding inhibitors initially, post-screen compound optimizations can also drastically improve compound binding. One example was the lead optimization of inhibitor for Beta secretase (BACE1) for Alzheimer's disease, in which lead optimization of the molecule improved the compound IC₅₀ from 73,000 nM to 59 nM¹⁰³. This example shows the effectiveness of HTP screening as a part of a hit-to-lead pipeline. For NSP15, putative NSP15 inhibitors, Exebryl-1 and NSC95397 were discovered through high-throughput screening of NSP15 using a FRET-based RNA substrate system similar to this study's

setup, detailed below^{10, 98}. Because of these reasons, I started this project through a large HTP screen of over 100,000 compounds.

CHAPTER 2: Materials and Methods for Screening for NSP15 Inhibitors

2.0 General Reagents

All polymerase chain reactions (PCR) were done with Q5 High Fidelity DNA polymerase (NEB, Canada). Gel extractions were done with the QIAquick Gel extraction kit (Qiagen, Canada). All plasmid extractions were done with QIAprep Spin Miniprep Kit (Qiagen, Canada). Sanger sequencing was done at Alberta Transplant Applied Genomics Centre (ATGC) at the University of Alberta, Canada. All primers were purchased from Integrated DNA Technologies (IDT, USA). Compounds containing the “CID” header were purchased from Hit2lead, ChemBridge (USA). BenzopururinB was purchased from MP Biomedicals (USA). Hexachlorophene was purchased from Sellekchem (USA). IPA3 and Reactive Blue 2 were purchased from MedChemExpress (USA). DH5-alpha competent *E.coli* cells (NEB, Canada) were used for all cloning/plasmid construction experiments.

2.1 NSP15 Cloning

The sequence encoding wild-type SARS-CoV-2 NSP15 protein (PDB: 6VWW)¹⁰⁴ was codon optimized for bacterial expression and purchased as a custom gene synthesis plasmid from IDT (USA) (**Table 2.1**). This sequence was PCR amplified, using primers found in **Table 2.2**, and inserted into a pET-based vector (derived from pC013, Addgene #90097) using the NEBuilder HiFi DNA assembly cloning kit (NEB, Canada), according to the manufacturer’s instructions. The resulting construct was verified by Sanger sequencing using T7 primers (**Table 2.2**). The $\Delta 0-28 \Delta 336-347$ NSP15 mutant construct was prepared in a similar fashion using its specific primers (**Table 2.2**). To prepare the NSP15 H250A mutant, Q5 Site-directed mutagenesis (NEB, Canada) was performed on the wildtype NSP15 construct using NSP15 H250A SDM Primers FWD and REV (**Table 2.2**), as per the manufacturer’s instructions. This plasmid was also validated by sanger sequencing.

Table 2.1: NSP15 codon optimized sequence. The original sequence, 6VWW, was taken from protein data bank (PDB). The IDT codon optimization tool was used to optimize the sequence for expression in *Escherichia coli*.

<p>5'- atgggcagcagccatcatcatcatcacagcagcggcggtggatcttggtagcggaaaatctgtactttcaatccaatgc catgctgtagagaacgtagctttaaactggtgaacaaaggccattttgatgggtcaacagggagaagtccagtgccat tataacaatacgggtatacaccaaagtggacgggtagatgtagaactgttgagaataagacgactttaccagtgat gtagcttctgagttgtgggctaagagaaacatcaagccagtaccggaagtaagattttaaataatctgggtagacatt gctgcaaatactgtcatctgggactataaacgggacgcgccgcacatactcaactatcggcgttgcagatgacaga tatagcgaaaaagccgacggaaaccatattgtgcacccttgaccgtttctcgatggtcgggtggatggtcaggtcgatt attcagaaatgctcgaatggagtctgattactgaggggagtgtaaaaggattacaaccatcagtgggaccgaaaca ggctcccttaatgggtgtacgcttactcgggtgagggcggtaaagacacagttcaattattacaaaaagggtggacggcgtcgt acaacagttacgtgaaacttactttacgcagtcgagaaactgcaggaattcaagccgctccagatggaaattgatt tctggagctggctatggacgaattatcgaaagataagctggaaggatattgcttgcacataatagtagcgggatttt ctcattcgcaactgggtggccttcatctttaaaggcttagcgaagcgttcaaggaatctcctttgagtagaagactttatt ccgatggactccaccgttaagaactattcattacagatgcacagacgggtctagcaaatgtgatgctctgtaattgacct gtttagacgactttgcgaaattatcaaaagccaggacctgtccgtagtctcgaagggttgaaagtgaccatcgacta cacagagatatcctttatgctttgggtgcaaggatggtcacgttgaacaattttatccaagctgcagtaa-3'</p>
--

Table 2.2: Primers for NSP15 cloning and sequencing.

Name	Sequence
NSP15 Wildtype Primers FWD	5'- ATCATCATCACAGCAGCGGCCGTGGATCTTGGTACGGAAAATC- 3'
NSP15 Wildtype Primers REV	5'-GCCTCGAGTGCGGCCGCTTACTGCAGCTTGGGATAAAATG- 3'
PC013 Vector FWD	5'-TAAGCGGCCGCACTCGAG-3'
PC013 Vector REV	5'-GCCGCTGCTGTGATGATG-3'
Δ0-28 Δ336-347 FWD	5'- TGTACTTTCAATCCAATGCCAACAATACGGTATACACCAAAG- 3'
Δ0-28 Δ336-347 Primer REV	5'-ATCCTTGCACCAAAGCATAAAG-3'

NSP15 H250A SDM Primer FWD	5'-GGGTGGCCTTGCTCTTTTAATAGG-3'
NSP15 H250A SDM Primer REV	5'-CTAAAAAGAGTAAGCGTTGA-3'
T7 FWD	5'-TAATACGACTCACTATAGGG-3'
T7 REV	5'-GCTAGTTATTGCTCAGCGG-3'

2.2 NSP15 Protein Purification

Wild-type and mutant NSP15 proteins were purified as previously described, with several modifications.¹⁰⁴ Briefly, BL21(DE3)pLYsS cells (Promega, Canada) were transformed with plasmids encoding NSP15. Starter cultures were grown overnight (~16 hrs) at 37°C with 5 mL of Difco Luria Broth (LB)(BD,USA) in the presence of 50 µg/mL carbenicillin. 1mL of this culture was then used to inoculate 2 L of Luria broth (LB) with carbenicillin, and this culture was grown as above until an OD₆₀₀ of 0.6 was reached. Following this, isopropyl-β-D-1-thiogalactopyranoside (IPTG) was added to a final concentration of 1mM and the culture was incubated at 18°C overnight. Cells were pelleted by centrifugation at 3500g for 15 minutes and resuspended in lysis buffer (20 mM Tris-Cl, pH 7.5, 250 mM NaCl, 5 mM imidazole, pH 8.0) supplemented with Roche Complete Ultra protease inhibitor (Sigma, Canada) and 0.1 M phenylmethylsulfonyl fluoride (PMSF). The mixture was incubated on ice for 30 minutes before being sonicated (15 second pulse-on and 59 second pulse-off for a total of 15 minutes at 55% amplitude). Cellular debris was pelleted by centrifuging at 28,000g for 1 hour. Next, the lysate was collected and subject to filtering through a 0.45 µM PVDF membrane. The filtered lysate was loaded onto a 1 mL HisTrap HP column (Sigma, Canada) and purified using an AKTA Start System (Cytiva, USA). The column was washed with buffer (20 mM Tris-Cl, pH 8.0, 250 mM NaCl, 10 mM imidazole, pH 8.0) until UV-baseline was reached, and subsequently eluted in gradient fashion. The final elution buffer was comprised of 20 mM Tris-Cl, pH 8.0, 250 mM NaCl, 250 mM imidazole, pH 8.0. Pooled protein fractions of high purity were concentrated with a Peirce Protein concentrator 10K (Thermo, Canada). During

concentration, the buffer was exchanged with 20 mM HEPES-KOH, pH 7.5, 500 mM NaCl, 1 mM DTT, 10% glycerol. Concentrated protein was aliquoted and stored at -80°C until usage. Protein concentration was measured using the DTT-resistant Peirce 660 nm Protein BCA Assay kit (Thermo, Canada).

2.3 NSP15 Fluorescent Activity Assay

I adapted a previously described fluorescence resonance energy transfer (FRET)-based assay. This assay employed a uracil-containing RNA substrate that is flanked by fluorophore and quencher pair.⁶² Sequences for the substrates are listed in **Table 2.3**. Reactions were set up in black 96 well flat-bottom polystyrene plates (Corning, USA) in 60 µl volume. The reaction buffer contained 25 mM HEPES, 50 mM NaCl, 5 mM MnCl₂, and 1 mM DTT. Final reaction concentrations of 1 ng/µl NSP15 and 1 µM RNA substrate were used unless otherwise stated. Where applicable, compounds were dissolved in DMSO before being added to the reaction. DMSO concentrations were kept to less than 1%. Reactions were started with the addition of RNA, and incubated at 37°C for the indicated times, and read at excitation/emission wavelengths of 490/520 nm for FAM or 645/670nm for Cy5 using a SpectraMax i3x spectrophotometer (Molecular Devices, USA).

Table 2.3 RNA substrate sequences for NSP15 activity assay.

Name	Sequence	Sequence Source
Positive control FAM RNA	5'-FAM-rArArArArArArArG-U'3	N/A
Negative control RNA	5'-FAM-rArArArArArArArGrArArArArArA-BHQ1-'3	N/A
RNA1	5'-FAM-rArArArArArArArGrUrArArArArA-BHQ1-'3	105
RNA2	5'-FAM-rCrArArCrUrArArArCrGrArArC-BHQ1-'3	63
RNA3	5'-FAM-dAdArUdAdA-BHQ1-'3	62
Cy5 RNA	5'-FAM-rCrArArCrUrArArArCrGrArArC-BHQ2-'3	63

Positive Control Cy5 RNA	5'-Cy5-rCrArArCrU-'3	N/A
--------------------------	----------------------	-----

2.4 High-Throughput Screening

Screening was performed at the High Content Analysis Core facility at the University of Alberta and at the Biofactorial Facility at the University of British Columbia. The library of compounds screened was comprised of roughly 30,000 compounds from the Canadian Chemical Biology Network (CCBN) collection, 1280 from LOPAC, 3040 from the TimTec collection, 50,000 from the Chembridge DIVERSet collection, and 24,000 Chembridge compounds from the GlycoNet collection. Compound overlap between the collections was <0.1%. Reagents were distributed into 384-well black flat bottom plates (Greiner, USA) using either a JANUS 384-well liquid handling system (PerkinElmer, USA) or an Echo acoustic dispenser (Beckman Coulter, USA). The reaction setup was similar to that described above, in which the final concentration of NSP15 was 1 ng/μL, and RNA was 0.5 μM. The reaction volume was 20 μl. Sequences for the positive control, RNA2, and Cy5 RNA substrates are listed in **Table 2.3**. Compounds were dissolved in DMSO and screened at a final concentration of 10 μM. DMSO without any inhibitors was used as a positive control, and either 100 μM of BenzopurpurinB or a reaction without NSP15 was used as a negative control. Readings were taken at excitation/emission wavelengths of 490/520 nm for FAM or 645/670 nm for Cy5. Read 1 measured autofluorescence in a reaction mixture containing buffer, NSP15, and compound. Subsequently, RNA substrate was added, and following incubation at 37°C in a humidified incubator for 20 minutes, the reaction was stopped by addition of 100 mM EDTA and Read 2 was performed. After the addition of 1 μM of positive control FAM-RNA (**Table 2.3**) to the reaction, Read 3 was taken to test for potential quenching. Percent inhibition values were calculated as follows: (Read 2 – Read 1)/Average Negative Control. Compounds that were found to quench the positive control by >50% in Read 3 were excluded from further analysis.

2.5 NSP15 RNA Gel Cleavage Assay and Densitometry

Native RNA cleavage assays employed a 31 nucleotide (nt) ssRNA (IDT, USA and Biosynthesis, USA) with the sequence 5'-rArUrArArArArArArArArA-3', whose cleavage at the "rU" site results in 21 nt and 10 nt fragments. The reaction was set up in a 10 μ L volume containing a final concentration of 7.5 ng/ μ l NSP15 and 250ng of RNA in assay buffer (25 mM HEPES, 50 mM NaCl, 5 mM MnCl₂, and 1 mM DTT) and allowed to run for the indicated time. Prior to gel loading, samples were prepared with 2X formamide-based RNA loading dye (NEB, Canada) and were boiled at 95°C for 5 minutes. Samples were electrophoresed on a denaturing 15% Mini-Protean TBE-UREA polyacrylamide gel (BioRad, USA) and run at 200 V for ~40 minutes at room temperature. Gels were stained with SYBR Gold (Thermo Fisher, Canada) for 20 minutes and imaged at Cy3 fluorescent channels (520/605 nm excitation/emission) with an Amersham Imager 680 (Cytiva, USA).

2.6 Amplex Red Assay

Redox reactivity of the lead compounds was assessed using the Amplex™ Red Hydrogen Peroxide/Peroxidase Assay Kit (Invitrogen, Canada), according to the manufacturer's instructions. Briefly, test compounds were diluted in assay buffer to a final concentration of 100 μ M in the presence of the indicated concentrations of DTT in 96 well plates. Hydrogen peroxide at a concentration of 10 μ M was used as a positive control. The reaction was started by addition of 0.2 U/mL horseradish peroxidase and 50 μ M final concentration of Amplex Red reagent. The reaction was incubated in the dark for 15 minutes at room temperature. Plates were read using a SpectraMax i3x spectrophotometer (Molecular Devices, USA) at excitation and emission wavelengths of 560 nm and 590 nm, respectively.

2.7 Vero Cell Culture and Toxicity Assay

Vero CCL81 cells were a kind gift from Dr. Tom C. Hobman (University of Alberta, Canada). Cells were maintained in Dulbecco's modified Eagles Medium (DMEM) High Glucose (Thermo Fischer, USA) supplemented with 10% fetal bovine serum (FBS), Canadian Origin (Sigma, Canada) and 1x Penicillin-Streptomycin-Glutamine (Thermo, Canada) in a 37°C humidified incubator with 5% CO₂.

Cells were seeded in 96-well plates (Greiner, USA) at 10,000 cells per well overnight before addition of compounds. Compounds were added to wells at the indicated concentrations alongside a DMSO control. Twenty-four hours later, cell viability was assayed using the CellTiter-Glo Luminescent Cell Viability Assay (Promega, USA) according to the manufacturer's instructions. Briefly, the assay relies on the quantification of adenosine 5'triphosphate (ATP) using a proprietary Ultra-Glo Luciferase that converts Luciferin to luminescent oxyluciferin in the presence of ATP. Cells were incubated in 100 µl of complete media with 100 µl of reconstituted CellTiter-Glo Reagent (buffer plus substrate). Samples were mixed by shaking for 10 minutes and then luminescence was measured using a Spectramax i3x (Molecular Devices, USA) device. Data from experimental wells was normalized to the appropriate DMSO control.

2.8 Vero SARS-CoV-2 Plaque Assay

Severe acute respiratory syndrome coronavirus 2 (SARS-CoV-2/CANADA/VIDO 01/2020) was kindly provided by Dr. Darryl Falzarano (Vaccine and Infectious Disease Organization-International Vaccine Centre, University of Saskatchewan, Canada). The virus was studied in a biosafety level 3 laboratory at the University of Alberta. The strain was grown in Vero cells (ATCC) with DMEM supplemented with 10% fetal bovine serum, 15 mM HEPES, L-glutamine and Penicillin-Streptomycin. To perform a plaque assay, Vero cells were infected for 24 hours with SARS-CoV-2 virus at a multiplicity of infection (m.o.i) of 0.1 in the absence or presence of compounds. Subsequently, supernatants were collected for virus titer determination by plaque assay. The monolayers were

overlaid with a mixture of MEM (Thermo Fisher, Canada) and 0.75% carboxymethylcellulose (Sigma-Aldrich) following infection. The cells were maintained at 37°C for 72 hours for plaque development. Cells were fixed with 10% formaldehyde and stained with 1% crystal violet in 20% ethanol after which time plaques were counted.

2.9 In-silico Pharmacological Predictors

Simplified Molecular Input Line Entry Specification (SMILES) were collected from PubChem Chemical Structure Sketcher), Open Parser for Systematic IUPAC Nomenclature (OPSIN), and/or PubChem literature search. Pharmacological predictors were obtained by inputting compound SMILES into ACD Labs Percepta Software (ACD Labs, Canada). Physical and chemical values collected were H-bond donor, H-bond acceptor, aromatic ring count, LogS, LogD, LogP, strongest pKa (Acid), strongest pKa (Base), Lipinski rule and overall solubility. The ADME parameters available for predictions were: P-gp substrate, CNS, PPB, Caco-2. The toxicological properties are Ames and hERG.

2.9 Data Analysis

GraphPad Prism 9 (GraphPad Software Inc, USA) was used for general plotting and statistics. High-throughput screening data was analyzed and graphed with Python or GraphPad Prism 9 (GraphPad Software Inc, USA). RNA cleavage gel densitometry was performed with ImageStudioLite 5.2.5 (LICOR, USA). Endnote 20 (Clarivate, USA) was used for reference organization. Chemical structures were generated with ChemDraw 21.0.0 (ChemAxon, USA).

CHAPTER 3: High-throughput (HTP) Screening to Identify SARS-CoV-2 NSP15 Inhibitors

3.1 NSP15 Reaction Setup and Substrate Optimization

3.1.1 NSP15 Reaction Setup

To identify NSP15 compound inhibitors, I adapted a fluorescence resonance energy transfer (FRET)-based NSP15 activity assay that was previously described⁶². Briefly, the assay relies on an RNA substrate flanked by a fluorophore-quencher pair. Fluorescent quenching is maintained via fluorescence resonance energy transfer (FRET) due to the close distance of the 5-prime fluorophores (FAM or Cy5) and 3-prime quenchers (BHQ1 or BHQ2). In the presence of manganese and reducing agent dithiothreitol (DTT), NSP15 would preferentially cleave the uracil residue of the reporter RNA. This cleavage produces fluorescence that would then be measured by a spectrophotometer (**Figure 3.1a**). This assay was adaptable to both 96-well 60 μ l reactions or 384-well 20 μ l reactions. The standard assay buffer contained 25 mM HEPES, 50 mM NaCl, 5 mM $MnCl_2$, and 1 mM dithiothreitol (DTT). To set up the assay, I first cloned and purified recombinant SARS-CoV-2 NSP15 (**Figure 3.1b**). To optimize the assay, three different 5'fluorescein (FAM) and 3'black hole quencher 1(BHQ1) RNA reporter substrates were tested, and whose sequences have been previously used for SARS-CoV-1 NSP15 assays (**Table 2.2**). The reporter RNA substrates were: RNA1: 5'FAM-rArArArArArArGrUrArArArArA-3'BHQ1, RNA2: 5'FAM-rCrArArCrUrArArArCrGrArArC-3'BHQ1, and RNA3: 5'FAM-dAdArUdAdA-3'BHQ1. FAM-only RNA control (5'FAM-rArArArArArArGrU) was included as positive control RNA. No uracil containing RNA (5'FAM-rArArArArArArGrArArArArArA-3'BHQ1) was included as negative control RNA.

All three reporter RNAs contained a single uridylate (rU) flanked by ribonucleic acids (RNA1,2) or deoxyribonucleic acid (RNA3). When incubated with NSP15, all three RNA substrates produced measurable signal compared to their respective background control

(RNA + buffer only), however, only RNA2 generated significant fluorescent signal against background control (**Figure 3.1c**). On the other hand, as expected, the negative control RNA did not result in significant fluorescent cleavage compared to its background control when incubated with NSP15 (**Figure 3.1c**). Based on its favourable fluorescence properties, the RNA2 sequence was used for all subsequent experiments.

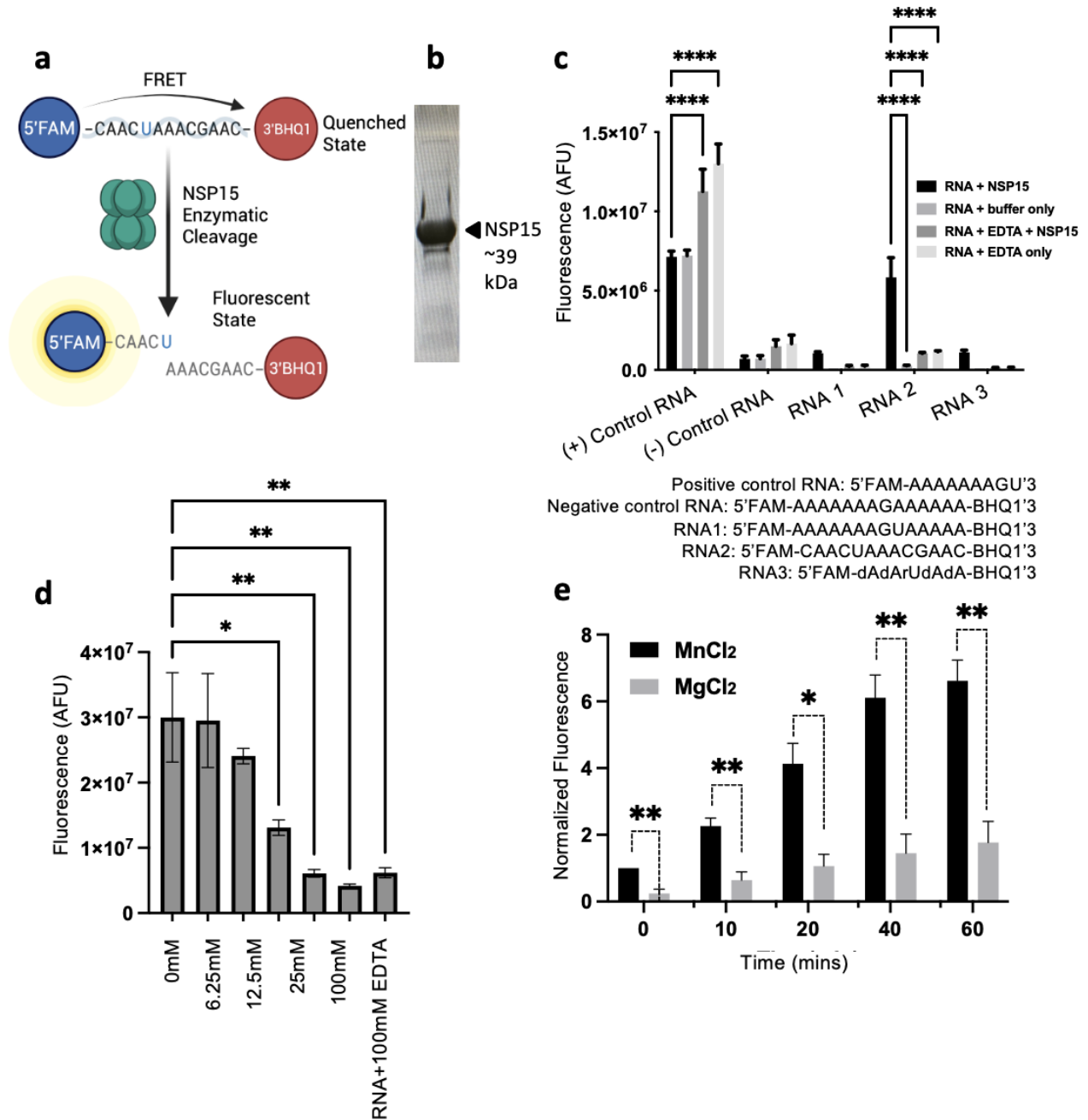


Figure 3.1. Establishment of FRET-based NSP15 activity assay. **a)** Schematic of NSP15 activity assay. Un-cleaved RNA substrate contained a 5'fluorescein (FAM) and 3'black hole quencher 1(BHQ1). In the presence of manganese and DTT, NSP15 cleaved RNA substrate at the uracil residue. **b)** Coomassie stain of purified recombinant wildtype NSP15 (~39kDa) following His-column purification. **c)** NSP15 activity assay tested with various reporter RNA constructs \pm 100 mM of EDTA. Negative control RNA (no uracil RNA) did not produce significant cleavage signal compared to background control (RNA+Buffer). RNA2 generated the highest fluorescent cleavage signal in contrast to RNA 1 and 2. Meanwhile, 100 mM EDTA inhibited reaction but significantly increased background signal regardless of NSP15 addition. Schematic of each RNA substrate sequences shown. Incubation occurred at 60 minutes. Stars indicate significance using two-way ANOVA with Dunnett's multiple comparisons test. **d)** EDTA (pH 8.0) titration on NSP15 activity. Starting at 25 mM of EDTA, activity was significantly reduced compared to no EDTA control. Complete inhibition of activity was achieved at 50-100 mM of EDTA. 1 μ M of RNA and 40 minutes of incubation time were used. Stars indicate significance using one way ANOVA with Dunnett's multiple comparisons test. **e)** Effect of 5 mM Mn^{2+} or Mg^{2+} on NSP15 activity. Mg^{2+} activity was significantly lower than activity with Mn^{2+} buffer. Data was normalized to time zero of manganese chloride. Stars indicate significance using multiple unpaired two-tailed Student's *t*-test. All results above were expressed as the mean \pm S.E, n=3, (* denotes $p < 0.05$) (**denotes $p < 0.01$) (***) denotes $p < 0.001$ ***), (**** denotes $p < 0.0001$).

3.1.2 NSP15 EDTA Inhibition and Ion Preference

Because NSP15s in other coronaviruses, such as SARS-CoV-1, have been reported to rely on manganese chloride (Mn^{2+}), but not magnesium chloride (Mg^{2+}) for activity, I investigated if SARS-CoV-2 NSP15 exhibited the same ion dependant preference.⁵⁸ SARS-CoV-2 NSP15 activity was significantly reduced in the presence of buffer containing only 5 mM Mg^{2+} versus 5mM Mn^{2+} (**Figure 3.1e**). This was in line with other reported results on SARS-CoV-2 NSP15, suggesting that SARS-CoV-2 NSP15 retains the preference for manganese^{58,9}.

Because NSP15 was dependent on manganese chloride (Mn^{2+}), I investigated if the addition of metal chelator ethylenediaminetetraacetic acid (EDTA; pH 8.0), a known Mn^{2+} chelator, would completely reduce the activity of the assay. Starting at 25 mM of EDTA, activity was significantly attenuated (**Figure 3.1d**). At 100 mM of EDTA, activity was completely reduced. (**Figure 3.1d**). Such attenuation of activity was effective for all RNA substrates sequences (**Figure 3.1c**). From this experiment, it was established that 100 mM EDTA can be used as a stopping reagent for the NSP15 activity assay.

3.1.3 NSP15 Mutant Analysis

To further validate the NSP15 assay, two NSP15 mutant protein constructs were purified using the same purification method (see **Chapter 2** for protocol). Based on previous literature, these included an H250A mutant (where the alanine replaced histidine at the 250 amino acid residue within the C-terminus catalytic domain), and a $\Delta 0-28 \Delta 336-347$ truncation mutant (containing truncations of both the N-term oligomerization domain and the C-terminus catalytic domain) (**Figure 3.2a**)^{40, 64}. The activity assay showed that all mutant proteins produced significantly reduced activity compared to wildtype NSP15 (**Figure 3.2b**). These results suggested that the signal of the assay is dependent on the catalytic activity of the NSP15 enzyme.

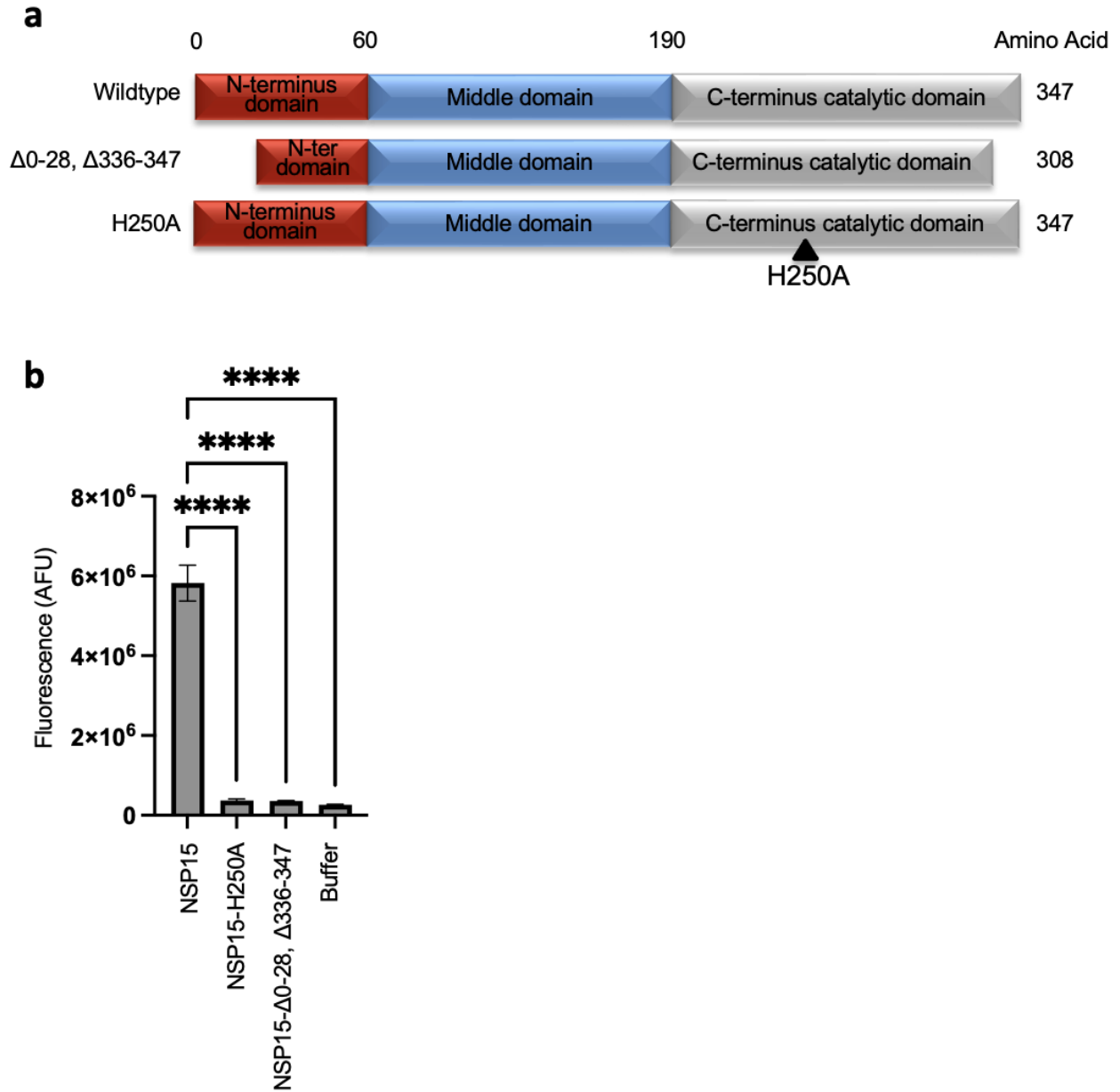


Figure 3.2. Inhibition of RNA cleavage activity by NSP15 mutants. A) Diagram of wildtype (WT) NSP15 and mutant NSP15 constructs. For the H250A mutant, alanine replaced histidine at the 250th amino acid residue within the C-terminus catalytic domain. For the $\Delta 0-28, \Delta 336-347$ truncation mutant, the first 28 amino acids of the N-terminus and last 11 amino acid of the C-terminus have been truncated. **B)** NSP15 mutants (H250A, and $\Delta 0-28, \Delta 336-347$) showed significantly decreased activity compared to wildtype (WT) NSP15 using the NSP15 activity assay. Stars indicate significance using one-way ANOVA with Dunnett's multiple comparison. Results were expressed as the mean \pm S.E, n=3, (**** denotes $p < 0.0001$).

3.1.4 Enzyme Kinetics

Following validation of the NSP15 activity assay, I characterized the enzyme kinetics of NSP15. To do this, reaction progress curves were performed at varying RNA substrate concentrations at early time points (1- 6 minutes) to produce linear reaction rate curves at a fixed NSP15 concentration (**Figure 3.3a**). To obtain product velocity, the fluorescent signal was first converted to RNA product using the equation $y(\text{fluorescence}) = 9011943 \cdot x(\text{product})$. This equation was calculated from a standard curve of the FAM only positive control RNA. The product amount was then divided by the amount of the reaction time elapsed to obtain rate. To obtain Michaelis-Menten curves, I plotted reaction velocity against increasing concentrations of RNA substrate at a fixed NSP15 concentration (1 ng/ μl). From three independent trials, I found that NSP15 has a mean K_M of $2.9 \pm 0.4 \mu\text{M}$ and V_{max} of $0.29 \pm 0.3 \mu\text{M}/\text{min}$ (**Figure 3.3b**). In comparison, SARS-CoV-1 had a reported K_M of $36.4 \pm 6.7 \mu\text{M}$ and the V_{max} of $0.15 \pm 0.03 \mu\text{M}/\text{min}$ ⁶². Based on the K_M value, RNA concentrations below $2.9 \mu\text{M}$ would be sufficient for future NSP15 screens in order to prevent excess competition with potential competitive inhibitors. Prior to the screen, NSP15 protein levels were optimized by varying the amount of NSP15 with a fixed amount of $0.5 \mu\text{M}$ RNA (**Figure 3.3c**). Based on the data, I decided that 1 ng/ μl of NSP15 for 20 minutes of reaction time was an acceptable experimental setup for the screen.

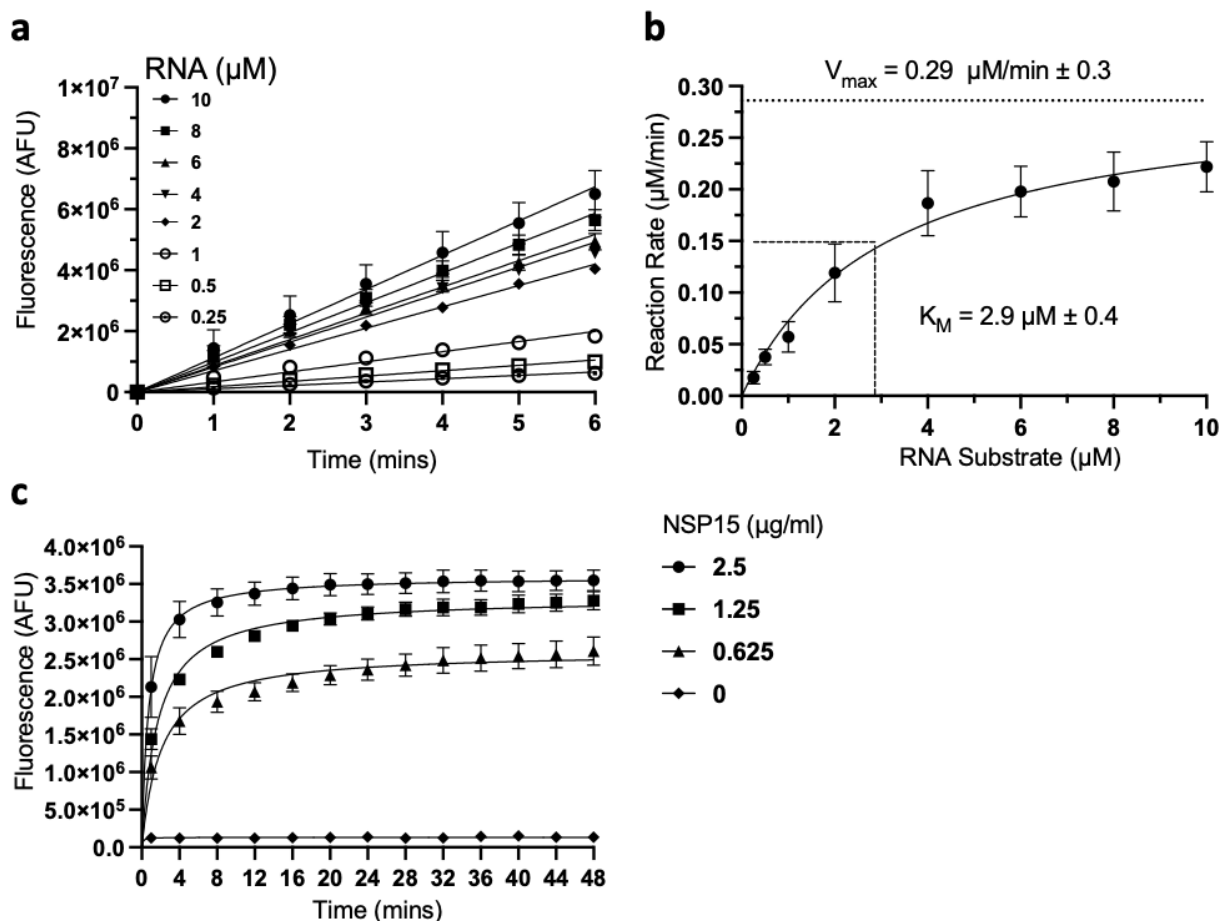


Figure 3.3. NSP15 enzyme kinetics. A) Initial NSP15 activity when incubated with various RNA substrate concentrations at fixed 1 ng/ μl ($\mu\text{g}/\text{ml}$) NSP15 concentration. Background (time 0) reading was subtracted from all data points. **B)** Michaelis-Menten plot of NSP15. NSP15 K_M was found to be $2.9 \pm 0.4 \mu\text{M}$ and V_{max} was found to be $0.29 \pm 0.3 \mu\text{M}/\text{min}$. Reaction rate was derived from the standard curve equation of $y(\text{fluorescence}) = 9011943 \cdot x(\text{product})$, divided by reaction time. **C)** Effect of varying concentrations of NSP15 activity over time with 1 μM of RNA. Results were expressed as the mean \pm S.E, $n=3$.

3.2 NSP15 High-throughput Screen of Small-Molecule Inhibitors

Using the above NSP15 assay, I performed a high-throughput screen of over 108,000+ compounds selected from the Maybridge, Prestwick, Microsource Spectrum, LOPAC, TimTec, and Chembridge DIVERSet collection compound libraries. Overlap between compounds libraries was $<0.1\%$.

In 384 well plates with 20 μ l reaction volume, the screen was set-up in three stages (see **Figure 3.4a** for a graphic summary of the stages). First, compounds were diluted in buffer with NSP15 and read at 480/520 nm excitation/emission to measure compound autofluorescence. Second, RNA substrate was added to each well to start the reaction. The final assay concentration was 1 ng/ μ l NSP15 with 0.5 μ M of RNA and 10 μ M of compound. The reaction proceeded for 20 minutes in a 37°C humidified incubator before 100 mM of EDTA was added as a stopping reagent. The plate was subsequently read to measure assay fluorescence. Thirdly, 0.5 μ M of positive control FAM RNA was added to each well to measure potential quenching effects. For each plate, positive control denotes the addition of DMSO, while negative control denotes no NSP15 added or 100 μ M of BenzopurpurinB added. BenzopurpurinB was a putative SARS-CoV-1 NSP15 inhibitor.⁸ Data was then processed with Python and/or PRISM, and was normalized as percent inhibition to the negative controls. Overall, the screen was robust, with an average signal/noise ratio >5 and with a Z' > 0.3. **Figure 3.4a** contain a summary of the screening process, and **Figure 3.4b** contain a graphic summary of the primary screen.

The results from the primary screen identified 1280 compounds whose fluorescence values were above two standard deviations from the mean. These compounds were then selected for secondary screening. I performed secondary screening with 5'Cy5 rCrArArCrUrArArArCrGrArArC-3'BHQ2 RNA in a similar fashion to the primary screen. However, the secondary screen did not include a third read with a positive control RNA. Reactions were incubated at 20 minutes at 37°C incubator and read at 645/670 nm. **Figure 3.4c** contain the graphic summary of the secondary screen.

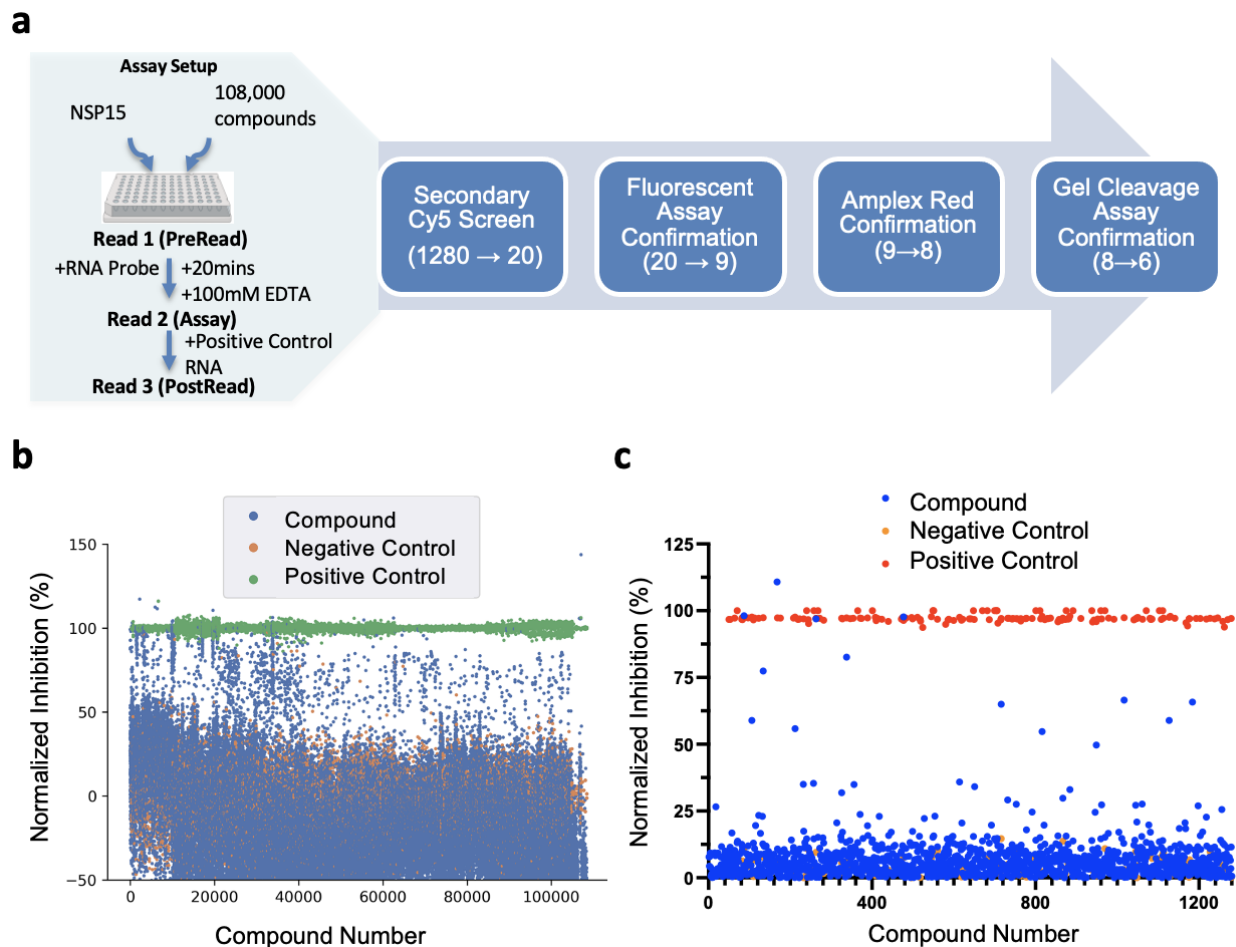


Figure 3.4. SARS-Cov-2 NSP15 high-throughput screening of small-molecule inhibitors. **a)** Schematic of high-throughput NSP15 screen and hit validation flowchart. Screening assay was set up such that there was a 1st pre-assay read for autofluorescence of compounds, a 2nd read for assay inhibition, and a 3rd post-assay read for extreme quenching effects. Hit molecules were then subjected to numerous downstream assays to validate and characterize their NSP15 inhibition activity. Parenthesis denoted the number of molecules that have successfully passed each of the assays. **B)** Graphic summarization of primary NSP15 screen with 108,000+ compounds. Signal was normalized to negative control as 100%. **C)** Graphic summarization of secondary NSP15 screen. Top 1280 compounds taken from two sigma deviations from the mean of the primary screen was selected for the secondary screen. The secondary screen was performed twice. Signal was normalized using negative control as 100%.

3.3 NSP15 Fluorescent and Quenching Assay Hit Validation

From the secondary screen, the top 20 compounds were selected for further validation. Compounds were rescreened at both FAM and Cy5 fluorescent channels at high doses of 25 μ M and 50 μ M. Because the FRET-assay was fluorescent dependent, we tested potential quenching effects using fluorescently tagged positive control RNAs: 5FAM'-CAACU'3 or 5Cy5'-CAACU'3 RNA (**Figure 3.5b**). This analysis showed that inhibition by compounds Asianticoside, CID9103877, CID5562635, CID3467652, CID19158832, CID81123829 were not reproducible, as shown in **Figure 3.5a,b**. Moreover, the initially observed inhibition of compounds, Fisetin, Doxycycline, CID97166731, CID3302573 were likely due to quenching, as shown in **Figure 3.5c,d**. However, 9 compounds (alongside the negative control BenzopurpurinB, a previously known NSP15 inhibitor) showed significant inhibition levels that were higher than their effect on quenching, in at least one or both channels. These compounds included CID4017446, CID5675221, Hexachlorophene, CID5220994, CID5266986, beta-lapachone, Reactive Blue 2 and IPA3. It should be noted that compounds were quenched more frequently in the Cy5 fluorophore than FAM fluorophore, suggesting that Cy5 could be more sensitive to quenching effects. As a result, the FAM substrate was used for subsequent FRET-based activity assays.

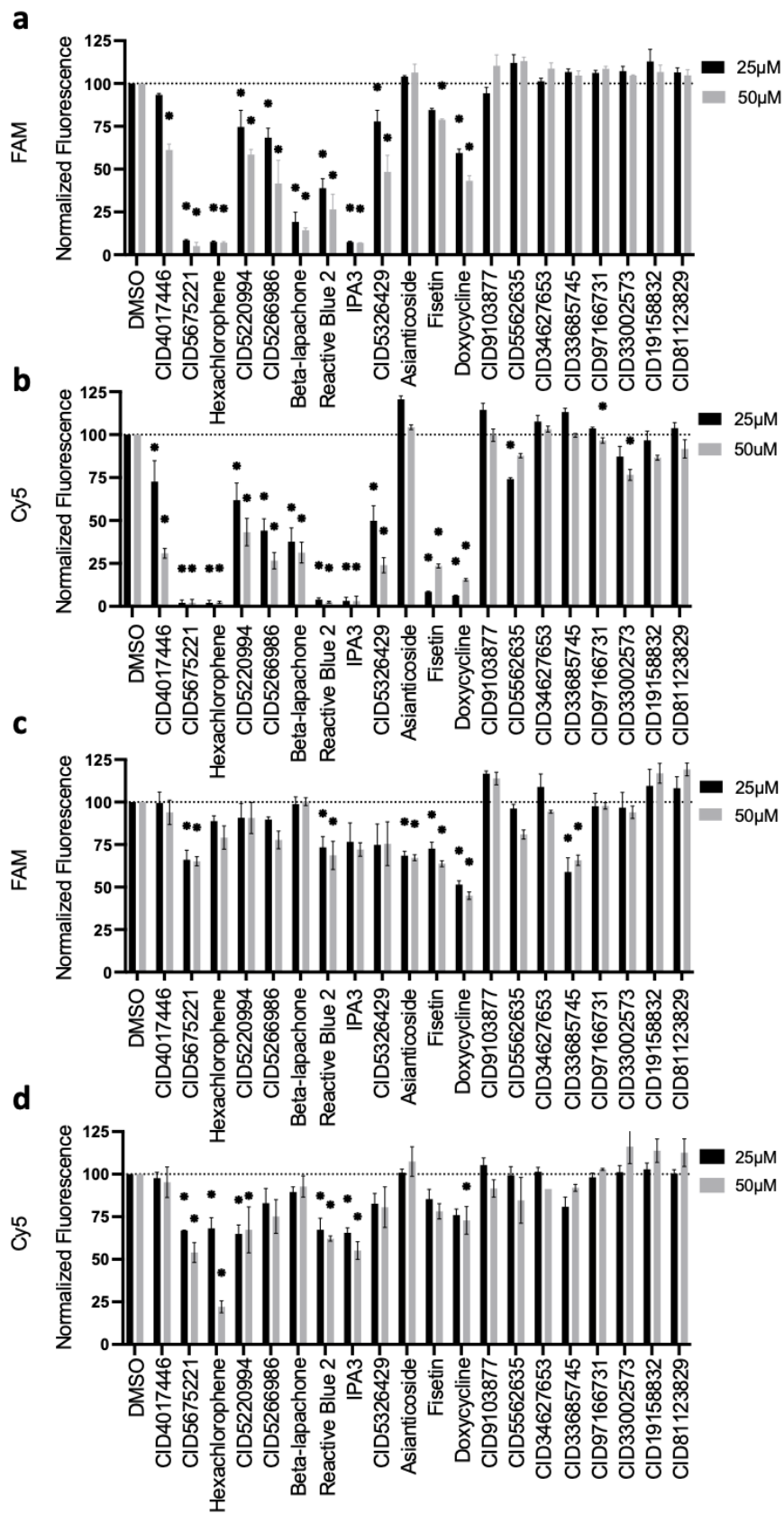
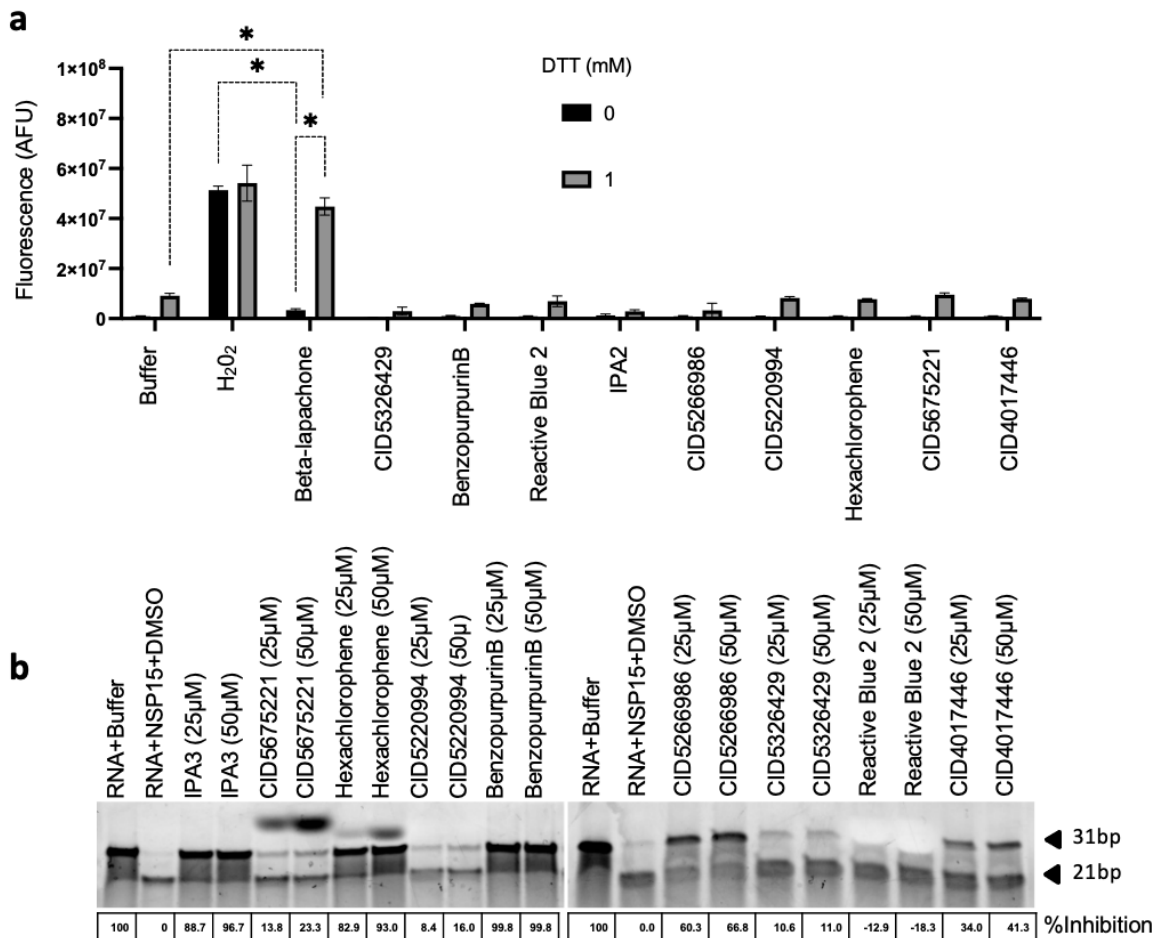


Figure 3.5. FRET-based assay validation of top twenty compound hits. Inhibition effect of compounds tested at 25 μ M and 50 μ M concentrations with: **a)** FAM RNA or **b)** Cy5 RNA. Results were normalized to DMSO (0.5%) control. Reaction setup was 1 ng/ μ l NSP15 incubated with 1 μ M of RNA. Quenching effects of compounds on positive control fluorescent RNAs **c)** FAM or **d)** Cy5 RNA were tested. Reaction setup was 25 μ M or 50 μ M of compounds added to 0.5 μ M of positive control FAM or Cy5 RNA. Stars denote significance compared to DMSO control using two-way ANOVA with Dunnett's multiple comparison. Results were expressed as the mean \pm S.E, n=3, (* denotes p<0.05).

3.4 NSP15 Inhibitors with Amplex Red Assay

Reducing agents, such as dithiothreitol (DTT), have the potential to participate in redox cycling in the presence of certain compounds and oxygen, resulting in H₂O₂ generation and non-specific inhibition of enzymes due to oxidative damage¹⁰⁶. Because our NSP15 assays included DTT, all nine lead compounds were tested at a high concentration of 100 μ M for any potential H₂O₂ generation using the Amplex Red assay. The assay principle relies on the Amplex Red reagent (10-acetyl-3,7-dihydroxyphenoxazine), whose oxidation in the presence of H₂O₂ and horseradish peroxidase, produced Resofurin in 1:1 ratio, a product that can imaged fluorescently at 560/590 nm excitation emission.¹⁰⁷ Amplex Red assay showed that only beta-lapachone produced significant non-specific redox cycling activities in the presence of 1 mM DTT when compared to buffer control (**Figure 3.6a**). Therefore, this compound was excluded from further assays. (See **Chapter 4** for more discussion on Amplex Red and DTT redox-cycling). Interestingly, a previous screen for NSP15 inhibitors also identified beta-lapachone as a possible inhibitor, and was ruled out based on its non-specific redox activity.¹⁰



c

CID 4017446	CID5220994	CID5266986	CID5675221	Hexachlorophene	IPA3	Benzopurpurin B (Control)
N-(1,3-thiazol-2-ylmethyl)cyclopropanamide dihydrochloride	N-(4-((9,10-dioxo-9,10-dihydro-2-anthracenyl)sulfonyl)aminophenyl)acetamide	3,4-dihydroxy-N'-(2-hydroxybenzylidene)benzohydrazide	3-benzyl-5-(3-bromo-2-hydroxy-5-nitrobenzylidene)-2-thioxo-1,3-thiazolidin-4-one	3,4,6-trichloro-2-[[2,3,5-trichloro-6-hydroxyphenyl)methyl]phenol	1-[(2-hydroxynaphthalen-1-yl)disulfanyl]naphthalen-2-ol	disodium;4-amino-3-[[4-[4-((1-amino-4-sulfonatophthalen-2-yl)diazonyl)-3-methylphenyl]-2-methylphenyl]diazonyl]naphthalene-1-sulfonate

Figure 3.6 Non-FRET-based validation of top NSP15 compound inhibitors. a) Only beta-lapachone significantly increased redox cycling compared to buffer control in the presence of 1mM dithiothreitol (DTT). Amplex Red assay was setup in the presence of 0 or 1 mM of DTT and 15 minutes of incubation. Reactions were read at 560nm excitation/590 nm emission. 10 μ M of H₂O₂ was added as a positive control for comparison. Stars denote significance using two-way ANOVA with Bonferroni's multiple comparison. Results were expressed as the mean \pm S.E, n=3, (p<0.05*). **B)** NSP15 non-FRET-based RNA cleavage gel assay with compounds tested at 25 and 50 μ M concentrations. Representative gel and densitometry (as percent inhibition compared to RNA+Buffer) are shown. 7 ng/ μ l of NSP15 was added to 250 ng of non-fluorescent cleavage gel RNA, which contained a single uracil (rU) flanked by poly(rA) nucleotides. The reaction was incubated for one hour at 37°C, ran on – 15% denaturing gel and stained with SYBR gold to visualize the bands. Cleavage of the 31nt RNA resulted in a visible 21 nt product. DMSO concentrations were kept at 0.5%. **c)** Structures of compounds that showed activity in the gel cleavage assay. CID denotes Chembridge-ID, purchased from Chembridge (USA).

3.5 NSP15 RNA Gel Cleavage Assay

To evaluate the ability of the compounds to inhibit NSP15 activity towards a native RNA substrate, I performed a cleavage assay using a natural non-fluorogenic RNA and analyzed the results using polyacrylamide gel electrophoresis. Briefly, this assay employed a 31 nt poly(rA) RNA punctuated with a single (rU), such that upon cleavage, it yielded a visible 21 nt product. For such a reaction, 7 ng/ μ l of NSP15 was added to 250 ng of RNA substrate and was incubated at 37°C for one hour. Reaction products were separated on a 15% polyacrylamide TBE-UREA denaturing gel. After SYBR-GOLD staining, uncleaved RNA substrate appeared as the top 31 nt band, while the cleaved RNA substrate appeared at 21 nt. The remaining 10 nt product was unable to be visualized. BenzopurpurinB was used as a positive control. Six of the eight prospective compounds demonstrated convincing inhibitory activity in this assay (**Figure 3.6b**). Unfortunately, Reactive Blue 2 could not be imaged as the compound produced an artifact that obscured the RNA band and thus was deprioritized. Compound CID5326429, which did not show appreciable inhibition, and was also excluded. **Figure 3.6c** shows the structures of the six compounds that passed the assay, plus the negative control BenzopurpurinB compound.

3.6 NSP15 Compound Inhibitors and IC₅₀ curves

Next, IC₅₀ titration curves were performed using both the above FRET-based NSP15 activity assay and gel cleavage assay. In both assays, compounds were diluted in a serial fashion before being added to the reaction. Using the FRET-based NSP15 activity assay (**Figure 3.7 and Table 3.1**), 3 compounds produced sub-20 μM IC₅₀ values. These were CID5675221, with a mean IC₅₀ of $12 \pm 1.2 \mu\text{M}$, IPA3 with a mean IC₅₀ of $9.8 \pm 0.35 \mu\text{M}$ and Hexachlorophene with a mean IC₅₀ of $1.5 \pm 0.072 \mu\text{M}$. Three other compounds produced IC₅₀s in the 30-90 μM range. These were: CID5266986 with a mean IC₅₀ of $87 \pm 4.2 \mu\text{M}$, CID4017446 with mean IC₅₀ of $39 \pm 2.9 \mu\text{M}$ and CID5220994 with mean IC₅₀ of $54 \pm 2.2 \mu\text{M}$.

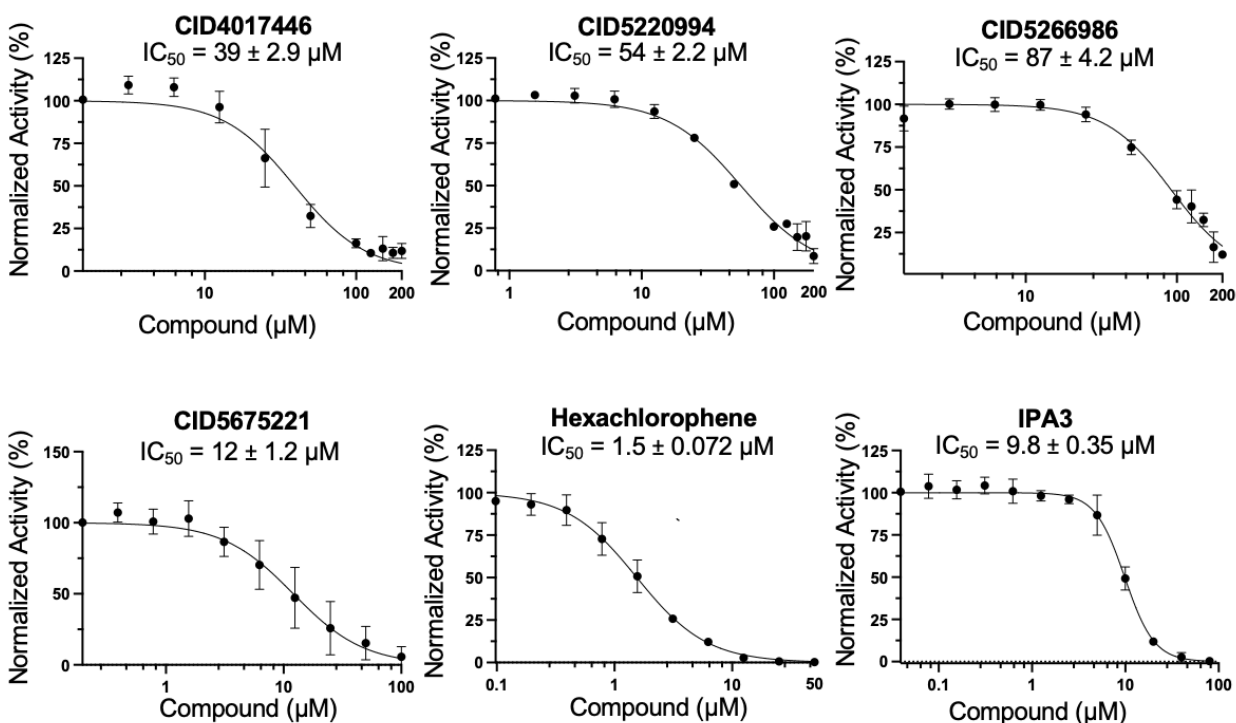


Figure 3.7. IC₅₀ of compound inhibitors using FRET-based assay. NSP15 (1ng/ μl) was incubated with a serial dilution of compounds and with fluorescent RNA2 substrate at 37°C for 12 minutes. Results were expressed as the mean \pm S.E, n=3. [Inhibitor] vs normalized response with variable slope curve was fitted to data. See Table 3.1 for summary of IC₅₀ values and hill slope values.

Due to the possible effect of fluorophore quenching by the compounds, I repeated the IC_{50} titration experiments using the gel cleavage assay. Inhibition activity was quantified using densitometry of the un-cleaved (31nt) product normalized to the negative (no NSP15) control. Using the gel-based assay, most compounds produced similar trends in inhibition compared to their FRET-based IC_{50} counterpart. These include: compound CID4017446 with a gel-based assay IC_{50} mean of $64 \pm 3.5 \mu\text{M}$, compound CID5220994 with IC_{50} of $95 \pm 3.2 \mu\text{M}$, compound CID5266986 with IC_{50} of $53 \pm 3.0 \mu\text{M}$, Hexachlorophene with a mean IC_{50} of $6.3 \pm 0.6 \mu\text{M}$, and IPA3 with IC_{50} of $4.8 \pm 0.6 \mu\text{M}$ (**Figure 3.8, and Table 3.1**). One exception was compound CID5675221, whose gel-based IC_{50} was $61 \pm 4.6 \mu\text{M}$, and was approximately 5x larger than its FRET-based IC_{50} of $12 \pm 1.2 \mu\text{M}$ (**Figure 3.7-3.8 and Table 3.1**). One explanation would be that compound CID5675221 produced quenching effects in the FAM channel (**Figure 3.6b**), which could have contributed to the stronger FRET-based IC_{50} value. In addition, stronger inhibition in FRET based assay IC_{50} s compared to its gel-based counterpart IC_{50} have been observed for previous NSP15 compound validations¹⁰. Nevertheless, all six inhibitors I identified showed NSP15 inhibition in a dose-dependent manner in both gel-based and FRET-based assays.

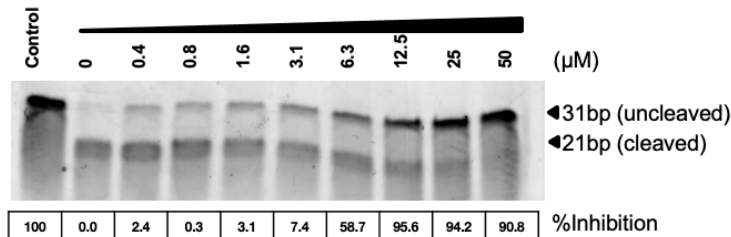
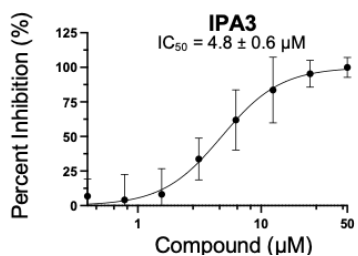
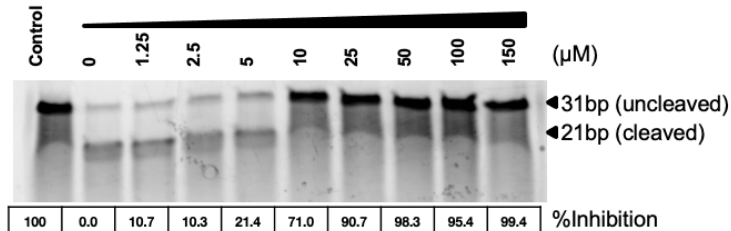
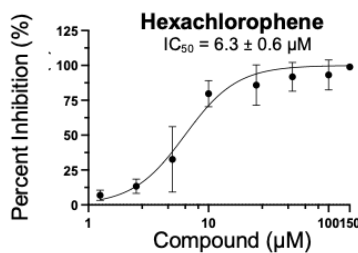
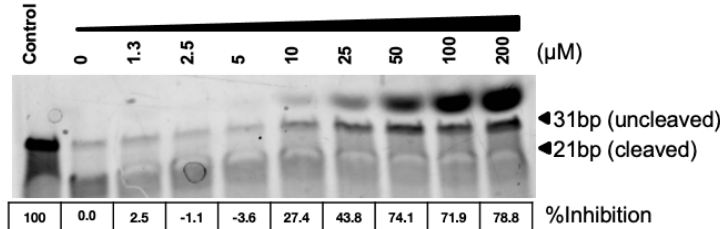
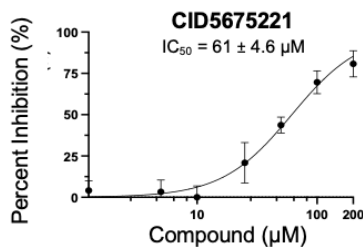
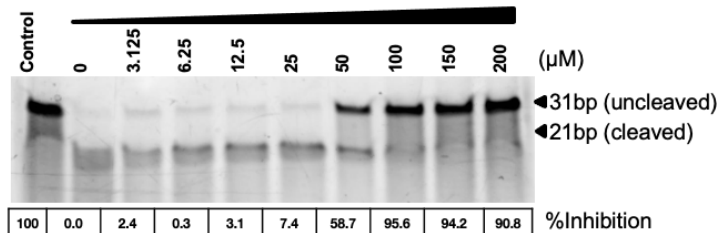
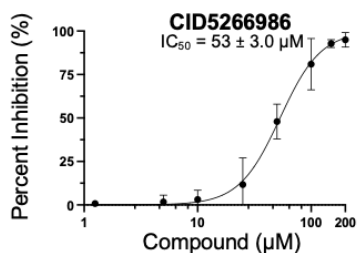
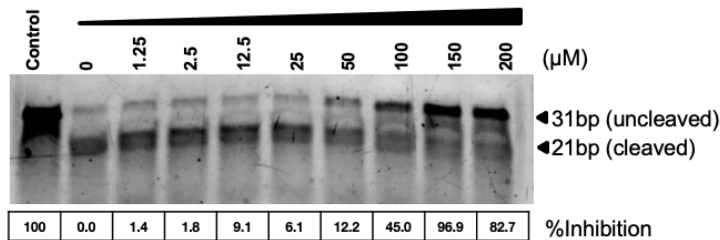
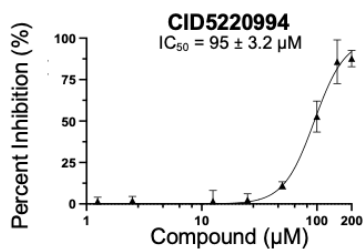
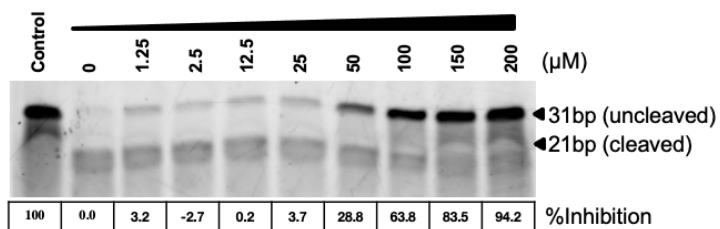
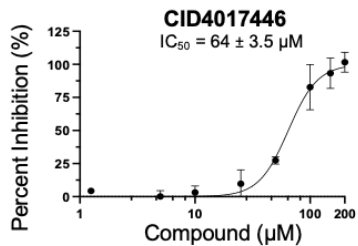


Figure 3.8: IC₅₀ of compound inhibitors using gel cleavage assay. NSP15 (7 ng/μl) was incubated with serial dilution of compounds and incubated with the 31 bp non-fluorescent single uracil-containing RNA substrate for 1 hour at 37°C. RNA cleavage was observed on 15% TBE-urea polyacrylamide gel stained with SYBR Gold. 100% denotes complete inhibition. Control denotes no NSP15 added. Densitometry of inhibition was calculated through the signal of full-length un-cleaved (31 nt) band, minus the “0” μM DMSO control band, and normalized to the negative control signal. Representative gel, and densitometry as percent inhibition, were shown. Results were expressed as the mean ± S.E, n=3. [Inhibitor] vs normalized response with variable slope curve was fitted to data. See **Table 3.1** for summary of IC₅₀ values and hill slope values. RNA sequence used was:

“5'rA-‘3,”.

Table 3.1: Summary of IC₅₀ values from both gel-based and FRET-based assays and their Hill slope values. Results expressed as the mean ± S.E, n=3.

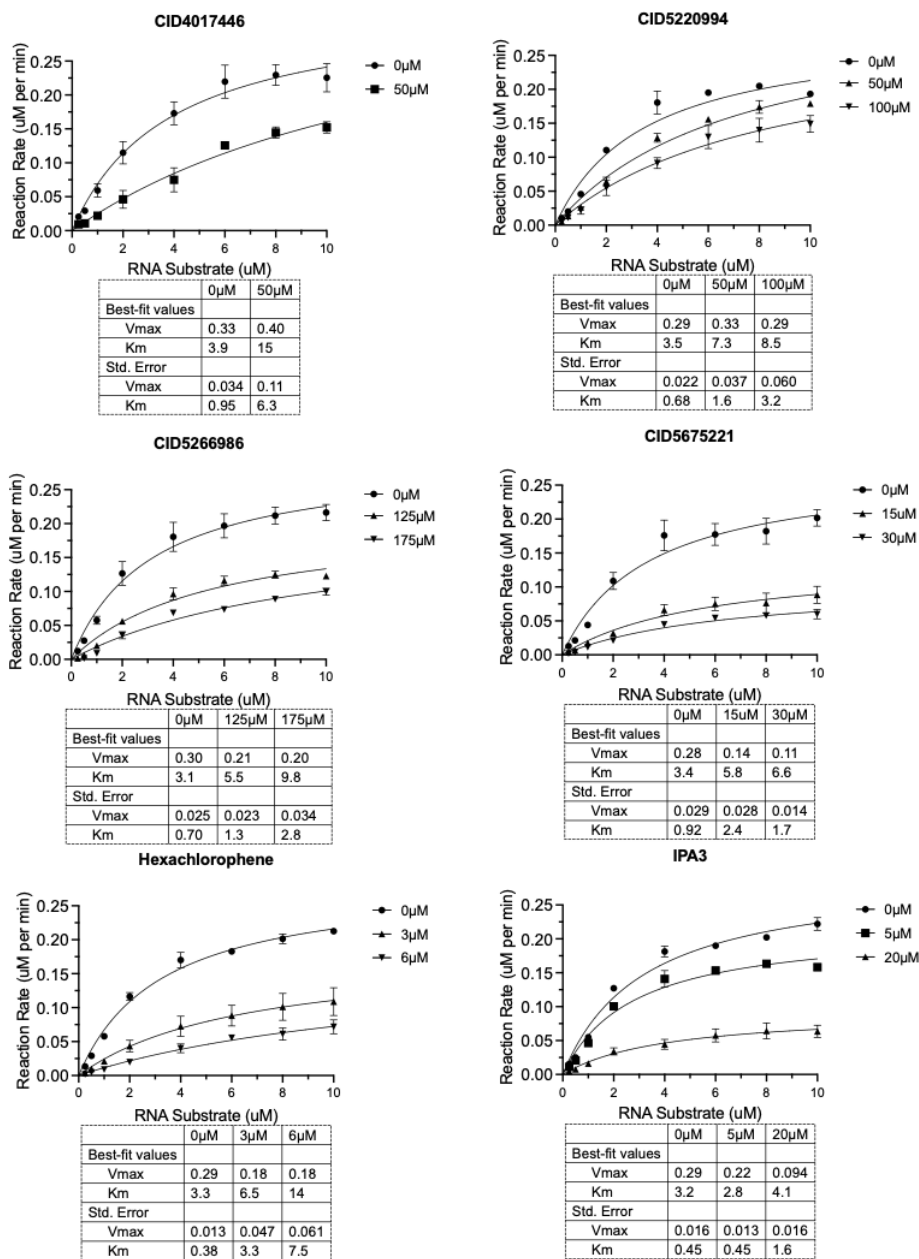
Compound Name	Mean IC ₅₀ (μM) ± S.E from Gel- based Assay	Gel Based Assay Hill Slope	Mean IC ₅₀ (μM) ± S.E from FRET-based Assay	FRET-Based Assay Hill Slope
CID4017446	64 ± 3.5	3.4 ± 0.5	39 ± 2.9	-1.8 ± 0.2
CID5220994	95 ± 3.2	3.2 ± 0.3	54 ± 2.2	-1.6 ± 0.08
CID5266986	53 ± 3.0	2.4 ± 1.7	87 ± 4.2	-2.0 ± 0.2
CID5675221	61 ± 4.6	1.8 ± 0.2	12 ± 1.2	-1.4 ± 0.2
Hexachlorophene	6.3 ± 0.6	2.0 ± 0.4	1.5 ± 0.072	-1.5 ± 0.08
IPA3	4.8 ± 0.6	1.8 ± 0.7	9.8 ± 0.35	-2.7 ± 0.3

3.7 NSP15 Michaelis-Menten of Compound Inhibitors

Next, to begin investigation into the mechanism of the 6 lead compounds, Michaelis-Menten titrations of increasing doses of the FAM-BHQ1 RNA substrates in the presence

or absence of the inhibitor compounds were performed. The resulting curves are shown in **Figure 3.9a** and the corresponding mechanisms of inhibition are summarized in **Table 3.2**. Briefly, CID4017446 and CID5220994 produced significantly higher K_m values but not affect V_{max} . As a result, they were classified as competitive inhibitors (**Table 3.2**). In contrast, CID5675221, Hexachlorophene and CID5266986 produced significantly higher K_m and lower V_{max} values, and thus was classified as mixed inhibition (**Table 3.2**). On the other hand, IPA3 produced significantly lowered V_{max} but not K_m values, and thus was classified as non-competitive (**Table 3.2**). To ensure that fluorescence quenching was not altering the interpretation of the results, a quenching assay was performed with the highest dose of inhibitor and found no significant quenching (**Figure 3.9b**).

a



b

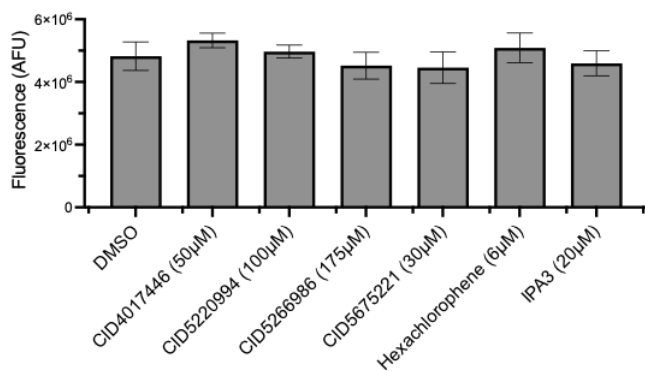


Figure 3.9. NSP15 Michaelis-Menten curves in the presence or absence of compound inhibitors. **a)** NSP15 (1 ng/ μ l) was incubated with serial dilution of fluorescent 5'FAM–BHQ1'3 RNA substrate at 37°C for 6 minutes. Compound concentrations were chosen to give partial inhibition and to avoid quenching effects. **b)** No significant quenching effects of NSP15 compounds were seen when incubated with 4 μ M of FAM positive control RNA at their respective dosages. Results were expressed as the mean \pm S.E, n=3. No significance was found when comparing compounds against DMSO control using one-way ANOVA with Dunnett's multiple comparison test.

Table 3.2: Summary of Michaelis-Menten values for compound inhibitors. Results were expressed as the mean \pm S.E, n=3. A difference in K_m and V_{max} was determined via extra sum-of-squares F test against average DMSO values taken from 15 trials, which was determined to have a K_m of 3.2 μ M \pm 0.20 and V_{max} of 0.30 μ M/min \pm 0.007.

Compound	Compound K_m (μ M) \pm S.E	Compound V_{max} (μ M/min) \pm S.E	K_m difference	K_m Statistics F=(DFn, DFd)	V_{max} difference	V_{max} Statistics F=(DFn, DFd)	Predicted Type of inhibition
CID4017446 (50 μ M)	15 \pm 6.3	0.40 \pm 0.11	Yes	P<0.0001 F 26.60 (1, 22)	No	P=0.2315 F=1.514 (1, 22)	Competitive
CID5220994 (100 μ M)	8.5 \pm 3.2	0.29 \pm 0.060	Yes	P<0.0001 25.93 (1, 22)	No	P=0.4587 F=0.5689 (1, 22)	Competitive
CID5266986 (175 μ M)	9.8 \pm 2.8	0.20 \pm 0.034	Yes	P<0.0001 23.69 (1, 22)	Yes	P=0.0397 4.782 (1, 22)	Mixed
CID5675221 (30 μ M)	6.6 \pm 1.7	0.11 \pm 0.014	Yes	P=0.0004 F=17.28 (1, 22)	Yes	P<0.0001 F 79.16 (1, 22)	Mixed
Hexachlorophene (6 μ M)	14 \pm 7.5	0.18 \pm 0.061	Yes	P<0.0001 F=65.12 (1, 22)	Yes	P=0.0280 F=5.537 (1, 22)	Mixed
IPA3 (20 μ M)	4.1 \pm 1.6	0.094 \pm 0.016	No	P=0.9059 F=0.01431 (1, 22)	Yes	P=0.0003 F= 18.01 (1, 22)	Non-competitive

3.8 NSP15 Compound Cytotoxicity Concentration 50 (CC_{50}) in Vero cells

To begin to evaluate the therapeutic potential of the inhibitors in suppressing SARS-CoV-2 replication, I tested their toxicity in Vero cells. Vero cells are kidney derived cells

from African Green Monkey and are commonly used in virology, including vaccine development, due to their susceptibility to viral infections¹⁰⁸. They have previously been used in a variety of SARS-CoV-2 studies for this reason^{9, 10, 109}. I tested a range of doses from 0.2 μM to 400 μM depending on the compound. I was unable to test doses higher than 400 μM , due to solubility limitations of these compounds, as well as the physiological relevance of higher doses. Using this assay, cell cytotoxicity 50 (CC_{50}) values were determined. These were: CID5220994 ($41 \pm 5.2 \mu\text{M}$), CID526698 ($42 \pm 4.8 \mu\text{M}$), CID5675221 ($248 \pm 33 \mu\text{M}$), Hexachlorophene ($15 \pm 4.6 \mu\text{M}$), and IPA3 ($38 \pm 3.9 \mu\text{M}$) (**Fig 3.10**). Compound CID4017446 did not produce a CC_{50} value because only limited cytotoxicity was observed, even at the highest dose tested of 400 μM (**Fig 3.10**).

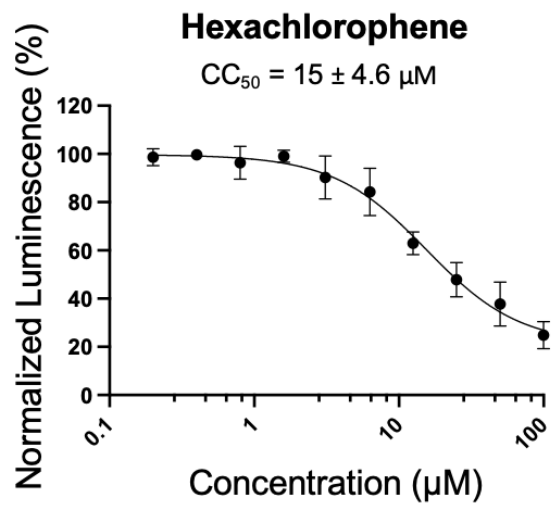
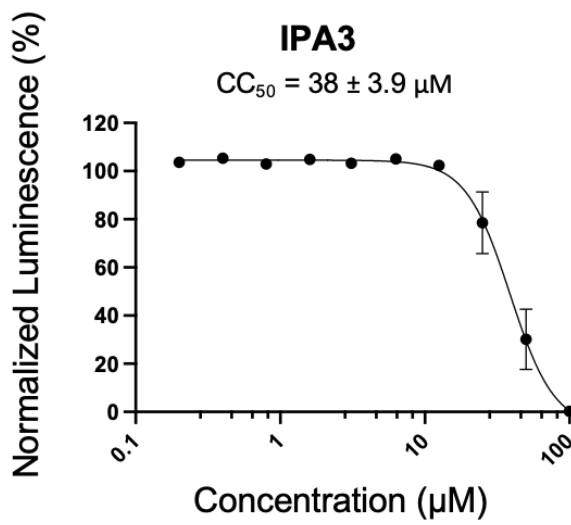
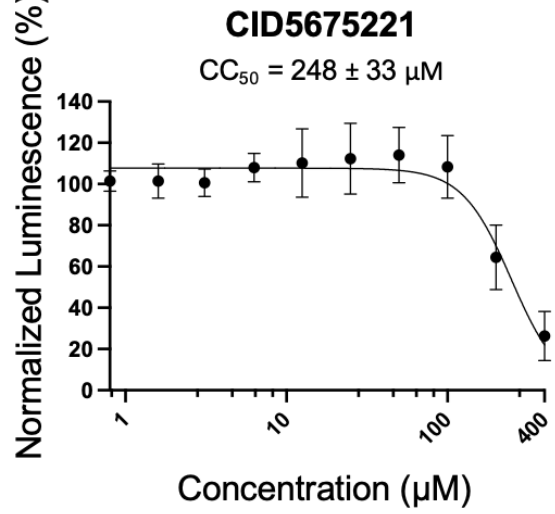
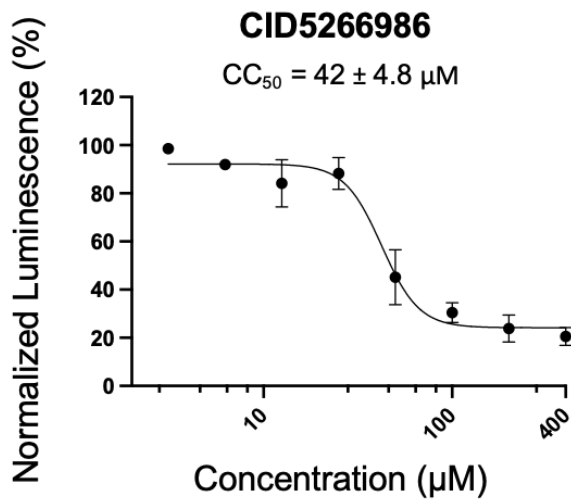
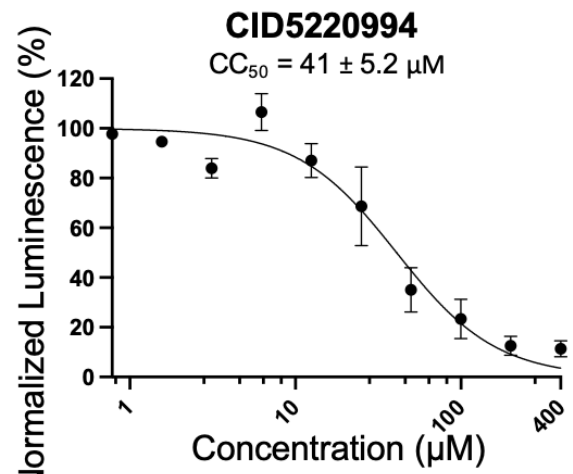
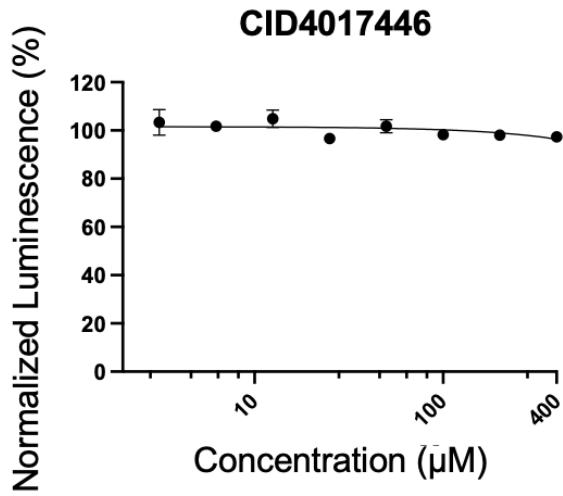


Figure 3.10. CC₅₀ Cytotoxicity Curves of NSP15 inhibitors in Vero cells. Viability of Vero cells incubated 24h with a titration of compounds (up to 400 µM) and assayed with CellTiterGlo viability assay. Results were normalized to no compound and DMSO *only* control. Results were expressed as the mean ± S.E, n=3. [Inhibitor] vs response with variable slope curve was fitted to data. See **Table 3.3** for summary of CC₅₀ values.

3.9 Compound Inhibitory Concentration 50 (IC₅₀) and Calculation of Therapeutic Index 50 (TI₅₀) in Vero cells

Having established compound toxicity, compounds were then tested for efficacy in inhibiting SARS-CoV-2 viral replication. These experiments were carried out in collaboration with Daniel Limonta Velázquez in lab of Dr. Tom Hobman at the University of Alberta. Compounds were first tested with a single dosage that was sub-toxic, and below CC₅₀ values. Vero cells were incubated with SARS-CoV-2 virus at 0.1 multiplicity of infection (m.o.i), with or without the presence of compounds. At 24 hours post infection (h.p.i) SARS-CoV-2 viral titers were measured using plaque assay. From the single dose assay, only CID5675221, Hexachlorophene, and IPA3 produced inhibitions at or above 50% effectiveness (**Figure 3.11a**). These three compounds were chosen for further dosage titration. Subsequently, CID5675221 produced an IC₅₀ of 19 ± 2.3 µM, Hexachlorophene produced an IC₅₀ of 0.95 ± 0.016 µM, and IPA3 produced an IC₅₀ of 7.9 ± 0.89 µM (**Figure 3.11b**).

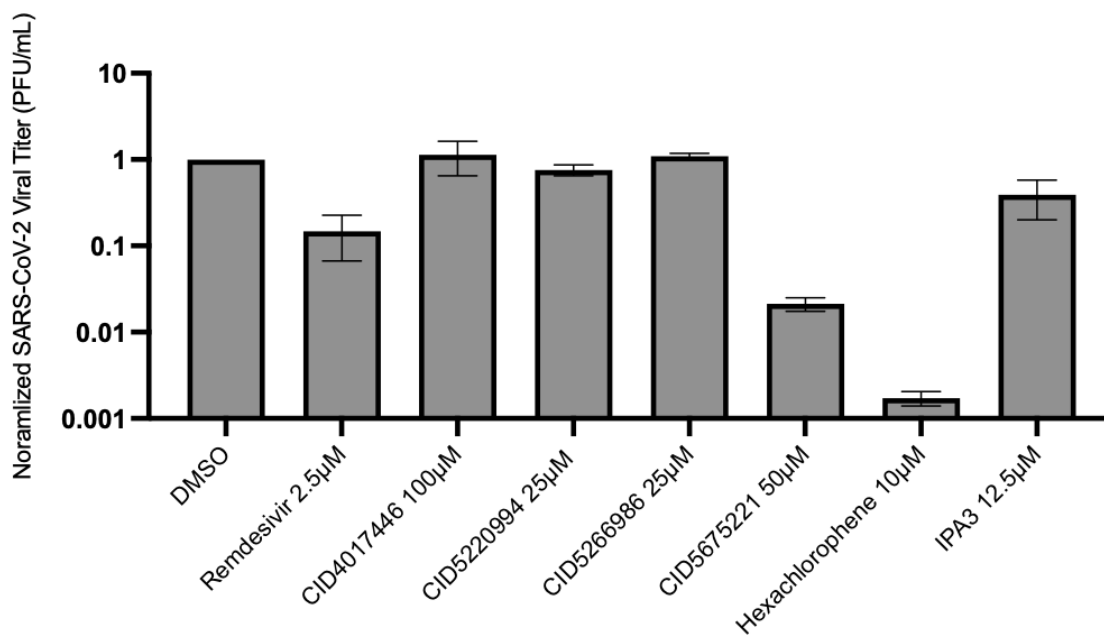
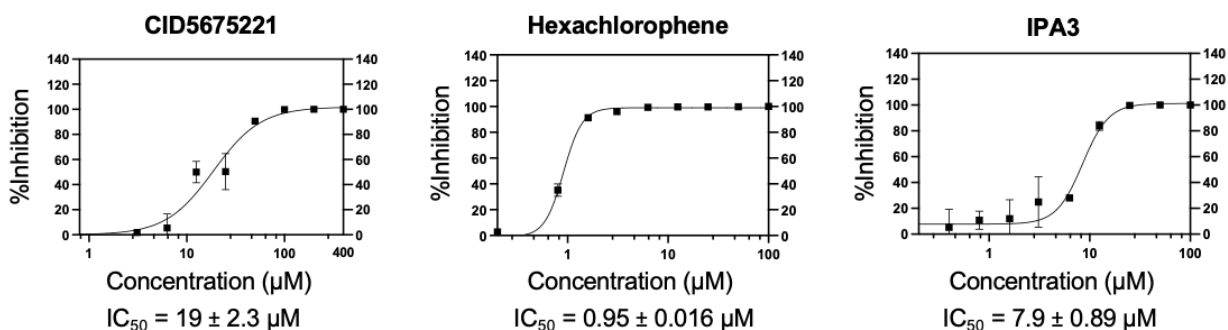
a**b**

Figure 3.11. Effectiveness of compounds on viral replication in Vero cells. Testing of compound effectiveness in reducing SARS-CoV-2 titers in Vero cells 24 h.p.i at: **a)** a single sub-toxic dose, or **b)** a dosage titration for the top 3 compounds. Viral titer was quantified by a plaque-forming unit (PFU) assay at 0.1 multiplicity of infection (m.o.i). Inhibition (%) was calculated as the percent of one minus the fraction of compound viral titer divided by non-viral DMSO control titer. Results were expressed as the mean ± S.E, n=2. A sigmoidal curve was fitted to data where applicable. See Table 3.3 for summary of IC₅₀ values.

To assess the selectivity index 50 (SI₅₀) of the top 3 lead compounds, cytotoxicity concentration 50 (CC₅₀) of each compound was divided by its inhibitory dose 50 (IC₅₀). All three compounds produced positive selectivity index dose 50 (SI₅₀) ratios.

CID5675221 produced an TC₅₀ of 15 ± 3.9, Hexachlorophene produced a TC₅₀ of 16 ± 4.7, IPA3 had an TC₅₀ of 5.4 ± 1.2.

Table 3.3: Summary of Cytotoxicity Concentration 50 (CC₅₀), Inhibitory Dose 50 (IC₅₀), and Selectivity Index 50 (SI₅₀) of NSP15 compound inhibitors in Vero cells against SARS-CoV-2. Results were expressed as the mean ± S.E, n=3 for CC₅₀ or n=2 for IC₅₀. SI₅₀ was calculated as CC₅₀ / IC₅₀. If values could not be calculated from the curves in Figure 3.10 and 3.11, they would be displayed as not available (N/A).

Compound	CC ₅₀ (μ M)	CC ₅₀ S.E	IC ₅₀ (μ M)	IC ₅₀ S.E	SI ₅₀	SI ₅₀ S.E
CID4017446	>400	N/A	N/A	N/A	N/A	N/A
CID5220994	41	5.2	N/A	N/A	N/A	N/A
CID5266986	42	4.8	N/A	N/A	N/A	N/A
CID5675221	248	33	19	2.3	15	3.8
Hexachlorophene	15	4.5	0.95	0.016	16	4.7
IPA3	38	3.9	7.9	0.89	5.4	1.2

3.10 Effect of DTT on NSP15 Activity and IPA3 Inhibition.

Because the molecular structure of IPA3 contained disulfide bonds, dithiothreitol (DTT) present in the assay buffer may have affected IPA3 inhibition activity (such as by cleaving the molecule into two). To test this hypothesis, I first tested if NSP15 required DTT for optimum performance in the FRET-based NSP15 assay. The results showed that NSP15 had drastically lowered activity without DTT in the buffer (**Figure 3.12**). At the same time, DTT concentrations above 1 mM did not result in significant increases in activity (**Figure 3.12**). Based on the results, DTT concentrations at 1 mM was determined to be sufficiently suitable for FRET-based assays. At the same time, IPA3 showed significant inhibition of NSP15 activity at both 0 and 1 mM DTT containing assays. However, at 10 mM DTT, IPA3 inhibition activity was insignificant versus “no

IPA3” control (Figure 3.12). The result suggested that DTT was detrimental to IPA3 inhibition NSP15 activity.

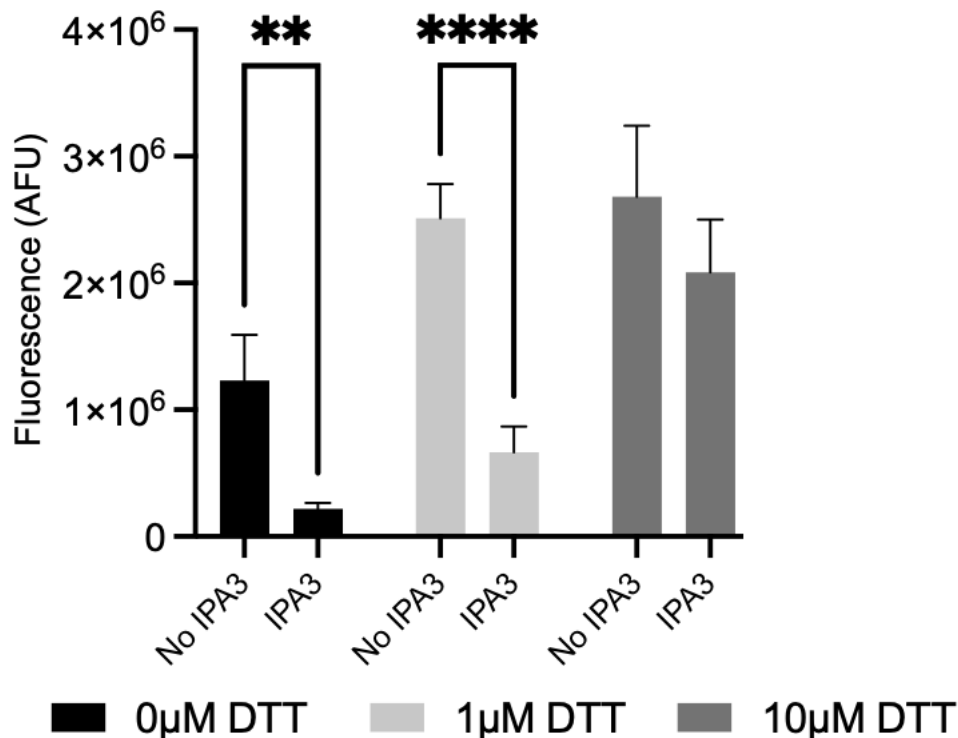


Figure 3.12 NSP15 and IPA3 activity was found to be dependent on dithiothreitol (DTT) concentration. NSP15 was incubated with different concentrations of DTT and 0.5µM of RNA2 ± 25µM IPA3. Results were expressed as the mean ± S.E, n=3. Stars indicate significance using two-way ANOVA with Bonferroni’s multiple comparison (* denotes p<0.05) (** denotes p< 0.01) (***) denotes p< 0.001), (****denotes p<0.0001).

3.11 Predicted Therapeutic Profile and Properties of NSP15 compounds

To further assess the therapeutic potential of the compounds, *in-silico* analysis of a variety of predictors were performed for the NSP15 inhibitors using ACD/Labs Percepta Software platform. The predictors included analysis of the Lipinski’s rule of 5, a predictor for overall “drugability” of a compound. The rule states that compounds should have:

- 1) No more than 5 H-bond donors¹¹⁰.

2) No more than 10 H-bond acceptors (excessive hydrogen bond donors/acceptors are known to impair permeability across membrane bi-layers)¹¹⁰.

3) Molecular weight <500 daltons (higher molecular weight are known to impair cellular permeability, including CNS and intestinal permeability)¹¹⁰.

4) Lipophilicity (LogP) <5 (LogP measures affinity for lipid environment; high lipophilicity is known to lead to poor solubility, low absorption and impairment of metabolic clearance leading to toxicity)¹¹⁰.

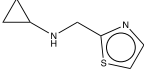
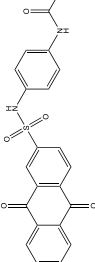
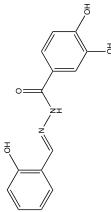
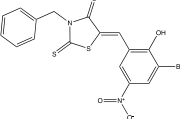
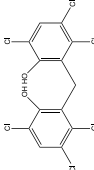
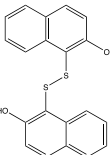
Other predictors tested include:

- Caco-2 permeability (predicts compound permeability to intestinal Caco-2 cells, a predictor of intestinal drug absorption)¹¹¹.
- P-glycoprotein (P-gp) substrates (predicts compound ability to bind to P-gp, an efflux transporter)¹¹².
- Ames bacterial test (predictor of carcinogenicity)¹¹³.
- hERG (Human ether-à-go-go related gene) (hERG is an ion channel and its binding is known to cause serious cardiotoxicity)¹¹⁴.
- CNS (central nervous system) penetration.
- Plasma protein binding (PPB) (high PPB affects drug diffusion, bioavailability and half-life of the compound)¹¹⁵.

I found that all compounds followed the Lipinski's rule except for Hexachlorophene, who only moderately followed the rule (**Table 3.4**). For Hexachlorophene, LogP was predicted to be 7.5, which was higher than the recommended value of 5 (**Table 3.4**). However, the compound obeyed all the other rules. At the same time, all compounds were predicted to be permeable to Caco-2 (**Table 3.4**). Meanwhile, the software predicted that only Hexachlorophene and CID5266986 were non-substrates to P-glycoprotein binding; the software was unable to form a prediction for the other compounds (**Table 3.4**). The software was also unable to predict AMEs test for most compounds, but Hexachlorophene was predicted to be non-mutagenic (**Table 3.4**). The software

predicted CID4017446, CID5220994 and CID5266986, were non-hERG substrates, while the others were undefined (**Table 3.4**). The software predicted CID4017446 and CID526698 as CNS penetrant while the other was not (**Table 3.4**). The compound also predicted CID5220994, and Hexachlorophene as extensively bound to plasma protein binding (PPB), CID526696 as a strong PPB binder, and CID4017446 as a weak PPB binder. Overall, these compounds have been predicted to have favorable properties for therapeutic treatment.

Table 3.4: Predicted Lipinski's rule of the five analyses and properties for NSP15 compound inhibitors. Values were predicted from Percepta Platform, ACD/Labs software (USA).

Structure						
Name	CID4017446	CID5220994	CID5266986	CID5675221	Hexachlorophene	IPA3
Molecular Weight	154.23	420.44	272.26	451.32	406.90	350.46
Density	1.20	1.49	1.34	1.80	1.71	1.46
# H-bond Donors	1	2	3	1	2	2
# H-bond Acceptors	2	7	5	6	2	2
# Aromatic Rings	1	3	2	2	2	4
LogS (pH = 7.30)	-0.68	-5.04	-2.87	-2.06	-4.87	-6.06
LogP	0.79	2.80	2.47	4.01	7.25	4.92
LogD (pH = 7.30)	0.77	2.66	2.34	0.99	6.05	4.70
Strongest pKa (Acid)	---	7.7 ± 0.2	8.3 ± 0.2	3.7 ± 0.5	6.5 ± 0.5	7.5 ± 0.5
Caco-2	Highly Permeable	Highly Permeable	Highly permeable	Highly Permeable	Highly Permeable	Highly permeable
P-glycoprotein Substrates	Undefined	Undefined	Non-substrate	Undefined	Non-substrate	Undefined
Ames	Undefined	Undefined	Undefined	Undefined	Non-mutagenic	Undefined

hERG	Non-Inhibitor	Non-Inhibitor	Non-Inhibitor	Undefined	Undefined	Undefined
CNS	Penetrant	Non-penetrant	Penetrant	Non-penetrant	Non-penetrant	Non-penetrant
PPB	Weakly Bound	Extensively	Strongly bound	Undefined	Extensively	Undefined
Metabolic Stability	Undefined	Undefined	Undefined	Undefined	Undefined	Undefined
Lipinski	Good	Good	Good	Good	Moderate	Good

Chapter 4: Discussion

4.1 Summary of findings

Using purified recombinant SARS-CoV-2 NSP15, I optimized a fluorescent FRET-based NSP15 activity assay (**Figure 3.1-3.3**). This FRET-based assay was successfully used to screen 108,000+ compounds for NSP15 inhibition across various libraries in the FAM and Cy5 channel. From the primary screen in the FAM channel, the top 1280 hits above two standard deviations were assayed in the secondary screening in the Cy5 channel (**Figure 3.4**). Following screening, a total of nine compounds were confirmed via the FRET-based activity assay to inhibit at least 25% in both channels (**Figure 3.5**). Because the assay utilized DTT, I employed Amplex Red assay to measure H₂O₂ generation, thereby eliminating beta-lapachone as a lead compound (**Figure 3.6a**). Of the remaining eight compounds, I employed a non-fluorescent RNA gel cleavage assay immune to fluorescent quenching for further compound validation (**Figure 3.6b,c**). In total, I verified, in addition to the negative control BenzopurpurinB, the following six compounds after gel cleavage: CID4017446, CID5220994, CID5266986, CID5675221, Hexachlorophene, and IPA3. Of the six compounds, I obtained their IC₅₀ values using both FRET-based activity assay and a non-fluorescent RNA gel cleavage assay (**Figure 3.7-3.8**). Furthermore, I performed Michaelis-Menten titrations (**Figure 3.9**) to determine their putative mechanisms of inhibition. Finally, the compounds were evaluated for both toxicity and efficacy in Vero cells and their potential therapeutic roles were established in inhibiting SARS-CoV-2 viral replication in Vero cells (**Figure 3.10-3.11**). Further characterizations were done on IPA3, whereby a high DTT concentration was found to inhibit IPA3 activity (**Figure 3.12**). Lastly, physical, and biological predictors of the compounds were assessed *in-silico* (**Table 3.4**).

4.1.1 FRET-Assay and RNA Sequence Differences

In setting up the FRET-based activity assay, substrate RNA2 5'FAM-rCrArArCrUrArArArCrGrArArC-BHQ1'3 produced the highest cleavage among the 3 RNAs tested (**Figure 3.1**). While my experiments did not further test the reason for this,

previous findings suggested that NSP15 may not stably bind to DNA, which may explain why the short-length RNA3 5'FAM-dAdArUdAdA-BHQ1'3 had a lower cleavage rate⁵⁸. In addition, SARS-CoV-1 NSP15 has been reported to have minor cleavage activity at the 3' end of cytidines, which may help explain why RNA2 was cleaved better than the no cytidine containing RNA1⁶². Indeed, cyclic-phosphate sequencing of the coronavirus Mouse Hepatitis Virus (MHV) NSP15's physiological targets suggested that a high amount of cytidine is cleaved in addition to uracil⁸¹. Recently, SARS-CoV-2 NSP15 has been shown to exhibit minor cleavages of ssRNA sequences in gel cleavage assays even when the uracil is replaced with cytidine, suggesting that SARS-CoV-2 NSP15 retains minor cytidine cleavage function¹¹⁶. Whether substrate differences between uracil or cytidine would affect NSP15 conformational changes is currently unknown. Lastly, RNA2 sequence corresponds to SARS-CoV-1 spike transcription regulatory sequence (TRS) signal, which makes the sequence more physiological relevant than the other sequences tested⁶³.

4.1.2 NSP15 Manganese Dependency

To further validate the FRET-based assay, NSP15 was found to have required Mn²⁺ but not Mg²⁺ for activity (**Figure 3.1d**). This is in line with both SARS-CoV-1 NSP15 results and recent findings for SARS-CoV-2 NSP15^{9, 10, 62, 117}. Manganese is hypothesized to help stabilize the active site during cleavage, or to help maintain RNA conformation during catalysis, but the exact role is still unclear, especially since manganese ions are not localized to the catalytic site^{9,38}. A recent study also confirmed the use of EDTA to inhibit NSP15 reactions through metal chelation¹¹⁷.

4.1.4 NSP15 Mutants

To help validate the substrate specificity of the FRET-based assay, two NSP15 protein mutants were created. NSP15 H250A mutant showed little to no cleavage activity compared to wildtype (**Figure 3.2b,c**). This is in line with reported literature that showed that SARS-CoV-2 NSP15 H250 was required for RNA cleavage³⁸. H250 is located at the catalytic site and is in hydrogen-bonding distance of the 2'OH of UMP ribose sugar. Such

a position was hypothesized to help start the 2'OH nucleophilic attack for RNA cleavage³⁸. The mutation was first discovered in SARS-CoV-1 NSP15 and thus highlights the conserved nature of NSP15. In addition to the H250A mutant, the Δ 0-28 Δ 336-347 truncation mutant also showed decreased activity cleavage (**Figure 3.2b,c**), in-line with previous SARS-CoV-1 NSP15 mutation of the same nature⁶⁴. Such a truncation affects the N-terminus oligomerization domain. The importance of the N-terminal truncation domain is highlighted by the fact that E3A mutation in the N-terminus, or truncation of the first 28 residues, prevented NSP15 oligomerization and subsequent activity^{63, 64}.

4.1.3 NSP15, DTT, and Amplex Red

Similar to previously reported SARS-CoV-1 NSP15 biochemical assays, the presence of dithiothreitol (DTT) was needed for nuclease activity^{58, 62}. As a reducing agent, DTT donates electrons to help cleave and prevent disulphide bond formation (cysteine to cysteine). Intracellularly, where NSP15 is found, cells usually contain reduced environments owing to the presence of the reducing agent glutathione¹¹⁸. In Mouse Hepatitis Virus (HPV), the NSP15 monomer was shown to contain nine cysteine residues, with Cys80 and Cys95 predicted to form an intramolecular disulphide bond⁵⁷. Cys95 is located at a surface loop and is predicted to help with NSP15 oligomerization. Thus, its oxidation state may affect NSP15 oligomerization and hence activity. The equivalent in SARS-CoV-2 NSP15 would be C103, C117, in addition to the other C291, C293, C334, for a total of five cysteines.

However, due to the presence of DTT in the assay buffer, non-enzymatic redox cycling with certain compounds may generate hydrogen peroxide. Known compounds to produce such an effect include quinones¹⁰⁶. For example, DTT in aqueous buffer can spontaneously produce superoxide anions in the presence of oxygen. At the same time, DTT reduction of quinones can produce hydroxyquinone. The superoxide anions can then bind to hydroquinone to produce H₂O₂ and a semiquinone radical anion¹⁰⁶.

To counter such a possibility, I screened the compounds using for the generation of H₂O₂ using the Amplex Red Hydrogen Peroxide kit. In the presence of H₂O₂, horseradish peroxidase catalyzes the oxidation of Amplex Red reagent (10-acetyl-3,7-dihydroxyphenoxazine) into resofurin in a 1:1 ratio, which can then be measured spectrophotometrically. Using the Amplex Red assay, I found that only beta-lapachone significantly generated H₂O₂ (**Figure 3.6a**). This was not surprising as beta-lapachone is a naphthoquinone. In cells, beta-lapachone can be bioactivated by NAD(P)H:quinone oxidoreductase 1(NQO1), producing a semi-quinone and free radical generation¹¹⁹. As a result, beta-lapachone was likely inhibiting NSP15 through non-specific H₂O₂ generation. Indeed, a previous NSP15 screen also excluded beta-lapachone due to redox cycling¹⁰.

4.1.5 NSP15 Enzyme Kinetics

To further characterize NSP15, NSP15 enzyme kinetics Michaelis-Menten experiments were performed. The experiments found that SARS-CoV-2 NSP15 K_M was 2.9 ± 0.4 μM and V_{max} was found to be 0.29 ± 0.3 μM/min (**Figure 3.3**). In contrast, SARS-CoV-1 NSP15 had a reported K_m of 36.4 ± 6.7 μM and V_{max} of 0.15 ± 0.03 μM/min⁶². However, it should be noted that the SARS-CoV-1 values were found using a different RNA substrate sequence and employed a gel-based system to quantify Michaelis-Menten values, which may contribute to the K_m and V_{max} differences⁶². At the same time, SARS-CoV-1 and 2 NSP15 may have inherently different K_m values, as a recent report found SARS-CoV-2 NSP15 K_m of 2.14 μM, which is similar to this study's K_m of 2.9 μM¹⁰⁹. If true, then SARS-CoV-2 NSP15 may have a higher binding affinity for RNA compared to reported SARS-CoV-1 values.

4.1.6 IC₅₀ Hill-Slope

Interestingly, both our FRET and Gel-based IC₅₀ curves (**Figure 3.7, Figure 3.8**) displayed positive hill slopes for all the compounds (**Table 3.1**). Usually, for protein enzyme activity, a positive hill slope larger than 1 would be indicative of positive protein enzyme cooperativity. Indeed, NSP15 is thought to act as a hexameric unit, as such, the binding of one subunit (perhaps to RNA substrate or to other subunits) may stimulate or

stabilize the rest of the hexameric subunit. Moreover, when an enzyme has more than one binding site, hill slopes can be expected to be higher than 1 in inhibitor IC₅₀ curves¹²⁰.

At the same time, steeper hill slopes for inhibitor IC₅₀ curves may also be dependent on the type of inhibitor¹²¹. Steeper hill slopes (>1.5) may indicate non-specific inhibition such as through aggregation, chemical reactions with the enzyme, or chelation of co-factors¹²¹. Additionally, for inhibitor IC₅₀ curves, tight binding inhibitors exhibit greater than 1 hill slopes due to possibility of titrating the enzyme from its tight binding. By definition, tight-binding inhibitors require concentrations comparable to the enzyme concentration to achieve intermediate levels of inhibition (e.g. 50% inhibition)¹²². Such tight binders are generally potent inhibitors and may be applicable to our strongest inhibitors (CID5675221, Hexachlorophene, IPA3). Additionally, compound solubility problems may also result in steeper hill slopes¹²². This would be applicable to compounds requiring high concentration during curve generation, such as CID5220994, CID5266986. Overall, while positive Hill sloped curves may be due to the hexameric nature of NSP15, more testing, especially for compound aggregation, would be needed to rule out other contributing factors.

4.1.6 Compound Discussion

It total, six compounds passed the *in-vitro* biochemical tests as inhibitors of NSP15: CID4017446, CID5220994, CID5266986, CID5675221, Hexachlorophene and IPA3.

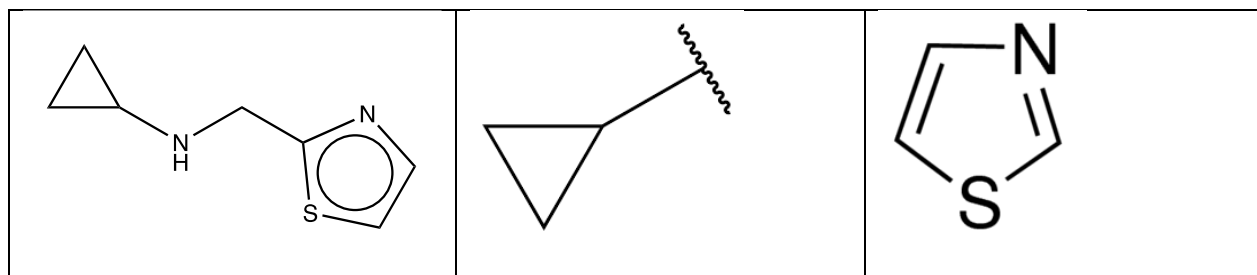
4.1.6.1 CID4017446

To my knowledge, compound CID4017446 has not been published before and no information has existed for its usage. Compound CID4017446 is an interesting compound in that it contains a thiazole group and a cyclopropyl(amine) group connected via a secondary amine (**Table 4.1**). Because cyclopropane has an inherent high ring strain of 27.5 kcal/mol, it is a molecule with diverse function depending on its bonding and site of addition¹²³. Cyclopropyl groups are often added to effective molecules

(including FDA approved drugs) to improve and modify therapeutic usefulness such as potency, selectivity, bio-availability, permeability, stability, solubility¹²⁴. On the other hand, thiazole groups have a wide history in pharmacology and often served as scaffold molecules for many small-molecule compounds and FDA approved drugs¹²⁵. In addition, natural thiazole containing molecules exist such as Vitamin B1 (thiamine)^{126,125}. I found CID4017446 to have gel based IC₅₀ of 64 ± 3.5 μM and FRET based IC₅₀ of 39 ± 2.9 μM. While the Michaelis-Menten curves suggested a competitive inhibition (**Table 3.2**), which would suppose a catalytic binding site, the structure does not naturally suppose a mimic of nucleic acid binding. Unfortunately, I was unable to determine a CC₅₀ as even 400 μM did not induce cytotoxicity. This may be due to a variety of reasons including: compound instability, an insufficiency of 24-hour incubation to induce cytotoxicity, presence of extensive efflux pumps, metabolism of the compound, inability to enter the cell, or high percentage of plasma protein binding. Future experiments could increase the time of compound incubation, use plasma free serum if cell-permitting, and/or use fluorophore attached compounds to visualize cellular uptake. Because the ACD software predicted low plasma protein binding, and that the compound is permeable to Caco-2, the former explanations could be more likely. Indeed, extra care for the storage of the compound must be carried out, as I found that compound stability has been problematic and unreliable. Interestingly, the similar compound, dicyclopropyl-thiazole, was found to be non-toxic against human lung fibroblasts (CCD-11Lu) up to high dose of 25 μg/mL and 72 hours tested¹²⁷. Nevertheless, due to the presence of the thiazole group, a privileged group, CID4017446 could be more favorable to chemical alterations. Possible alterations could include adding alkyl groups to the thiazole as steric shield to prevent possible protein cleavage. Overall, CID4017446 is an interesting compound due to its unique structure and poses interesting questions of its cellular interaction and possible mode of binding.

Table 4.1: Chemical structure of compound CID4017446 and its moieties.

CID4017446	Cyclopropyl	Thiazole



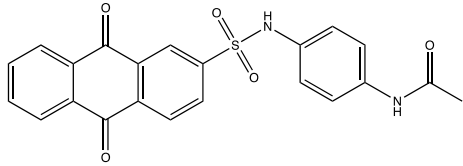
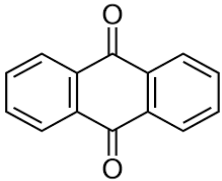
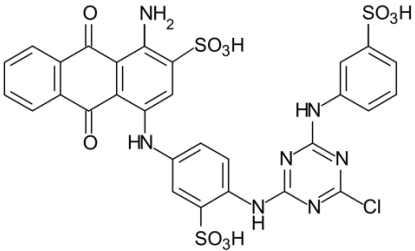
4.1.6.2 CID5220994

For compound CID5220994, it should be noted that the compound contains an anthraquinone group (**Table 4.2**). Such a group is found frequently in proteins with nucleotide-binding sites, in particular those containing ATP-, ADP-, or AMP (adenosine monophosphate)-binding motifs¹²⁸. It is thought that the anthraquinone group mimics adenosine binding. Indeed, X-ray crystallography of rat ectonucleoside triphosphate diphosphohydrolase2 nucleotide binding site showed anthraquinone binding¹²⁸.

Likewise, based on the Michaelis-Menten results (**Figure 3.9**), CID5220994 is predicted to be a competitive inhibitor. Thus, I hypothesize that the compound is likely binding to NSP15 catalytic core to compete with RNA binding. Drugs of the anthraquinone class also include doxorubicin, which is thought to stabilize topoisomerase II from re-ligating DNA ends¹²⁹. Interestingly, Reactive Blue 2 is also an anthraquinone (**Table 4.2**), but was dropped from further characterization due to incompatibility with the gel-based assay (**Figure 3.6b**). Despite anthraquinone molecules being known to show preference for binding to proteins containing nucleotide-binding sites, they are also frequent hitters of small-molecule screens and are likely promiscuous towards other nucleotide-binding proteins as well¹²⁸. In addition, anthraquinones, such as doxorubicin, may undergo enzyme-catalyzed redox cycling with flavoenzymes, generating reactive oxygen species (ROS) inside the cell, which may explain the cytotoxicity of CID5220994 in Vero cells with an CC_{50} of $41 \pm 5.2 \mu\text{M}$ (**Table 3.3**). Despite passing the Lipinski rule of five, CID5220994 was predicted to have extensive plasma proteins binding which may complicate, and likely decrease, the bioavailability of the compound (**Table 3.4**). Possible strategies to overcome such challenges include adding steric shields, such as the

addition of alky groups to the phenyl acetamide to prevent hydrolysis or protein recognition, and to improve compound chemical stability. The sulphone bond in CID5220994 may also be susceptible to cleavage or attacks, and its replacement by more stable bonds may improve chemical stability. Nevertheless, CID5220994 is of anthraquinone class, and such a group may be interesting in NSP15 inhibitor drug design.

Table 4.2: Chemical structure of compound CID5220994 and anthraquinones.

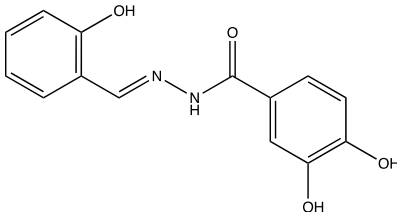
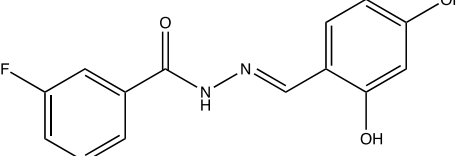
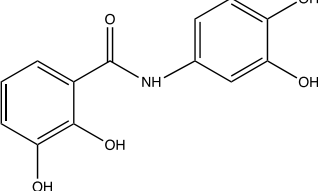
CID5220994	Anthraquinone	Reactive Blue 2
		

4.1.6.3 CID5266986

Compound CID5266986 bears a passing resemblance to the structures of CID5326429 and to recently published NSP15 inhibitor Exebryl-1 (See **Table 4.3** for chemical structure comparison). Compound CID5326429 was not further pursued due to little to no inhibition on the initial gel assay (**Figure 3.6**). This could be due to it being a weaker inhibitor and requiring higher than 50 μM to yield a gel assay result. Nevertheless, CID5266986, CID5326429 and Exebryl-1 all appear to be chemically similar as they all contain dihydroxybenzenes (**Table 4.1**). Exebryl-1 appears to be two catechol groups linked by an amide bond. CID5326429 appears to be ethylamine resorcinol linked to fluorobenzamide via nitrogen bonding. CID5266986 appears to be a dihydroxybenzamide linked to a hydroxybenzonitrile via the nitrogen bond. Given the structural similarity, they may share the same binding pocket to NSP15. Exebryl-1 was confirmed to bind to NSP15 via native mass spectrophotometry in a non-covalent way¹⁰.

Computer docking predicted Exebryl-1 binding to two places with slightly higher probability at: Site 1) a pocket formed between the N-terminal oligomerization and C-terminal catalytic domain contacting residues Lys71, Thr275, Tyr279, but not the catalytic site itself, versus Site 2) the catalytic pocket site. As a result, I expect compounds CID5266986 and CID5326429 to bind similar sites to Exebryl-1. Michaelis-Menten results showed CID5266986 binding in a mixed formation, which could be indicative of both sites. CID5266986 produced a FRET-assay IC_{50} of $53 \pm 3.0 \mu M$. Meanwhile Exebryl-1, in similar FRET assay setup, produced an IC_{50} of $1.3 \mu M$. It could be hypothesized that the addition of extra catechol group in Exebryl-1 could be reason for increased inhibition (**Table 4.3**). It could also be hypothesized that CID5326429 produced reduced inhibitory activity than CID5266986 due to having a fluoride group in place of the hydroxyl group, as phenols are known to be more nucleophilic than fluorobenzene (**Table 4.3**). While compound CID5266986 was not tested for Vero IC_{50} , it was shown to produce an CC_{50} of $42 \pm 4.8 \mu M$ (**Table 3.3**). Given that the compound was predicted to have passed the Lipinski rule and was predicted to be highly permeable to Caco-2, in addition to being a non-substrate to P-glycoprotein, the data could be indicative of positive signs for further downstream refinement (**Table 3.4**). However, while it is promising to having chemical similarity between different published hits, it should be cautioned that catechols are known PAIN molecules that could be redox and protein reactive¹³⁰. However, given the published data on Exebryl-1, I hypothesize that the compounds do not produce redox or covalently modify proteins. More direct binding assays are needed and explained in future directions (**chapter 4.3**).

Table 4.3: Chemical structure of CID5266986, CID5326429 and Exebryl-1.

CID5266986	CID5326429	Exebryl-1 ¹⁰
		

--	--	--

4.1.6.4 CID5675221

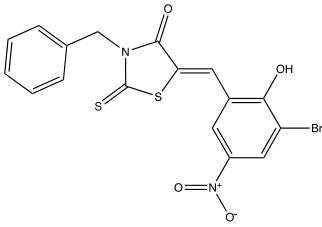
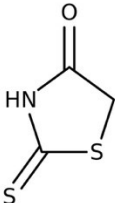
To my knowledge, compound CID5675221 has not been published before and no information exists for its usage. At the centre of this chemical is a rhodanine group (**Table 4.4**). Rhodanine groups have been used in screening compounds against hepatitis C and human immunodeficiency virus (HIV). For example, rhodanine derivatives have been used to inhibit HIV NS5B polymerase with IC_{50} of $7.7 \mu M$ ¹³¹. As well, Rhodanine derivatives have been found to potently inhibit HIV-1 entry through interactions with its transmembrane protein gp41 with EC_{50} as low as $2.2 \mu M$ ¹³². Only Epalrestat, a rhodanine containing molecule, has been medically approved for human use (and only in Japan). Epalrestat is a reversible non-competitive inhibitor of aldose reductase and is approved for diabetic neuropathy in Japan only, however future Phase IIb clinical trials using Epalrestat have been proposed in the United States¹³³.

I found CID5675221 to have an CC_{50} of $248 \pm 33 \mu M$ (**Table 3.3**). This is least toxic of the compounds with CC_{50} values. The compound produced a Vero IC_{50} of $19 \pm 2.3 \mu M$ against SARS-COV-2, the highest IC_{50} value, and subsequently produced the second highest SI_{50} value of $15 \pm 3.8 \mu M$ (**Table 3.3**). While the compound has passed the Lipinski's rule and was predicted to be highly permeable to Caco-2, the software was unable to predict the other parameters. However, given the calculatable data, the results could bode well for further downstream refinement.

However, rhodanines have been recognized as a pan assay interference (PAIN) compound¹³⁰. This is due to its ability to interfere photometrically in the 570 nm and 620 nm range. CID5675221 does cause significant quenching, especially in the Cy5 channel of 645/670nm but with limited quenching in the FAM channel of 490/520 nm (Figure 3.5). At the same time, the compound is traditionally difficult to further modify due to the compound's thioxo group, whereby it has the potential to engage in many interactions,

possibly covalently, leading to promiscuous binding, and frequent hits in biological high-throughput screens¹³⁰. Despite this, rhodanine based compounds have been successful in producing selective hits such as against UDP-*N*-acetylmuramoyl-*L*-alanine:*D*-glutamate ligase (MurD)¹³⁴. Additionally, rhodanine compounds can aid in drug design due to their ability to easily form crystalline complexes and structure¹³². As a result, rhodanine based molecules can be a good starting stage for binding mode discovery, whereby the rhodanine groups can be switched out at a later stage.

Table 4.4: Chemical structure of CID5675221 and Rhodanine.

CID5675221	Rhodanine
 <p>The chemical structure of CID5675221 features a rhodanine core (a five-membered ring with a sulfur atom, a carbonyl group, and a nitrogen atom) substituted with a benzyl group on the nitrogen and a 4-bromo-2-nitrophenyl group on the 2-position of the rhodanine ring.</p>	 <p>The chemical structure of Rhodanine is a five-membered heterocyclic ring containing one sulfur atom, one nitrogen atom, and one carbonyl group, with a double bond between the nitrogen and the carbon adjacent to the sulfur.</p>

4.1.6.5 Hexachlorophene

Hexachlorophene was a widely used disinfectant found in topical treatments and toothpaste and is regarded as safe to use externally at (<1%)¹³⁵. It is not recommended/banned for use internally, as animal studies in rats and pigs found hexachlorophene induced paralysis and neurotoxicity at high doses¹³⁶. Hexachlorophene was found to inhibit mouse hepatitis virus (MHV) infection in mouse astrocytoma (DBT) cells with an IC₅₀ of 1.2 μM with unknown mechanisms¹²⁰. Interestingly, hexachlorophene was previously shown to inhibit SARS-CoV-2 viral titer in HEK293T cells with an IC₅₀ of 0.9 μM with an unknown mechanism¹³⁷. Despite known cell culture data of viral efficacy, it should be noted hexachlorophene could bind promiscuously as it has been implicated in binding to SARS-CoV-1 3CL protease with IC₅₀ of 4 μM¹³⁸.

I found hexachlorophene to have an CC₅₀ of 15.4 μM ± 4.59 μM (**Table 3.3**). This is most toxic of the compounds tested. However, I found hexachlorophene inhibited SARS-CoV-

2 in Vero cell culture with an IC_{50} of $0.95 \pm 0.016 \mu\text{M}$ (**Table 3.3**). Subsequently, hexachlorophene had a calculated SI_{50} value of $16 \pm 4.7 \mu\text{M}$, which was the largest SI_{50} value the tested groups. Usually, a high SI_{50} bode well for drug development. However, it was unknown what the *in-vivo* targets of hexachlorophene were; hexachlorophene could bind to other viral proteins to inhibit viral titers. Indeed, reactivity could be a problem as hexachlorophene was predicted to have extensive high plasma protein binding (**Table 3.4**). Depending on how hexachlorophene binds, hiding or masking polar groups, such as the hydroxyl groups, may help decrease off-target reactivity. Although the software did not predict CNS penetration, hexachlorophene was banned due to potential of neurotoxicity¹³⁶. However, typical antiseptic 3% hexachlorophene is 73.7 mM, whereas the reported IC_{50} values of hexachlorophene in cell culture is more than ~50,000 times lower¹³⁹. While a more safer compound would be needed for any clinical application, nevertheless, the results here showed that hexachlorophene to be a strong inhibitor of NSP15 in biochemical assay, and would interesting from drug design standpoint to determine the site of binding in future directions.

4.1.6.6 IPA3

IPA3 is a known uncompetitive inhibitor of group 1 p21-activated kinases (PAK)¹⁴⁰. Group 1 PAKs are a family of serine/threonine protein kinases¹⁴⁰. They are autoinhibited as a homodimer unless bound to Guanosine-5'-triphosphate (GTP) activated Rac or Cdc42. Activated PAKs act on more than 40 identified substrates and a variety of cellular processes, including progression of cell cycle, protection from cell apoptosis, cell motility and cancer metastasis.¹⁴¹ IPA-3 was found to target the autoregulatory domain of group I PAKs with $2.5 \mu\text{M } IC_{50}$ ¹⁴⁰. Interestingly, IPA3 was found to be inactivated by DTT, potentially due to direct DTT reduction of IPA-3 compound¹⁴⁰. At the same time, IPA3 may bind to PAKs in a covalent manner¹⁴⁰. As a result, IPA-3 may also potentially form mixed disulphides with NSP15 cysteine residues. I attempted to test the effect of reducing agent DTT on IPA3 to evaluate this hypothesis. As shown in **Figure 3.12**, I found that higher DTT concentrations abolished IPA3 inhibition activity. This may indicate that IPA3 inhibition relies on NSP15 cysteine bonds. However, the result could

also be interpreted as DTT reacting to the IPA3 disulphide bonds, thereby destroying the compound structure. While Michaelis-Menten curves suggested a non-competitive inhibition for IPA3 (**Figure 3.9**), if IPA3 is a covalent inhibitor due to cysteine bonding, it too would result in non-competitive kinetics when protein concentrations were more than inhibitor concentrations. Future experiments, such as crystal modelling of binding, may be useful in further testing of IPA3 mechanics.

Because intra-cellular environments are usually reducing due to an abundance of glutathione, with estimates ranging from 0.5 to 15 mM, IPA3 may be reduced before reaching its *in-vivo* targets¹⁴². This may pose a challenge to IPA3 delivery¹⁴². At the same time though, due to its sulfhydryl moiety, IPA3 may also lead to non-specific effect binding in cells, producing toxicity. Indeed, I found IPA3 to have an CC₅₀ of 38 ± 3.9 µM in Vero cells (**Table 3.3**). The presence of cytotoxicity suggested that the compound was reacting to off-targets intracellularly. At the same time, binding to PAK proteins may also have contributed to the cytotoxicity, as inhibition of PAK proteins can lead to cellular apoptosis¹⁴⁰.

Surprisingly, I found that IPA3 was effective in stopping SARS-CoV-2 replication in Vero cells, with a IC₅₀ of 7.9 ± 0.89 µM, and a subsequent SI₅₀ of 5.4 ± 1.2 µM (**Table 3.3**). This cellular IC₅₀ was comparable to the biochemical gel-based assay IC₅₀ of 4.8 ± 0.55 µM and the FRET-based IC₅₀ of 9.8 ± 0.35 µM (**Table 3.2**). IPA3 also passed the Lipinski rule test, and the software predicted that it is highly permeable to Caco-2 (**Table 3.4**), suggesting good bio-absorption and ADME metrics, and a favorable compound for further downstream optimization. However, the drug was also predicted to be a CNS penetrant and there is currently unknown safety data on human consumption of IPA3. Usually, to overcome problematic CNS penetration, specific site and type of delivery methods are tailored. As well, the addition of polar groups, such as amide or alcohol groups will help prevent CNS penetration¹⁴³. At the same time, depending on the IPA3 method of binding (especially if the binding is non-covalent), I may remove the sulfhydryl bonds to decrease chances of off-target effects and likely improve compound

metabolic stability. Overall, IPA3 is an interesting molecule, with a positive SI₅₀ ratio, which bodes well for downstream applications.

4.1.6.7 On the Possibility of Covalent Interactions of Inhibitors

While I hypothesize that the compounds tested may bind in non-covalent manner, without further functional structural analysis (elaborated in future directions), I cannot rule out covalent binding. This is especially important for IPA3 due to possible cysteine interaction. Such covalent inhibitor typically acts in a two-step manner, whereby the inhibitor first binds the protein in a reversible equilibrium bond formation, after which, a covalent irreversible bond is formed¹⁴⁴. It should also be noted though that covalent inhibitors do not necessarily constitute a detriment to the drug pipeline for coronavirus treatment. Traditionally, covalent modifiers are frowned upon in pharmacology due to safety concerns of their ability to covalently modify off-target cellular proteins²⁴. However, numerous U.S Food and Drug Administration (FDA) approved covalent inhibitors exist²⁴. The most pertinent to the topic is Pfizer's Paxlovid, which has FDA emergency use approval for COVID, and has seen 89% effectiveness against serious illness in COVID clinical trials¹⁴⁵. Paxlovid (whose key ingredient is Nirmatrelvir), targets the coronavirus protease 3CL, through a reversible covalent bond between its nitrile group and the protein's cysteine group. Indeed, cysteine residues are considered a viable and promising target of reversible covalent inhibitors¹⁴⁶. Such a strategy may apply to SARS-CoV-2 NSP15, such as through targeting of C103, C117 of the oligomerization domain, or through NSP15 C291, which is close to the active site and is thought to be reactive¹¹⁶. The other possible site is C291. Although C291A mutants previously showed no oligomerization or decreases in activity phenotype, it is unknown if larger molecular inhibitor modifications to that site may affect NSP15 activity¹¹⁶. Such a scenario may be possible for IPA3, whereby its prominent disulphide bond structure allows for the hypothesis of inhibition via binding to NSP15's cysteine groups.

4.1.6.8 In the Context of Viral Treatments

The compounds this project aimed to find are but a small part in the global fight against SARS-CoV-2. Despite the development of SARS-CoV-2 vaccines, there is still the need to find effective anti-coronavirus therapies, in part due to problems relating to vaccine penetration, breakthrough infections, the rise of COVID variants, and the possibility of novel future coronavirus outbreaks. Currently, no FDA approved SARS-CoV-2 antiviral small molecules target NSP15. FDA approved small molecule treatments currently include: Paxlovid (nirmatrelvir with ritonavir), Veklury (remdesivir), and Lagevrio (molnupiravir)¹⁴⁷. Briefly, nirmatrelvir is a 3CL protease inhibitor involving a covalent cysteine modifying nitrile warhead¹⁴⁸. Molnupiravir is a prodrug of the nucleoside analogue EIDD-1931, and was shown to impair SARS-CoV-2 replication by increasing the frequency of viral mutations (through mimicking cytidine or uridine) during RNA-dependant RNA polymerase (RdRp) based replication^{149, 150}. Lastly, remdesivir (originally named GS-5734) is also an prodrug nucleoside analogue¹⁵¹. As such, it is apparent from the current FDA approved compounds, that most of the anti-viral small molecule drug discovery effort focused on two protein targets: the polymerase, and the protease. As a result, NSP15 represents a novel and distinct therapeutic target.

In addition to the FDA approved therapies, there is pipeline of emerging pre-clinical SARS-CoV-2 antivirals with novel viral targets, in addition to NSP15. Promising leads include oridonin targeting NSP9. NSP9 is a conserved homodimeric RNA binding protein essential for viral replication, and the protein was found to be regulated by the addition of nucleoside monophosphate (NMP) by NSP12, though more research is needed to determine its physiological significance¹⁵². Recently, NSP9 over-expression was found to decrease nuclear pore protein NUP63 and impair NF- κ B response¹⁵³. Oridonin was confirmed via native mass spectrometry to bind to NSP9 with a K_d of $\sim 7.2 \pm 1.0$ μ M, and was found to have produced 5 log of viral titer reduction in Calu-3 cells after 24 hours¹⁵⁴. Selectivity index for oridonin was not measured in the study¹⁵⁴. In addition to NSP9, small molecule screens have been done for NSP13 helicase and NSP14/10 exonuclease as well¹⁵⁵. Of which, the strongest inhibitor was suramin, targeting NSP13.

NSP13 is an essential protein for coronavirus replication and is thought to be part of the replication transcription complex as the helicase³⁴. Suramin was found to inhibit NSP13 at an IC₅₀ of 1.6 μM enzymatically, with an Vero EC₅₀ of 9.9μM, and no cytotoxicity at 300 μM tested, and thus produced a subsequent SI₅₀ of >30¹⁵⁶. All in all, the above pre-clinical compounds inhibited enzymatically at ranges similar to the strongest inhibitors in this project (CID5675221, hexachlorophene, IPA3), but suramin produced a slightly larger SI₅₀ compared to this project's compounds (which were 15 for CID5675221, 16 for Hexachlorophene, and 5.34 for IPA3; **Table 3.3**).

However, the above pre-clinical compounds (including molecules discovered in this project) are vastly less potent in comparison to known FDA approved SARS-CoV-2 small molecular inhibitors. Nirmatrelvir (its precursor PF-00835231) was first discovered from a FRET screen with a K_i of 230 nM, and was modified into nirmatrelvir with a final K_i of 3.11 nM and an EC₅₀ of 74 nM in Vero E6 cells^{148, 157}. Nirmatrelvir has been reported to have a CC₅₀ of >100 μM in Vero E6 cells, which would produce an apparent SI₅₀ of >1351¹⁵⁸. Meanwhile, molnupiravir (specifically EIDD-1931) inhibited SARS-CoV-2 in Vero cell culture at an IC₅₀ of 0.30 μM¹⁵⁰. *In-vitro* data found that EIDD-1931 produced an SI₅₀ of 1.24 to >130 depending on the cell line used¹⁵⁹. Meanwhile, remdesivir inhibited SARS-CoV-2 in Vero cell lines at an EC₅₀ of 1.65 μM with an selectivity index of over >129^{160,161}. Thus, these FDA approved compounds not only have higher potency (in the nM range) but also higher SI₅₀ (>100 range) than this project's compounds (whose SI₅₀ ranged from 5.34 to 16; **Table 3.3**). However, these differences are not entirely unexpected. For example, screening with nucleoside analogues is simplified by the existence of curated nucleoside analogue screening libraries, and the predicted mechanism of such analogues insures higher potency against polymerase protein targets, such as in the case of molnupiravir and remdesivir^{162, 163}. Additionally, there is a history of drug designs against coronavirus 3CL main proteinase, many, including starting designs for nirmatrelvir, were derived from SARS-CoV-1 and rhinovirus 3C proteinase inhibitors¹⁶⁴. As such, it is expected for this project's random compound screen to yield compounds with lower affinities than the above rational screens.

Additionally, it is expected of antiviral compounds to have high selectivity index for FDA approval, given the nature of required selectivity for therapeutic safety. For example, FDA approved cabotegravir (GSK1265744), against HIV integrase, produced a selectivity index of >22,000 in *in-vitro* cell culture^{165, 166}. As such, the compounds discovered in this project against NSP15 will need vast improvements in binding affinity and selectivity index, such as through rational drug design and/or compound modifications, in order to reach therapeutic potential. Thus, the compounds discovered here against NSP15 are merely starting points for such further lead optimization in the hit-to-lead pipeline.

Additionally, while NSP15 could be an effective therapeutic target as a modulator of interferon and immune evasion⁴⁰, immune modulation relies on an intricate network of proteins and pathways. Numerous coronavirus proteins have been implicated in modulating or interacting with RIG-I-like receptor/MAVS pathway, such as NSP16, NSP14, NSP13, NSP10, NSP5, NSP3, ORF9b, and even membrane (M)¹⁶⁷. As such, targeting NSP15 alone may not produce the desired effect due to pathway redundancies. This perhaps may explain why some our compounds failed to inhibit SARS-CoV-2 replication *in-vitro* (**Figure 3.11**) and/or produced lower than desired selectivity index values when compared to FDA approved anti-SARS-CoV-2 antiviral molecules. As a result, should any NSP15 targeted therapies arise, they would most likely be part of a cocktail therapy targeting the numerous key NSP proteins (such as in the immune evasion pathway), or in conjunction with current FDA approved or preclinical compounds. Treatment could also be complicated by the fact that SARS-CoV-2 is known to induce cytokine storm, as such, to prevent further induction of cytokines by interferon response, the timing such therapies would be important, predictably in the very early stages of infection¹⁶⁸.

4.1.6.9 Summary and Application of Research

This project has established a high-throughput NSP15 screen and has discovered six novel SARS-CoV-2 NSP15 inhibitors that work in *in-vitro* biochemical assays, and of

which, three have been shown to block SARS-CoV-2 viral replication in Vero cell culture. Previously, only two compounds are known to successfully inhibit SARS-CoV-2 NSP15. If the six compounds in this study are successfully validated in further downstream binding and cell assays, these novel compounds would greatly increase the repertoire of known NSP15 inhibitors and potential candidates for SARS-CoV-2 treatments. Because NSP15 is highly involved in immune evasion, NSP15 inhibitors may have therapeutic potential in helping the immune system recognize viral infection, especially at the early COVID-19 infection stage. The methods and results in this study will also aid in the design and search of novel NSP15 therapeutic agents, and will also provide the basis for expanded high-throughput screening of NSP15 inhibitors. Because NSP15 is highly conserved across coronavirus species, identifying SARS-CoV-2 NSP15 inhibitors will also help the scientific and medical community better prepare for and research other coronavirus species, including potential future coronavirus species and/or coronavirus variants.

4.2 Limitations

4.2.1 Screening and FRET-based Assay Limitations

While the project was able to obtain putative NSP15 inhibitors during the screens, the high throughput (HTP) screen has encountered many known pan-assay interference compounds (PAIN) that have ended up as final hits^{169, 170}. These include the well-known flavone compounds such as quercetin and fisetin, which are considered false positives as they are known to bind promiscuously and often via non-specific methods^{169, 170}.

While such occurrences are not entirely unavoidable, library selection and pre-screen *in-silico* filtering of known PAIN molecules can help prevent such occurrences and help save follow-up time and resources⁹⁴. The final hit rate using compounds validated for NSP15, compared to the original 108,000 + compounds screened, was ~0.005-0.015% depending on if you include the known PAIN molecules. While such a rate is acceptable and is in line with the average hit rate of 0.01% to 0.14%, it is on the lower end of the range¹⁷¹. While careful library selection, and *in-silico* screening of inhibitors prior to HTP

screening, are known to enhance success rate, many aspects of this study's assay can also be improved to help with hit selection, such as through a higher signal to noise (S/N) ratio and preventing false positives¹⁷¹.

For example, while I assumed that pH ranges are stable due to the HEPES buffer in the FRET-based assay, compounds that can affect pH may unknowingly tilt the assay pH and result in quenching due to the pH-sensitive nature of Cy5 cyanine dyes. An alternative would be to use derivatives such as Alexa Fluor 647 in the RNA substrate design, which are generally considered pH in-sensitive and more photostable¹⁷². In addition, while I found 100mM ethylenediaminetetraacetic acid (EDTA) was an effective stopping reagent, the dosage has led to significantly increased background fluorescence (**Figure 3.1**) which decreased the assay S/N ratio. An alternative was to perform a manganese titration to find an acceptable lower manganese concentration that does not impact NSP15 activity, which would facilitate likely lower EDTA usage. Additionally, the screen could also have been setup without the use of a stopping reagent. In **Figure 3.6a**, it was shown that the NSP15 assay could be prone to dithiothreitol (DTT) redox cycling when detected with Amplex Red. This was an inherent flaw to the assay that may result in false positives in future screens. While a reducing agent was found to be needed for optimum NSP15 activity (**Figure 3.12**), other milder reducing agents such as glutathione or β -mercaptoethanol may be preferred for screening to prevent redox cycling. While I take great lengths to try and reduce false positives, additional assays could be needed. Many PAIN molecules are colloidal aggregators that self-assemble into a liquid to liquid phase separation and form promiscuous inhibition¹⁷³. These can form up to 95% of identified hits^{173,174}. To my knowledge, online databases for tracking such PAINs few and not properly maintained or accessible. To avoid such compounds, counter screens done with 0.1% Triton or with β -lactamase should be done to rule out potential colloidal aggregators¹⁷⁴. Additionally, the compounds provided for the secondary screen(s) were shipped and frozen in aqueous buffer at -20°C for week(s) before screening. As a result, this procedure may have resulted in compound degradation and a subsequent decrease in active hits. Future screening should be done

with compounds directly taken from stock plates. Finally, a shorter substrate length between the fluorophore and quencher would likely result in less background and a higher S/N ratio for the assay to help improve hit detection rate; the spacer between fluorophore and quencher should also be optimized.

At the same time, additional optimizations of the FRET-based activity assay buffer may have benefited the experiments and screening. It has been reported that NSP15 crystallized in the presence of citrate, forming hydrogen bonding with His235, His250, Lys290, and Thr341, which was hypothesized to stabilize the active site¹⁰⁴. Indeed, the addition of citrate to HEPES buffer was recently shown to enhance NSP15 cleavage activity, suggesting that such an addition may benefit NSP15 assays¹¹⁷.

In addition, a major limitation of the high-throughput screening was the number of compounds screened. While close to 108,000 compounds were screened, it is well known that typical HTS screens, especially at the industry level, requires millions of compounds to identify suitable pharmacological inhibitors for clinical development. The selected hits found here may not be representative of the diversity of true NSP15 inhibitors. In addition, it should be noted that the NSP15 screening performed solely looked at inhibition of NSP15 endonuclease activity. NSP15 may modulate coronavirus infection independent of its nuclease activity, as explained in **chapter 1**. As a result, inhibitors of binding sites that do not affect nuclease activity may not have been picked up by the screen.

4.2.2 Gel-Based IC₅₀

In the gel-based cleavage assays, I found ~5x higher gel-based IC₅₀ versus its FRET-based IC₅₀ counterpart for compound CID5675221 (**Figure 3.7-3.8**). This is not entirely uncommon as previous NSP15 inhibitor studies have found as much as ~9x difference between FRET-based and gel-based compound IC₅₀s, suggesting that the RNA gel-based IC₅₀s could be prone to producing higher IC₅₀ values than their FRET-based counterpart¹⁰. One explanation is that for the gel-based assays, I used absolute IC₅₀

calculations based on the uncleaved negative control (no NSP15) band, which may bias toward higher IC₅₀ values. Additionally, because compound CID5675221 has been shown to partially quench in the FAM channel at 25 and 50 μM (**Figure 3.5c,d**), possible increased quenching effects at higher compound concentration values could increase apparent inhibition values. A more complex IC₅₀ setup where assay signal is normalized against potential quenching at each compound concentration point measured against a FAM positive control could be used to help mitigate such a scenario. To my knowledge, no other studies using FRET-based RNA screening have investigated such potential quenching effects of their compounds, nor have they attempted IC₅₀s in such a manner. Additionally, due to the increase in protein and RNA concentrations present in the gel-based assay, more compound concentration may be needed to accomplish the same inhibition. Future experiments in **chapter 4.3** could help address alternative methods of finding inhibition values.

I also found that the gel-based assay could not test the compound, Reactive Blue 2, due to fluorescent interference of the compound that occluded the band of interest. This was most likely due to the compound migrating at the same speed as the RNA band. As a result, either different RNA substrate lengths or purification of RNA prior to gel loading would be needed. Future experiments in **chapter 4.3** can address such a problem via alternative ways of measuring compound binding.

4.2.3 Vero Cell Culture and Plaque Assay Limitations

For the Vero cell CC₅₀ data, I was limited by agent availability and compound solubility. In some cases, to achieve 400 μM doses, I had to resort to 1% DMSO, which resulted in a decrease in Vero cell growth but not lethality. As a result, a separate DMSO control group was included for each concentration DMSO used in the compound serial dilution. At the same time, CID4017446 could not produce cytotoxicity in the experiments. This could be due to a variety of reason listed in the discussion, including the possibility that longer incubations times are needed for the compounds to induce toxicity. However, only

24h incubation times was tested, thus longer incubation times should be done to test this theory.

Additionally, I chose the cell line, Vero (derived from African Green Monkey kidney) due to its ease of viral infection and usage in viral studies¹⁰⁸. However, Vero cell lines are not human derived and may not be representative of human host cell infection. In addition, Vero cells lack interferon response, possibly due to genetic defects¹⁰⁸. As a result, other cell lines, such as human lung epithelial cancer cell line, Calu-3, may be more suitable to the study of NSP15 and its effect on the interferon pathway. At the same time, due to difficulty of Biosafety level 3 (BSL3) work, just the top 3 compounds were tested in detail. Additional time, effort, and resources are needed to test the other compounds in more detail, and possibly in other cell lines as well.

While plaque assay is a good gauge of viral replication, it does not directly measure viral entry. Quantitative polymerase chain reaction (qPCR) of viral genes, or western-blot of viral proteins from infected cells, can directly detect intracellular markers of infection. Additionally, the Vero cell culture IC₅₀ does not measure if the compounds are binding to NSP15 target *in-vivo*. Decreases in the viral titer could also be due to off-target binding of other viral proteins. In the plaque assays, because the virus was co-incubated with the compounds at the same time, compounds that block viral entry instead may result in the same viral titer decrease. To remedy this, compounds can be added post-infection. Indeed, elucidating the timing window of compound effectiveness on viral infection can help determine at what stage of viral infection the compound act upon. Additionally, alternative markers should be chosen for measurement, such as interferon induction. It should be noted that a reduction in viral titer does not necessarily mean NSP15 induction, and vice versa, an induction of interferon does not necessarily mean a reduction of viral titer, as shown in other coronavirus studies (see **chapter 1.5** for more explanation). As a result, it is prudent to include a NSP15 catalytic deficient mutant virus to show the maximal effect of NSP15 inhibition in the cell lines.

Last, due to the use of only cell culture, and given the rise of SARS-CoV-2 variants, the experiments here are limited in scope and are likely not reflective of true physiological infection or may not be reflective of the current dominant strains of infection.

4.2.4 Michaelis-Menten

Lastly, due to NSP15 being a hexameric unit, cooperativity under certain conditions may be possible. If NSP15 activity is cooperative, then Michaelis-Menten equations would not be suitable for the analysis and a sigmoidal curve would be preferred. However, limited data is available on this subject, and previous SARS-CoV-1 NSP15 papers performed enzyme reactions assuming hyperbolic curves⁶². More detailed enzyme testing, in addition to a hill curve analysis, would be needed to determine if there is cooperativity and if a sigmoidal enzyme curve would be more appropriate. It would also be interesting to see if compound binding requires NSP15 to be in a hexameric, trimeric, or monomeric condition.

Additionally, while I tried to improve the accuracy of the Michaelis-Menten curves by performing them at two inhibitor concentration doses (**Figure 3.9**), the curves generated may still not be fully accurate due to the large standard deviations observed. Future experiments could improve Michaelis-Menten accuracy by increasing the number of substrate dosages, as well as increasing the maximum substrate dosage tested. Furthermore, other types of molecular interaction assays could be used to probe for enzyme binding affinity, as discussed in future directions below.

4.3 Future Directions

To further delineate mechanisms of compound inhibitor binding to NSP15, I suggest surface plasmon resonance (SPR). SPR is a label free spectroscopy technique to monitor molecular interactions^{175,176}. A typical (Kretschmann configuration) setup involves analyte (NSP15 protein) immobilized to a gold surface and connected to a microfluidic system. The ligand (the compounds) will then be flowed through the microfluidic system and binds to the analyte/NSP15 protein. After binding and equilibrium

is established, running buffer is continuously injected to dissociate the ligand/analyte binding (dissociation phase). Such dissociation will cause subtle changes in light when shined upon by a polarized laser source passing through a prism setup and finally recorded by a detector. Specifically, the detector will measure angle change of light which is reflective of changes in the refractive index resulting from interactions and hence binding. Such a setup allows for measurement of binding affinity such as the association rate constant (k_a), dissociation rate constant (k_d)¹⁷⁵. These are important biophysical parameters that measure affinity of compound binding and is useful in further study of structure-function relationships. To this end, I am currently collaborating with other labs to complete this objective.

To further understand structure-functional relationship, future work may involve solving crystal structures of the compounds with the NSP15 protein. X-ray crystallography allows for three-dimensional molecular structure and the identification of specific binding residues of the inhibitor-protein relationship. Briefly, high concentrations of highly purified NSP15 protein would be crystallised with the inhibitor and subjected to X-ray diffraction¹⁷⁷. Crystallization usually occurs in a vapor diffusion chambers, such as in the sitting drop vapor diffusion chamber. In such a chamber, a droplet of protein is seated in a raised post and is surrounded by a liquid reservoir. To form vapor equilibrium, water molecules would leave the protein droplet, leading to supersaturation of the droplet and protein crystallization.¹⁷⁷ Following X-ray of the crystal, the diffraction patterns of the repeating crystal lattice would then be processed to obtain an electron density map and fitted to protein sequence and conformation. Softwares could include HKL2000/3000, using CCP4 for electron density map generation, and Phenix for structure determination^{178, 179}. One of the major difficulties of X-ray crystallography is obtaining a solution that sufficiently supersaturates the protein droplet in a slow and controlled manner to form a homogenous crystal. This is confounded by the addition of compounds, which naturally introduce heterogeneity into the system, impeding crystal formation. These challenges may hinder the crystallization of the protein, and ultimately

the overall achievable resolution¹⁷⁷. To this end, I am currently collaborating with other labs to complete this objective.

To further study if the compound inhibitors found are effective against SARS-CoV-2, one can also test compound effects on interferon induction instead of viral titer. In theory, blockage of NSP15 would cause increased Type I interferon response measurable via either qPCR of IFNB, or via an IFNB firefly luciferase report assay. Alternatively, one can incubate compounds with overexpressed NSP15 in cells stimulated with MAVS, MDA-CARD, poly(I:C) or Sendai virus, and then measure for changes in interferon response. In addition, it is prudent to test the effect on the compound on multiple cell lines, as well as to test the assays with a catalytic deficient mutant virus to show the maximal effect of NSP15 inhibition.

Given the conserved nature of NSP15, future experiments could also include testing such inhibitors on NSP15 orthologs such as that of SARS-CoV-1 or murine coronavirus (MHV) NSP15. Establishing NSP15 inhibitors in MHV could also pave the way for mouse models of MHV coronavirus experiments with the compounds.

Finally – future work could use structure function data obtained from crystals to model derivative compounds that have better properties (i.e., compounds with more potent and more positive drug properties), eventually leading to therapeutics.

References

1. Roser, M.; Ritchie, H.; Ortiz-Ospina, E.; Hasell, J., Coronavirus pandemic (COVID-19). *Our world in data* **2020**.
2. Aleem, A.; Kothadia, J., Remdesivir. *StatPearls* **2021**.
3. Ledford, H., Covid antiviral pills: what scientists still want to know. *Nature* **2021**, *599* (7885), 358-359.
4. Garcia-Beltran, W. F.; Lam, E. C.; Denis, K. S.; Nitido, A. D.; Garcia, Z. H.; Hauser, B. M.; Feldman, J.; Pavlovic, M. N.; Gregory, D. J.; Poznansky, M. C., Multiple SARS-CoV-2 variants escape neutralization by vaccine-induced humoral immunity. *Cell* **2021**, *184* (9), 2372-2383. e9.
5. Deng, X.; Hackbart, M.; Mettelman, R. C.; O'Brien, A.; Mielech, A. M.; Yi, G.; Kao, C. C.; Baker, S. C., Coronavirus nonstructural protein 15 mediates evasion of dsRNA sensors and limits apoptosis in macrophages. *Proceedings of the National Academy of Sciences* **2017**, *114* (21), E4251-E4260.
6. Yuen, C.-K.; Lam, J.-Y.; Wong, W.-M.; Mak, L.-F.; Wang, X.; Chu, H.; Cai, J.-P.; Jin, D.-Y.; To, K. K.-W.; Chan, J. F.-W., SARS-CoV-2 nsp13, nsp14, nsp15 and orf6 function as potent interferon antagonists. *Emerging Microbes & Infections* **2020**, 1-29.
7. Shemesh, M.; Aktepe, T. E.; Deerrain, J. M.; McAuley, J. L.; Audsley, M. D.; David, C. T.; Purcell, D. F. J.; Urin, V.; Hartmann, R.; Moseley, G. W.; Mackenzie, J. M.; Schreiber, G.; Harari, D., SARS-CoV-2 suppresses IFN β production mediated by NSP1, 5, 6, 15, ORF6 and ORF7b but does not suppress the effects of added interferon. *PLOS Pathogens* **2021**, *17* (8), e1009800.
8. Ortiz-Alcantara, J.; Bhardwaj, K.; Palaninathan, S.; Frieman, M.; Baric, R.; Kao, C., Small molecule inhibitors of the SARS-CoV NSP15 endoribonuclease. *Virus Adaptation and Treatment* **2010**, *2*, 125-133.
9. Kim, Y.; Wower, J.; Maltseva, N.; Chang, C.; Jedrzejczak, R.; Wilamowski, M.; Kang, S.; Nicolaescu, V.; Randall, G.; Michalska, K., Tipiracil binds to uridine site and inhibits Nsp15 endoribonuclease NendoU from SARS-CoV-2. *Communications biology* **2021**, *4* (1), 1-11.
10. Choi, R.; Zhou, M.; Shek, R.; Wilson, J. W.; Tillery, L.; Craig, J. K.; Salukhe, I. A.; Hickson, S. E.; Kumar, N.; James, R. M., High-throughput screening of the ReFRAME, Pandemic Box, and COVID Box drug repurposing libraries against SARS-CoV-2 nsp15 endoribonuclease to identify small-molecule inhibitors of viral activity. *PloS one* **2021**, *16* (4), e0250019.
11. Fauci, A. S.; Lane, H. C.; Redfield, R. R., Covid-19—navigating the uncharted. *Mass Medical Soc*: 2020.

12. Andersen, K. G.; Rambaut, A.; Lipkin, W. I.; Holmes, E. C.; Garry, R. F., The proximal origin of SARS-CoV-2. *Nature medicine* **2020**, *26* (4), 450-452.
13. Carvalho, T.; Krammer, F.; Iwasaki, A., The first 12 months of COVID-19: a timeline of immunological insights. *Nature Reviews Immunology* **2021**, *21* (4), 245-256.
14. Gorbalenya, A. E.; Baker, S. C.; Baric, R. S.; de Groot, -. R. J.; Drosten, C.; Gulyaeva, A. A.; Haagmans, B.; Lauber, C.; Leontovich, A.; Neuman, B., Coronaviridae Study Group of the International Committee on Taxonomy of Viruses. The species severe acute respiratory syndrome-related coronavirus: classifying 2019-nCoV and naming it SARS-CoV-2. *Nat. Microbiol* **2020**, *5* (4), 536-544.
15. Payne, S., Viruses: From understanding to investigation. Chapter 17: Family Coronaviridae. Elsevier Inc. All rights reserved. Academic Press: 2017.
16. Liu, D. X.; Liang, J. Q.; Fung, T. S., Human coronavirus-229E,-OC43,-NL63, and-HKU1. *Reference Module in Life Sciences* **2020**.
17. Murphy, F. A.; Fauquet, C. M.; Bishop, D. H.; Ghabrial, S. A.; Jarvis, A. W.; Martelli, G. P.; Mayo, M. A.; Summers, M. D., *Virus taxonomy: classification and nomenclature of viruses*. Springer Science & Business Media: 2012; Vol. 10.
18. Heikkinen, T.; Järvinen, A., The common cold. *The Lancet* **2003**, *361* (9351), 51-59.
19. Llanes, A.; Restrepo, C. M.; Caballero, Z.; Rajeev, S.; Kennedy, M. A.; Leonart, R., Betacoronavirus genomes: How genomic information has been used to deal with past outbreaks and the COVID-19 pandemic. **2020**.
20. Fernandes, J. D.; Hinrichs, A. S.; Clawson, H.; Gonzalez, J. N.; Lee, B. T.; Nassar, L. R.; Raney, B. J.; Rosenbloom, K. R.; Nerli, S.; Rao, A. A., The ucsc sars-cov-2 genome browser. *Nature Genetics* **2020**, *52* (10), 991-998.
21. Kim, D.; Lee, J.-Y.; Yang, J.-S.; Kim, J. W.; Kim, V. N.; Chang, H., The architecture of SARS-CoV-2 transcriptome. *Cell* **2020**, *181* (4), 914-921. e10.
22. Gordon, D. E.; Jang, G. M.; Bouhaddou, M.; Xu, J.; Obernier, K.; White, K. M.; O'Meara, M. J.; Rezelj, V. V.; Guo, J. Z.; Swaney, D. L., A SARS-CoV-2 protein interaction map reveals targets for drug repurposing. *Nature* **2020**, *583* (7816), 459-468.
23. Schubert, K.; Karousis, E. D.; Jomaa, A.; Scaiola, A.; Echeverria, B.; Gurzeler, L.-A.; Leibundgut, M.; Thiel, V.; Mühlemann, O.; Ban, N., SARS-CoV-2 Nsp1 binds the ribosomal mRNA channel to inhibit translation. *Nature structural & molecular biology* **2020**, *27* (10), 959-966.
24. Osipiuk, J.; Azizi, S.-A.; Dvorkin, S.; Endres, M.; Jedrzejczak, R.; Jones, K. A.; Kang, S.; Kathayat, R. S.; Kim, Y.; Lisnyak, V. G., Structure of papain-like protease from

SARS-CoV-2 and its complexes with non-covalent inhibitors. *Nature communications* **2021**, *12* (1), 1-9.

25. Sakai, Y.; Kawachi, K.; Terada, Y.; Omori, H.; Matsuura, Y.; Kamitani, W., Two-amino acids change in the nsp4 of SARS coronavirus abolishes viral replication. *Virology* **2017**, *510*, 165-174.

26. Hagemeijer, M. C.; Ulasli, M.; Vonk, A. M.; Reggiori, F.; Rottier, P. J.; de Haan, C. A., Mobility and interactions of coronavirus nonstructural protein 4. *Journal of virology* **2011**, *85* (9), 4572.

27. Lee, J.; Worrall, L. J.; Vuckovic, M.; Rosell, F. I.; Gentile, F.; Ton, A.-T.; Caveney, N. A.; Ban, F.; Cherkasov, A.; Paetzel, M., Crystallographic structure of wild-type SARS-CoV-2 main protease acyl-enzyme intermediate with physiological C-terminal autoprocessing site. *Nature communications* **2020**, *11* (1), 1-9.

28. Angelini, M. M.; Akhlaghpour, M.; Neuman, B. W.; Buchmeier, M. J., Severe acute respiratory syndrome coronavirus nonstructural proteins 3, 4, and 6 induce double-membrane vesicles. *MBio* **2013**, *4* (4).

29. Hillen, H. S.; Kokic, G.; Farnung, L.; Dienemann, C.; Tegunov, D.; Cramer, P., Structure of replicating SARS-CoV-2 polymerase. *Nature* **2020**, *584* (7819), 154-156.

30. Jiang, Y.; Yin, W.; Xu, H. E., RNA-dependent RNA polymerase: Structure, mechanism, and drug discovery for COVID-19. *Biochemical and biophysical research communications* **2021**, *538*, 47-53.

31. Littler, D. R.; Gully, B. S.; Colson, R. N.; Rossjohn, J., Crystal structure of the SARS-CoV-2 non-structural protein 9, Nsp9. *Science* **2020**, *23* (7), 101258.

32. Bouvet, M.; Lugari, A.; Posthuma, C. C.; Zevenhoven, J. C.; Bernard, S.; Betzi, S.; Imbert, I.; Canard, B.; Guillemot, J.-C.; Lécine, P., Coronavirus Nsp10, a critical co-factor for activation of multiple replicative enzymes. *Journal of Biological Chemistry* **2014**, *289* (37), 25783-25796.

33. Decroly, E.; Debarnot, C.; Ferron, F.; Bouvet, M.; Coutard, B.; Imbert, I.; Gluais, L.; Papageorgiou, N.; Sharff, A.; Bricogne, G., Crystal structure and functional analysis of the SARS-coronavirus RNA cap 2'-O-methyltransferase nsp10/nsp16 complex. *PLoS Pathog* **2011**, *7* (5), e1002059.

34. Newman, J. A.; Douangamath, A.; Yazdani, S.; Yosaatmadja, Y.; Aimon, A.; Brandao-Neto, J.; Dunnett, L.; Gorrie-Stone, T.; Skyner, R.; Fearon, D., Structure, Mechanism and Crystallographic fragment screening of the SARS-CoV-2 NSP13 helicase. *bioRxiv* **2021**.

35. Adedeji, A. O.; Marchand, B.; Te Velthuis, A. J.; Snijder, E. J.; Weiss, S.; Eoff, R. L.; Singh, K.; Sarafianos, S. G., Mechanism of nucleic acid unwinding by SARS-CoV helicase. *PLoS one* **2012**, *7* (5), e36521.
36. Shannon, A.; Le, N. T.-T.; Selisko, B.; Eydoux, C.; Alvarez, K.; Guillemot, J.-C.; Decroly, E.; Peersen, O.; Ferron, F.; Canard, B., Remdesivir and SARS-CoV-2: Structural requirements at both nsp12 RdRp and nsp14 Exonuclease active-sites. *Antiviral research* **2020**, *178*, 104793.
37. Lin, S.; Chen, H.; Chen, Z.; Yang, F.; Ye, F.; Zheng, Y.; Yang, J.; Lin, X.; Sun, H.; Wang, L., Crystal structure of SARS-CoV-2 nsp10 bound to nsp14-ExoN domain reveals an exoribonuclease with both structural and functional integrity. *Nucleic acids research* **2021**, *49* (9), 5382-5392.
38. Pillon, M. C.; Frazier, M. N.; Dillard, L.; Williams, J. G.; Kocaman, S.; Krahn, J. M.; Perera, L.; Hayne, C. K.; Gordon, J.; Stewart, Z. D., Cryo-EM Structures of the SARS-CoV-2 Endoribonuclease Nsp15. *BioRxiv* **2020**.
39. Hackbart, M.; Deng, X.; Baker, S. C., Coronavirus endoribonuclease targets viral polyuridine sequences to evade activating host sensors. *Proceedings of the National Academy of Sciences* **2020**, *117* (14), 8094-8103.
40. Kindler, E.; Gil-Cruz, C.; Spanier, J.; Li, Y.; Wilhelm, J.; Rabouw, H. H.; Züst, R.; Hwang, M.; V'kovski, P.; Stalder, H., Early endonuclease-mediated evasion of RNA sensing ensures efficient coronavirus replication. *PLoS pathogens* **2017**, *13* (2), e1006195.
41. Ke, Z.; Oton, J.; Qu, K.; Cortese, M.; Zila, V.; McKeane, L.; Nakane, T.; Zivanov, J.; Neufeldt, C. J.; Cerikan, B., Structures and distributions of SARS-CoV-2 spike proteins on intact virions. *Nature* **2020**, *588* (7838), 498-502.
42. Schoeman, D.; Fielding, B. C., Coronavirus envelope protein: current knowledge. *Virology journal* **2019**, *16* (1), 1-22.
43. Armstrong, J.; Niemann, H.; Smeekens, S.; Rottier, P.; Warren, G., Sequence and topology of a model intracellular membrane protein, E1 glycoprotein, from a coronavirus. *Nature* **1984**, *308* (5961), 751-752.
44. Neuman, B. W.; Kiss, G.; Kunding, A. H.; Bhella, D.; Baksh, M. F.; Connelly, S.; Droese, B.; Klaus, J. P.; Makino, S.; Sawicki, S. G., A structural analysis of M protein in coronavirus assembly and morphology. *Journal of structural biology* **2011**, *174* (1), 11-22.
45. Masters, P. S.; Sturman, L. S., Background paper functions of the coronavirus nucleocapsid protein. *Coronaviruses and their Diseases* **1990**, 235-238.
46. Cheng, Y.-W.; Chao, T.-L.; Li, C.-L.; Chiu, M.-F.; Kao, H.-C.; Wang, S.-H.; Pang, Y.-H.; Lin, C.-H.; Tsai, Y.-M.; Lee, W.-H., Furin inhibitors block SARS-CoV-2 spike protein

cleavage to suppress virus production and cytopathic effects. *Cell reports* **2020**, *33* (2), 108254.

47. Hoffmann, M.; Kleine-Weber, H.; Schroeder, S.; Krüger, N.; Herrler, T.; Erichsen, S.; Schiergens, T. S.; Herrler, G.; Wu, N.-H.; Nitsche, A., SARS-CoV-2 cell entry depends on ACE2 and TMPRSS2 and is blocked by a clinically proven protease inhibitor. *cell* **2020**, *181* (2), 271-280. e8.

48. Chan, J. F.-W.; Kok, K.-H.; Zhu, Z.; Chu, H.; To, K. K.-W.; Yuan, S.; Yuen, K.-Y., Genomic characterization of the 2019 novel human-pathogenic coronavirus isolated from a patient with atypical pneumonia after visiting Wuhan. *Emerging microbes & infections* **2020**, *9* (1), 221-236.

49. Scheim, D., From cold to killer: how SARS-CoV-2 evolved without hemagglutinin esterase to agglutinate, then clot blood cells in pulmonary and systemic microvasculature. *Then Clot Blood Cells in Pulmonary and Systemic Microvasculature (October 6, 2020)* **2020**.

50. Lei, X.; Dong, X.; Ma, R.; Wang, W.; Xiao, X.; Tian, Z.; Wang, C.; Wang, Y.; Li, L.; Ren, L.; Guo, F.; Zhao, Z.; Zhou, Z.; Xiang, Z.; Wang, J., Activation and evasion of type I interferon responses by SARS-CoV-2. *Nature Communications* **2020**, *11* (1), 3810.

51. Snijder, E. J.; Limpens, R. W.; De Wilde, A. H.; De Jong, A. W.; Zevenhoven-Dobbe, J. C.; Maier, H. J.; Faas, F. F.; Koster, A. J.; Bárcena, M., A unifying structural and functional model of the coronavirus replication organelle: tracking down RNA synthesis. *Plos Biology* **2020**, *18* (6), e3000715.

52. Fehr, A. R.; Perlman, S., Coronaviruses: an overview of their replication and pathogenesis. In *Coronaviruses*, Springer: 2015; pp 1-23.

53. Sola, I.; Almazán, F.; Zúñiga, S.; Enjuanes, L., Continuous and Discontinuous RNA Synthesis in Coronaviruses. *Annu Rev Virol* **2015**, *2* (1), 265-288.

54. Hofmann, M. A.; Brain, D., The 5'end of coronavirus minus-strand RNAs contains a short poly (U) tract. *Journal of virology* **1991**, *65* (11), 6331-6333.

55. Snijder, E. J.; Bredenbeek, P. J.; Dobbe, J. C.; Thiel, V.; Ziebuhr, J.; Poon, L. L.; Guan, Y.; Rozanov, M.; Spaan, W. J.; Gorbalenya, A. E., Unique and conserved features of genome and proteome of SARS-coronavirus, an early split-off from the coronavirus group 2 lineage. *Journal of molecular biology* **2003**, *331* (5), 991-1004.

56. Renzi, F.; Caffarelli, E.; Laneve, P.; Bozzoni, I.; Brunori, M.; Vallone, B., The structure of the endoribonuclease XendoU: From small nucleolar RNA processing to severe acute respiratory syndrome coronavirus replication. *Proceedings of the National Academy of Sciences* **2006**, *103* (33), 12365-12370.

57. Xu, X.; Zhai, Y.; Sun, F.; Lou, Z.; Su, D.; Xu, Y.; Zhang, R.; Joachimiak, A.; Zhang, X. C.; Bartlam, M.; Rao, Z., New antiviral target revealed by the hexameric structure of mouse hepatitis virus nonstructural protein nsp15. *Journal of virology* **2006**, *80* (16), 7909-7917.
58. Bhardwaj, K.; Guarino, L.; Kao, C. C., The severe acute respiratory syndrome coronavirus Nsp15 protein is an endoribonuclease that prefers manganese as a cofactor. *Journal of virology* **2004**, *78* (22), 12218-12224.
59. Kim, Y.; Jedrzejczak, R.; Maltseva, N. I.; Wilamowski, M.; Endres, M.; Godzik, A.; Michalska, K.; Joachimiak, A., Crystal structure of Nsp15 endoribonuclease NendoU from SARS-CoV-2. *Protein Science* **2020**.
60. Pillon, M. C.; Frazier, M. N.; Dillard, L. B.; Williams, J. G.; Kocaman, S.; Krahn, J. M.; Perera, L.; Hayne, C. K.; Gordon, J.; Stewart, Z. D., Cryo-EM structures of the SARS-CoV-2 endoribonuclease Nsp15 reveal insight into nuclease specificity and dynamics. *Nature communications* **2021**, *12* (1), 1-12.
61. Ivanov, K. A.; Hertzog, T.; Rozanov, M.; Bayer, S.; Thiel, V.; Gorbalenya, A. E.; Ziebuhr, J., Major genetic marker of nidoviruses encodes a replicative endoribonuclease. *Proceedings of the National Academy of Sciences* **2004**, *101* (34), 12694-12699.
62. Bhardwaj, K.; Sun, J.; Holzenburg, A.; Guarino, L. A.; Kao, C. C., RNA recognition and cleavage by the SARS coronavirus endoribonuclease. *Journal of molecular biology* **2006**, *361* (2), 243-256.
63. Guarino, L. A.; Bhardwaj, K.; Dong, W.; Sun, J.; Holzenburg, A.; Kao, C., Mutational analysis of the SARS virus Nsp15 endoribonuclease: identification of residues affecting hexamer formation. *Journal of molecular biology* **2005**, *353* (5), 1106-1117.
64. Joseph, J. S.; Saikatendu, K. S.; Subramanian, V.; Neuman, B. W.; Buchmeier, M. J.; Stevens, R. C.; Kuhn, P., Crystal structure of a monomeric form of severe acute respiratory syndrome coronavirus endonuclease nsp15 suggests a role for hexamerization as an allosteric switch. *Journal of virology* **2007**, *81* (12), 6700-6708.
65. Lee, A. J.; Ashkar, A. A., The dual nature of type I and type II interferons. *Frontiers in immunology* **2018**, *9*, 2061.
66. Wack, A.; Terczyńska-Dyla, E.; Hartmann, R., Guarding the frontiers: the biology of type III interferons. *Nature immunology* **2015**, *16* (8), 802-809.
67. Jefferies, C. A., Regulating IRFs in IFN driven disease. *Frontiers in immunology* **2019**, *10*, 325.
68. Schroder, K.; Hertzog, P. J.; Ravasi, T.; Hume, D. A., Interferon- γ : an overview of signals, mechanisms and functions. *Journal of leukocyte biology* **2004**, *75* (2), 163-189.

69. Green, D. S.; Young, H. A.; Valencia, J. C., Current prospects of type II interferon γ signaling and autoimmunity. *Journal of Biological Chemistry* **2017**, *292* (34), 13925-13933.
70. Park, A.; Iwasaki, A., Type I and Type III Interferons—Induction, Signaling, Evasion, and Application to Combat COVID-19. *Cell Host & Microbe* **2020**.
71. Morgan Brisse, H. L., Comparative structure and function analysis of the RIG-I-like receptors: RIG-I and MDA5. *Frontiers in immunology* **2019**, *10*.
72. David, R. Y. S.; Combredet, C.; Najburg, V.; Millot, G. A.; Beauclair, G.; Schwikowski, B.; Léger, T.; Camadro, J.-M.; Jacob, Y.; Bellalou, J., LGP2 binds to PACT to regulate RIG-I—and MDA5-mediated antiviral responses. *Science Signaling* **2019**, *12* (601), eaar3993.
73. Junior, A. G. D.; Sampaio, N. G.; Rehwinkel, J., A balancing act: MDA5 in antiviral immunity and autoinflammation. *Trends in microbiology* **2019**, *27* (1), 75-85.
74. Uchikawa, E.; Lethier, M.; Malet, H.; Brunel, J.; Gerlier, D.; Cusack, S., Structural analysis of dsRNA binding to anti-viral pattern recognition receptors LGP2 and MDA5. *Molecular cell* **2016**, *62* (4), 586-602.
75. Kawasaki, T.; Kawai, T., Toll-like receptor signaling pathways. *Frontiers in immunology* **2014**, *5*, 461.
76. Liu, T.; Zhang, L.; Joo, D.; Sun, S.-C., NF- κ B signaling in inflammation. *Signal transduction and targeted therapy* **2017**, *2* (1), 1-9.
77. Garcia, M.; Meurs, E.; Esteban, M., The dsRNA protein kinase PKR: virus and cell control. *Biochimie* **2007**, *89* (6-7), 799-811.
78. Drappier, M.; Michiels, T., Inhibition of the OAS/RNase L pathway by viruses. *Current opinion in virology* **2015**, *15*, 19-26.
79. Cooper, D. A.; Banerjee, S.; Chakrabarti, A.; García-Sastre, A.; Hesselberth, J. R.; Silverman, R. H.; Barton, D. J., RNase L targets distinct sites in influenza A virus RNAs. *Journal of virology* **2015**, *89* (5), 2764-2776.
80. Athmer, J.; Fehr, A. R.; Grunewald, M.; Smith, E. C.; Denison, M. R.; Perlman, S., In situ tagged nsp15 reveals interactions with coronavirus replication/transcription complex-associated proteins. *MBio* **2017**, *8* (1).
81. Ancar, R.; Li, Y.; Kindler, E.; Cooper, D. A.; Ransom, M.; Thiel, V.; Weiss, S. R.; Hesselberth, J. R.; Barton, D. J., Physiologic RNA targets and refined sequence specificity of coronavirus EndoU. *RNA* **2020**, *26* (12), 1976-1999.

82. Zheng, A.; Shi, Y.; Shen, Z.; Wang, G.; Shi, J.; Xiong, Q.; Fang, L.; Xiao, S.; Fu, Z. F.; Peng, G., Insight into the evolution of nidovirus endoribonuclease based on the finding that nsp15 from porcine Deltacoronavirus functions as a dimer. *Journal of Biological Chemistry* **2018**, 293 (31), 12054-12067.
83. Liu, X.; Fang, P.; Fang, L.; Hong, Y.; Zhu, X.; Wang, D.; Peng, G.; Xiao, S., Porcine deltacoronavirus nsp15 antagonizes interferon- β production independently of its endoribonuclease activity. *Molecular immunology* **2019**, 114, 100-107.
84. Bhardwaj, K.; Liu, P.; Leibowitz, J. L.; Kao, C. C., The coronavirus endoribonuclease Nsp15 interacts with retinoblastoma tumor suppressor protein. *Journal of virology* **2012**, 86 (8), 4294-4304.
85. Dahiya, A.; Gavin Mark, R.; Luo Robin, X.; Dean Douglas, C., Role of the LXCXE Binding Site in Rb Function. *Molecular and Cellular Biology* **2000**, 20 (18), 6799-6805.
86. Lei, Y.; Moore, C. B.; Liesman, R. M.; O'Connor, B. P.; Bergstralh, D. T.; Chen, Z. J.; Pickles, R. J.; Ting, J. P. Y., MAVS-mediated apoptosis and its inhibition by viral proteins. *PloS one* **2009**, 4 (5), e5466-e5466.
87. Benedict, C. A.; Norris, P. S.; Ware, C. F., To kill or be killed: viral evasion of apoptosis. *Nature Immunology* **2002**, 3 (11), 1013-1018.
88. Kang, H.; Bhardwaj, K.; Li, Y.; Palaninathan, S.; Sacchettini, J.; Guarino, L.; Leibowitz, J. L.; Kao, C. C., Biochemical and genetic analyses of murine hepatitis virus Nsp15 endoribonuclease. *J Virol* **2007**, 81 (24), 13587-97.
89. Comar, C. E. Interactions of Highly Pathogenic Human Coronaviruses with dsRNA-Induced Innate Immune Pathways. University of Pennsylvania, 2021.
90. Xia, H.; Cao, Z.; Xie, X.; Zhang, X.; Chen, J. Y.-C.; Wang, H.; Menachery, V. D.; Rajsbaum, R.; Shi, P.-Y., Evasion of type I interferon by SARS-CoV-2. *Cell reports* **2020**, 33 (1), 108234.
91. Kumar, A.; Ishida, R.; Strilets, T.; Cole, J.; Lopez-Orozco, J.; Fayad, N.; Felix-Lopez, A.; Elaish, M.; Evseev, D.; Magor, K. E.; Mahal, L. K.; Nagata, L. P.; Evans, D. H.; Hobman, T. C.; Gallagher, T., SARS-CoV-2 Nonstructural Protein 1 Inhibits the Interferon Response by Causing Depletion of Key Host Signaling Factors. *Journal of Virology* **2021**, 95 (13), e00266-21.
92. Hayn, M.; Hirschenberger, M.; Koepke, L.; Nchioua, R.; Straub, J. H.; Klute, S.; Hunszinger, V.; Zech, F.; Prelli Bozzo, C.; Aftab, W.; Christensen, M. H.; Conzelmann, C.; Müller, J. A.; Srinivasachar Badarinarayan, S.; Stürzel, C. M.; Forne, I.; Stenger, S.; Conzelmann, K.-K.; Münch, J.; Schmidt, F. I.; Sauter, D.; Imhof, A.; Kirchhoff, F.; Sparrer, K. M. J., Systematic functional analysis of SARS-CoV-2 proteins uncovers viral innate immune antagonists and remaining vulnerabilities. *Cell Reports* **2021**, 35 (7), 109126.

93. Li, Y.; Renner, D. M.; Comar, C. E.; Whelan, J. N.; Reyes, H. M.; Cardenas-Diaz, F. L.; Truitt, R.; Tan, L. H.; Dong, B.; Alysandratos, K. D.; Huang, J.; Palmer, J. N.; Adappa, N. D.; Kohanski, M. A.; Kotton, D. N.; Silverman, R. H.; Yang, W.; Morrissey, E. E.; Cohen, N. A.; Weiss, S. R., SARS-CoV-2 induces double-stranded RNA-mediated innate immune responses in respiratory epithelial-derived cells and cardiomyocytes. *Proceedings of the National Academy of Sciences* **2021**, *118* (16), e2022643118.
94. Khan, R. J.; Jha, R. K.; Singh, E.; Jain, M.; Amera, G. M.; Singh, R. P.; Muthukumar, J.; Singh, A. K., Identification of promising antiviral drug candidates against non-structural protein 15 (NSP15) from SARS-CoV-2: an in silico assisted drug-repurposing study. *Journal of Biomolecular Structure and Dynamics* **2022**, *40* (1), 438-448.
95. Sinha, S. K.; Shakya, A.; Prasad, S. K.; Singh, S.; Gurav, N. S.; Prasad, R. S.; Gurav, S. S., An in-silico evaluation of different Saikosaponins for their potency against SARS-CoV-2 using NSP15 and fusion spike glycoprotein as targets. *Journal of Biomolecular Structure and Dynamics* **2021**, *39* (9), 3244-3255.
96. Sharma, J.; Bhardwaj, V. K.; Singh, R.; Rajendran, V.; Purohit, R.; Kumar, S., An in-silico evaluation of different bioactive molecules of tea for their inhibition potency against non structural protein-15 of SARS-CoV-2. *Food chemistry* **2021**, *346*, 128933.
97. Stevaert, A.; Krasniqi, B.; Van Loy, B.; Nguyen, T.; Thomas, J.; Vandeput, J.; Jochmans, D.; Thiel, V.; Dijkman, R.; Dehaen, W.; Voet, A.; Naesens, L., Betulonic Acid Derivatives Interfering with Human Coronavirus 229E Replication via the nsp15 Endoribonuclease. *Journal of Medicinal Chemistry* **2021**, *64* (9), 5632-5644.
98. Canal, B.; Fujisawa, R.; McClure, A. W.; Deegan, T.; Wu, M.; Ulferts, R.; Weissmann, F.; Drury, L. S.; Bertolin, A. P.; Zeng, J.; Beale, R.; Howell, M.; Labib, K.; Diffley, J. F. X., Identifying SARS-CoV-2 Antiviral Compounds by Screening for Small Molecule Inhibitors of Nsp15 Endoribonuclease. *bioRxiv* **2021**, 2021.04.07.438811.
99. Wang, L.; Saarela, J.; Poque, S.; Valkonen, J. P., Development of FRET-based high-throughput screening for viral RNase III inhibitors. *Molecular plant pathology* **2020**, *21* (7), 961-974.
100. Parniak, M. A.; Min, K.-L.; Budihis, S. R.; Le Grice, S. F.; Beutler, J. A., A fluorescence-based high-throughput screening assay for inhibitors of human immunodeficiency virus-1 reverse transcriptase-associated ribonuclease H activity. *Analytical biochemistry* **2003**, *322* (1), 33-39.
101. White, R.; Saxty, B.; Large, J.; Kettleborough, C. A.; Jackson, A. P., Identification of small-molecule inhibitors of the ribonuclease H2 enzyme. *Journal of biomolecular screening* **2013**, *18* (5), 610-620.
102. Brooks, H. B.; Geeganage, S.; Kahl, S. D.; Montrose, C.; Sittampalam, S.; Smith, M. C.; Weidner, J. R., Basics of enzymatic assays for HTS. *Assay Guidance Manual [Internet]* **2012**.

103. Lloyd, M. D., High-Throughput Screening for the Discovery of Enzyme Inhibitors. *Journal of Medicinal Chemistry* **2020**, 63 (19), 10742-10772.
104. Kim, Y.; Jedrzejczak, R.; Maltseva, N. I.; Wilamowski, M.; Endres, M.; Godzik, A.; Michalska, K.; Joachimiak, A., Crystal structure of Nsp15 endoribonuclease NendoU from SARS-CoV-2. *Protein Science* **2020**, 29 (7), 1596-1605.
105. Nedialkova, D. D.; Ulferts, R.; Van Den Born, E.; Lauber, C.; Gorbalenya, A. E.; Ziebuhr, J.; Snijder, E. J., Biochemical characterization of arterivirus nonstructural protein 11 reveals the nidovirus-wide conservation of a replicative endoribonuclease. *Journal of virology* **2009**, 83 (11), 5671.
106. Johnston, P. A., Redox cycling compounds generate H₂O₂ in HTS buffers containing strong reducing reagents--real hits or promiscuous artifacts? *Curr Opin Chem Biol* **2011**, 15 (1), 174-182.
107. Karakuzu, O.; Cruz, M. R.; Liu, Y.; Garsin, D. A., Amplex Red Assay for Measuring Hydrogen Peroxide Production from *Caenorhabditis elegans*. *Bio Protoc* **2019**, 9 (21), e3409.
108. Osada, N.; Kohara, A.; Yamaji, T.; Hirayama, N.; Kasai, F.; Sekizuka, T.; Kuroda, M.; Hanada, K., The Genome Landscape of the African Green Monkey Kidney-Derived Vero Cell Line. *DNA Research* **2014**, 21 (6), 673-683.
109. Canal, B.; Fujisawa, R.; McClure, A. W.; Deegan, T. D.; Wu, M.; Ulferts, R.; Weissmann, F.; Drury, L. S.; Bertolin, A. P.; Zeng, J.; Beale, R.; Howell, M.; Labib, K.; Diffley, J. F. X., Identifying SARS-CoV-2 antiviral compounds by screening for small molecule inhibitors of nsp15 endoribonuclease. *The Biochemical journal* **2021**, 478 (13), 2465-2479.
110. Benet, L. Z.; Hosey, C. M.; Ursu, O.; Oprea, T. I., BDDCS, the Rule of 5 and drugability. *Adv Drug Deliv Rev* **2016**, 101, 89-98.
111. Press, B.; Di Grandi, D., Permeability for intestinal absorption: Caco-2 assay and related issues. *Current drug metabolism* **2008**, 9 (9), 893-900.
112. Elmeliegy, M.; Vourvahis, M.; Guo, C.; Wang, D. D., Effect of P-glycoprotein (P-gp) inducers on exposure of P-gp substrates: review of clinical drug-drug interaction studies. *Clinical pharmacokinetics* **2020**, 59 (6), 699-714.
113. Tejs, S., The Ames test: a methodological short review. *Environmental Biotechnology* **2008**, 4, 7-14.
114. Kalyaanamoorthy, S.; Barakat, K. H., Development of safe drugs: the hERG challenge. *Medicinal research reviews* **2018**, 38 (2), 525-555.

115. Trainor, G. L., The importance of plasma protein binding in drug discovery. *Expert Opin Drug Discov* **2007**, 2 (1), 51-64.
116. Frazier, Meredith N.; Dillard, Lucas B.; Krahn, Juno M.; Perera, L.; Williams, Jason G.; Wilson, Isha M.; Stewart, Zachary D.; Pillon, Monica C.; Deterding, Leesa J.; Borgnia, Mario J.; Stanley, Robin E., Characterization of SARS2 Nsp15 nuclease activity reveals it's mad about U. *Nucleic Acids Research* **2021**.
117. Saramago, M.; Costa, V. G.; Souza, C. S.; Bária, C.; Domingues, S.; Viegas, S. C.; Lousa, D.; Soares, C. M.; Arraiano, C. M.; Matos, R. G., The nsp15 Nuclease as a Good Target to Combat SARS-CoV-2: Mechanism of Action and Its Inactivation with FDA-Approved Drugs. *Microorganisms* **2022**, 10 (2), 342.
118. Chakravarthi, S.; Jessop, C. E.; Bulleid, N. J., The role of glutathione in disulphide bond formation and endoplasmic-reticulum-generated oxidative stress. *EMBO Rep* **2006**, 7 (3), 271-275.
119. Glorieux, C.; Sandoval, J. M.; Dejeans, N.; Ameye, G.; Poirel, H. A.; Verrax, J.; Calderon, P. B., Overexpression of NAD (P) H: quinone oxidoreductase 1 (NQO1) and genomic gain of the NQO1 locus modulates breast cancer cell sensitivity to quinones. *Life sciences* **2016**, 145, 57-65.
120. Cao, J.; Forrest, J. C.; Zhang, X., A screen of the NIH Clinical Collection small molecule library identifies potential anti-coronavirus drugs. *Antiviral Res* **2015**, 114, 1-10.
121. Scott, J. E.; Williams, K. P., Validating identity, mass purity and enzymatic purity of enzyme preparations. *Assay Guidance Manual [Internet]* **2012**.
122. Taylor, K. B., Slow and tight inhibition. *Enzyme Kinetics and Mechanisms* **2002**, 122-146.
123. Salaün, J., Cyclopropane derivatives and their diverse biological activities. *Small ring compounds in organic synthesis VI* **2000**, 1-67.
124. Talele, T. T., The "Cyclopropyl Fragment" is a Versatile Player that Frequently Appears in Preclinical/Clinical Drug Molecules. *Journal of Medicinal Chemistry* **2016**, 59 (19), 8712-8756.
125. Ji Ram, V.; Sethi, A.; Nath, M.; Pratap, R., Chapter 5 - Five-Membered Heterocycles. In *The Chemistry of Heterocycles*, Ji Ram, V.; Sethi, A.; Nath, M.; Pratap, R., Eds. Elsevier: 2019; pp 149-478.
126. Wu, Y.-J., Chapter 5.5 - Five-Membered Ring Systems: With N and S Atom. In *Progress in Heterocyclic Chemistry*, Gribble, G. W.; Joule, J. A., Eds. Elsevier: 2016; Vol. 28, pp 317-339.

127. Biernasiuk, A.; Banasiewicz, A.; Maslyk, M.; Martyna, A.; Janeczko, M.; Baranowska-Łączkowska, A.; Malm, A.; Łączkowski, K. Z., Synthesis and Physicochemical Characterization of Novel Dicyclopropyl-Thiazole Compounds as Nontoxic and Promising Antifungals. *Materials (Basel)* **2021**, *14* (13), 3500.
128. Malik, E. M.; Müller, C. E., Anthraquinones As Pharmacological Tools and Drugs. *Med Res Rev* **2016**, *36* (4), 705-48.
129. Thorn, C. F.; Oshiro, C.; Marsh, S.; Hernandez-Boussard, T.; McLeod, H.; Klein, T. E.; Altman, R. B., Doxorubicin pathways: pharmacodynamics and adverse effects. *Pharmacogenet Genomics* **2011**, *21* (7), 440-446.
130. Baell, J. B.; Holloway, G. A., New substructure filters for removal of pan assay interference compounds (PAINS) from screening libraries and for their exclusion in bioassays. *Journal of medicinal chemistry* **2010**, *53* (7), 2719-2740.
131. Talele, T. T.; Arora, P.; Kulkarni, S. S.; Patel, M. R.; Singh, S.; Chudayeu, M.; Kaushik-Basu, N., Structure-based virtual screening, synthesis and SAR of novel inhibitors of hepatitis C virus NS5B polymerase. *Bioorganic & Medicinal Chemistry* **2010**, *18* (13), 4630-4638.
132. Tomašić, T.; Peterlin Mašič, L., Rhodanine as a scaffold in drug discovery: a critical review of its biological activities and mechanisms of target modulation. *Expert Opin Drug Discov* **2012**, *7* (7), 549-560.
133. Iyer, S.; Sam, F. S.; DiPrimio, N.; Preston, G.; Verheijen, J.; Murthy, K.; Parton, Z.; Tsang, H.; Lao, J.; Morava, E., Repurposing the aldose reductase inhibitor and diabetic neuropathy drug epalrestat for the congenital disorder of glycosylation PMM2-CDG. *Disease models & mechanisms* **2019**, *12* (11), dmm040584.
134. Frlan, R.; Kovac, A.; Blanot, D.; Gobec, S.; Pecar, S.; Obreza, A., Design and synthesis of novel N-benzylidenesulfonohydrazide inhibitors of MurC and MurD as potential antibacterial agents. *Molecules* **2008**, *13* (1), 11-30.
135. Lockhart, J. D.; Simmons, H. E., HEXACHLOROPHENE DECISIONS AT THE FDA. *Pediatrics* **1973**, *51* (2), 430-434.
136. Chow, C.; Chow, A. Y.; Downie, R. H.; Buttar, H. S., Percutaneous absorption of hexachlorophene in rats, guinea pigs and pigs. *Toxicology* **1978**, *9* (1-2), 147-54.
137. Jeon, S.; Ko, M.; Lee, J.; Choi, I.; Byun Soo, Y.; Park, S.; Shum, D.; Kim, S., Identification of Antiviral Drug Candidates against SARS-CoV-2 from FDA-Approved Drugs. *Antimicrobial Agents and Chemotherapy* **64** (7), e00819-20.
138. Liu, Y.-C.; Huang, V.; Chao, T.-C.; Hsiao, C.-D.; Lin, A.; Chang, M.-F.; Chow, L.-P., Screening of drugs by FRET analysis identifies inhibitors of SARS-CoV 3CL protease. *Biochemical and biophysical research communications* **2005**, *333* (1), 194-199.

139. Itaba, N.; Matsumi, Y.; Okinaka, K.; Ashla, A. A.; Kono, Y.; Osaki, M.; Morimoto, M.; Sugiyama, N.; Ohashi, K.; Okano, T.; Shiota, G., Human mesenchymal stem cell-engineered hepatic cell sheets accelerate liver regeneration in mice. *Scientific reports* **2015**, *5*, 16169-16169.
140. Deacon, S. W.; Beeser, A.; Fukui, J. A.; Rennefahrt, U. E.; Myers, C.; Chernoff, J.; Peterson, J. R., An isoform-selective, small-molecule inhibitor targets the autoregulatory mechanism of p21-activated kinase. *Chem Biol* **2008**, *15* (4), 322-31.
141. Dummler, B.; Ohshiro, K.; Kumar, R.; Field, J., Pak protein kinases and their role in cancer. *Cancer Metastasis Rev* **2009**, *28* (1-2), 51-63.
142. Montero, D.; Tachibana, C.; Rahr Winther, J.; Appenzeller-Herzog, C., Intracellular glutathione pools are heterogeneously concentrated. *Redox Biol* **2013**, *1* (1), 508-513.
143. Pajouhesh, H.; Lenz, G. R., Medicinal chemical properties of successful central nervous system drugs. *NeuroRx* **2005**, *2* (4), 541-553.
144. Sutanto, F.; Konstantinidou, M.; Dömling, A., Covalent inhibitors: a rational approach to drug discovery. *RSC medicinal chemistry* **2020**, *11* (8), 876-884.
145. Mahase, E., Covid-19: Pfizer's paxlovid is 89% effective in patients at risk of serious illness, company reports. British Medical Journal Publishing Group: 2021.
146. Senkane, K.; Vinogradova, E. V.; Suciu, R. M.; Crowley, V. M.; Zaro, B. W.; Bradshaw, J. M.; Brameld, K. A.; Cravatt, B. F., The Proteome-Wide Potential for Reversible Covalency at Cysteine. *Angewandte Chemie* **2019**, *131* (33), 11507-11511.
147. Administration, U. S. F. a. D. Emergency Use Authorization. <https://www.fda.gov/emergency-preparedness-and-response/mcm-legal-regulatory-and-policy-framework/emergency-use-authorization> (accessed June 13).
148. Owen, D. R.; Allerton, C. M.; Anderson, A. S.; Aschenbrenner, L.; Avery, M.; Berritt, S.; Boras, B.; Cardin, R. D.; Carlo, A.; Coffman, K. J., An oral SARS-CoV-2 Mpro inhibitor clinical candidate for the treatment of COVID-19. *Science* **2021**, *374* (6575), 1586-1593.
149. Kabinger, F.; Stiller, C.; Schmitzová, J.; Dienemann, C.; Kobic, G.; Hillen, H. S.; Höbartner, C.; Cramer, P., Mechanism of molnupiravir-induced SARS-CoV-2 mutagenesis. *Nature structural & molecular biology* **2021**, *28* (9), 740-746.
150. Sheahan, T. P.; Sims, A. C.; Zhou, S.; Graham, R. L.; Pruijssers, A. J.; Agostini, M. L.; Leist, S. R.; Schäfer, A.; Dinnon III, K. H.; Stevens, L. J., An orally bioavailable broad-spectrum antiviral inhibits SARS-CoV-2 in human airway epithelial cell cultures and multiple coronaviruses in mice. *Sci Transl Med* **2020**, *12* (541), eabb5883.

151. Siegel, D.; Hui, H. C.; Doerffler, E.; Clarke, M. O.; Chun, K.; Zhang, L.; Neville, S.; Carra, E.; Lew, W.; Ross, B., Discovery and Synthesis of a Phosphoramidate Prodrug of a Pyrrolo [2, 1-f][triazin-4-amino] Adenine C-Nucleoside (GS-5734) for the Treatment of Ebola and Emerging Viruses. ACS Publications: 2017.
152. Slanina, H.; Madhugiri, R.; Bylapudi, G.; Schultheiß, K.; Karl, N.; Gulyaeva, A.; Gorbalenya, A. E.; Linne, U.; Ziebuhr, J., Coronavirus replication–transcription complex: Vital and selective NMPylation of a conserved site in nsp9 by the NiRAN-RdRp subunit. *Proceedings of the National Academy of Sciences* **2021**, *118* (6).
153. Makiyama, K.; Hazawa, M.; Kobayashi, A.; Lim, K.; Voon, D. C.; Wong, R. W., NSP9 of SARS-CoV-2 attenuates nuclear transport by hampering nucleoporin 62 dynamics and functions in host cells. *Biochemical and biophysical research communications* **2022**, *586*, 137-142.
154. Littler, D. R.; Liu, M.; McAuley, J. L.; Lowery, S. A.; Illing, P. T.; Gully, B. S.; Purcell, A. W.; Chandrashekar, I. R.; Perlman, S.; Purcell, D. F., A natural product compound inhibits coronaviral replication in vitro by binding to the conserved Nsp9 SARS-CoV-2 protein. *Journal of Biological Chemistry* **2021**, *297* (6).
155. Diffley, J. F., Author's overview: identifying SARS-CoV-2 antiviral compounds. *Biochemical Journal* **2021**, *478* (13), 2533-2535.
156. Zeng, J.; Weissmann, F.; Bertolin, A. P.; Posse, V.; Canal, B.; Ulferts, R.; Wu, M.; Harvey, R.; Hussain, S.; Milligan, J. C., Identifying SARS-CoV-2 antiviral compounds by screening for small molecule inhibitors of nsp13 helicase. *Biochemical Journal* **2021**, *478* (13), 2405-2423.
157. Hoffman, R. L.; Kania, R. S.; Brothers, M. A.; Davies, J. F.; Ferre, R. A.; Gajiwala, K. S.; He, M.; Hogan, R. J.; Kozminski, K.; Li, L. Y., Discovery of ketone-based covalent inhibitors of coronavirus 3CL proteases for the potential therapeutic treatment of COVID-19. *Journal of medicinal chemistry* **2020**, *63* (21), 12725-12747.
158. Review, C. F. D. E. a. R. C. Emergency Use Authorization (EUA) for Paxlovid (nirmatrelvir tablets co-packaged with ritonavir tablets) <https://www.fda.gov/media/155194/download>.
159. Agency, E. M. *Use of molnupiravir for the treatment of COVID-19*; 2022.
160. Pruijssers, A. J.; George, A. S.; Schäfer, A.; Leist, S. R.; Gralinski, L. E.; Dinnon III, K. H.; Yount, B. L.; Agostini, M. L.; Stevens, L. J.; Chappell, J. D., Remdesivir inhibits SARS-CoV-2 in human lung cells and chimeric SARS-CoV expressing the SARS-CoV-2 RNA polymerase in mice. *Cell reports* **2020**, *32* (3), 107940.
161. Wang, M.; Cao, R.; Zhang, L.; Yang, X.; Liu, J.; Xu, M.; Shi, Z.; Hu, Z.; Zhong, W.; Xiao, G., Remdesivir and chloroquine effectively inhibit the recently emerged novel coronavirus (2019-nCoV) in vitro. *Cell research* **2020**, *30* (3), 269-271.

162. Ecker, D. J.; Vickers, T. A.; Hanecak, R.; Diver, V.; Anderson, K., Rational screening of oligonucleotide combinatorial libraries for drug discovery. *Nucleic acids research* **1993**, *21* (8), 1853-1856.
163. Jockusch, S.; Tao, C.; Li, X.; Anderson, T. K.; Chien, M.; Kumar, S.; Russo, J. J.; Kirchdoerfer, R. N.; Ju, J., A library of nucleotide analogues terminate RNA synthesis catalyzed by polymerases of coronaviruses that cause SARS and COVID-19. *Antiviral research* **2020**, *180*, 104857.
164. Anand, K.; Ziebuhr, J.; Wadhwani, P.; Mesters, J. R.; Hilgenfeld, R., Coronavirus main proteinase (3CLpro) structure: basis for design of anti-SARS drugs. *Science* **2003**, *300* (5626), 1763-1767.
165. Yoshinaga, T.; Kobayashi, M.; Seki, T.; Miki, S.; Wakasa-Morimoto, C.; Suyama-Kagitani, A.; Kawachi-Miki, S.; Taishi, T.; Kawasuji, T.; Johns, B. A.; Underwood, M. R.; Garvey, E. P.; Sato, A.; Fujiwara, T., Antiviral characteristics of GSK1265744, an HIV integrase inhibitor dosed orally or by long-acting injection. *Antimicrob Agents Chemother* **2015**, *59* (1), 397-406.
166. Young, C. A., FDA approves first once-monthly injectable drug regimen for adults with HIV. *Pharmacy Today* **2021**, *27* (3), 15.
167. Beyer, D. K.; Forero, A., Mechanisms of Antiviral Immune Evasion of SARS-CoV-2. *Journal of molecular biology* **2022**, *434* (6), 167265.
168. Song, P.; Li, W.; Xie, J.; Hou, Y.; You, C., Cytokine storm induced by SARS-CoV-2. *Clinica chimica acta* **2020**, *509*, 280-287.
169. Xie, T.; Du, G. H., [Pain of high-throughput screening--pan assay interference compounds]. *Yao Xue Xue Bao* **2015**, *50* (8), 925-30.
170. Dahlin, J. L.; Walters, M. A., How to Triage PAINS-Full Research. *Assay Drug Dev Technol* **2016**, *14* (3), 168-174.
171. Zhu, T.; Cao, S.; Su, P.-C.; Patel, R.; Shah, D.; Chokshi, H. B.; Szukala, R.; Johnson, M. E.; Hevener, K. E., Hit identification and optimization in virtual screening: practical recommendations based on a critical literature analysis. *Journal of medicinal chemistry* **2013**, *56* (17), 6560-6572.
172. Panchuk-Voloshina, N.; Haugland, R. P.; Bishop-Stewart, J.; Bhalgat, M. K.; Millard, P. J.; Mao, F.; Leung, W.-Y.; Haugland, R. P., Alexa Dyes, a Series of New Fluorescent Dyes that Yield Exceptionally Bright, Photostable Conjugates. *Journal of Histochemistry & Cytochemistry* **1999**, *47* (9), 1179-1188.
173. Feng, B. Y.; Shelat, A.; Doman, T. N.; Guy, R. K.; Shoichet, B. K., High-throughput assays for promiscuous inhibitors. *Nature Chemical Biology* **2005**, *1* (3), 146-148.

174. Aldrich, C.; Bertozzi, C.; Georg, G. I.; Kiessling, L.; Lindsley, C.; Liotta, D.; Merz, K. M., Jr.; Schepartz, A.; Wang, S., The Ecstasy and Agony of Assay Interference Compounds. *ACS Cent Sci* **2017**, 3 (3), 143-147.
175. Bakhtiar, R., Surface Plasmon Resonance Spectroscopy: A Versatile Technique in a Biochemist's Toolbox. *J Chem Educ* **2013**, 90 (2), 203-209.
176. Tang, Y.; Zeng, X.; Liang, J., Surface Plasmon Resonance: An Introduction to a Surface Spectroscopy Technique. *J Chem Educ* **2010**, 87 (7), 742-746.
177. Benvenuti, M.; Mangani, S., Crystallization of soluble proteins in vapor diffusion for x-ray crystallography. *Nature protocols* **2007**, 2 (7), 1633-1651.
178. Adams, P. D.; Afonine, P. V.; Bunkóczi, G.; Chen, V. B.; Davis, I. W.; Echols, N.; Headd, J. J.; Hung, L.-W.; Kapral, G. J.; Grosse-Kunstleve, R. W., PHENIX: a comprehensive Python-based system for macromolecular structure solution. *Acta Crystallographica Section D: Biological Crystallography* **2010**, 66 (2), 213-221.
179. Minor, W.; Cymborowski, M.; Otwinowski, Z.; Chruszcz, M., HKL-3000: the integration of data reduction and structure solution—from diffraction images to an initial model in minutes. *Acta crystallographica section D: biological crystallography* **2006**, 62 (8), 859-866.